Hybrid PIC-MCC Computational Modeling of Hall Thrusters

by

Justin William Koo

A dissertation submitted in partial fulfillment
of the requirements for the degree of
Doctor of Philosophy
(Aerospace Engineering and Scientific Computing)
in The University of Michigan
2005

Doctoral Committee:

Professor Iain D. Boyd, Chair
Professor Alec D. Gallimore
Professor Brian E. Gilchrist
Assistant Professor Andrew J. Christlieb

© Justin William Koo / All Rights Reserved 2005

Dedicated to my family,
Mom, Dad, Renee, Belinda, Gavin, and Michelle,
who believed in me from the very beginning

ACKNOWLEDGEMENTS

Before I begin, I'd like to make clear that this thesis represents the efforts not only of myself, but also of every single person who has assisted and encouraged me throughout the years. There are so many of people to thank, that, due to sheer numbers alone, I will undoubtedly fail to acknowledge some. For these omissions, I offer my most humble apologies. Find me and I'll thank you in person..maybe I'll even buy you a burrito.

First, I'd like to thank my professor, Iain D. Boyd, who, despite my protests to the contrary, insisted that I had plenty of material to write a thesis (he was right). Thank you for providing me with the invaluable guidance necessary to develop this thesis while at the same time granting me the independence to choose my own path. For your balanced efforts, I am a far more complete scientist than I ever expected. I'd also like to thank the rest of the faculty for the inspiration and wisdom they have shared with me throughout the years. In particular, I'd like to thank Prof. Alec D. Gallimore for sparking my interest in EP and permitting me to bother his entire experimental group (for 5+ years now) in my efforts to understand how plasma thrusters "actually" work.

My graduate career would probably have been stuck in a bureaucratic swamp for another five years without the experience and dedication of Margaret Fillion as the graduate secretary (and chief cookie and candy provider) in the aerospace department and Pam Derry as the (overworked) LaSC program coordinator and the

local administrator for my DOE fellowship. I was always comforted knowing that you two were constantly looking out for my stipend and my transcript. To the rest of the support staff, thank you for shepherding me through the system. I have heard tales of how the third floor was always falling apart and and how students were always falling through the cracks, yet you always managed to keep my paperwork complete and my health benfits intact. Thank you all for giving me the peace of mind to focus single-mindedly on my research.

I'd like to acknowledge my first year of support from the University of Michigan through a TA/RA appointment. For the next four years, I was generously supported by a Department of Energy Computational Science Graduate Fellowship Program of the Office of Scientific Computing and Office of Defense Programs in the Department of Energy under contract DE-FG02-97ER25308. I want to express my particular gratitude to the US government for providing this wonderful opportunity. Moreover, I want to thank the Krell Institute and all its wonderful staff for their tireless efforts in administering the CSGF fellowship which make it the unqualified envy of all graduate students. Finally, I'd like to thank NASA for supporting my last semester of research under grant NNC04GA38G.

And to my fellow grad students, thank you with all my heart. There were days when I was tired and frustrated, but I still came in to the department because I knew that you would be there.

– First, the Old Guard – Al , Alphonso (and Shabnam), Ansis, Mike Meuller, "Club" Mani Rad, Biju, Ed, Suman, Chad "The Elder" Ohlandt, Amit, Basu, Rajeeva, Javier (Spanish), Pete, Rich, Tim and Dr. James Matthew Haas. In particular, without drjimmyhaas and his internal plasma measurements of the P5, my thesis would be little more than a computational workout for three year old SUN

machines. And thanks, Pete, for sticking by your self-field ideas...they really could to shake up the modeling world. Thanks guys, for making me understand that the aero department is actually a community, not just a set of labs and offices.

– Next, the Pancheros crew – Jeff "Tin Man" Sutton, "Red" Joe Rakow (or "El Diablo"), Ryan Elliott, and Chris Wing. My steadfast supporters, from El Gordo to La Gordita and now on to Qdoba, it probably works out that each page of the thesis costs about one burrito...and a lifetime of friendship.

– Finally, all you kids – Joe "Jowen" Owen, "Greasy" Matt, Jerry "Don't Piss Me Off" Emhoff, "Angry" Norhal, Mike Martin (still a kid in my book), "Big" Mitch, Brian Beal, Leigh McCue, "Young" Po-Heng Chen, Josh Rovey, Jon B, Johnny Y., Leo (both of ya, Leo S. and Leo R.), Yoshi, Floppy, Ellie, "Big" Jesse (thanks for the krypton) Linnell, "Little" Jesse Hoagg, Chadwick Clifford Rasmussen, Zach (and Ginelle), Sulabh, Anish, Jesse David Thomas, Farzad, Anton, Javier P., Allen "Victory" Victor, Kristina, Dan "hermo" Herman, Tom S. the Canadian, Bald Adam, Brian "Gator" Glaz, Islam H., Matt Rizzo, Eiji S., Marci, Big Dan (Bearded), Erin Lynn Renk, Robert "Robbie" Lobbia, and Julie Bellerose. You make me want to stay for another five years.

And lastly, as in my dedication, I want to thank my family for all the love and support. I wish everyone was as fortunate as me.

TABLE OF CONTENTS

DEDICATION . . . . . **ii**

ACKNOWLEDGEMENTS . . . . . **iii**

LIST OF FIGURES . . . . . **ix**

LIST OF TABLES . . . . . **xii**

LIST OF APPENDICES . . . . . **xiii**

CHAPTER

I. Introduction **1**

1.1 Objective 1
1.2 Newton's 3^{rd} Law and the Rocket Equation 3
1.3 Electric propulsion 4
1.4 Hall thruster historical background 7
1.5 Hall thruster operation 9
1.5.1 Magnetic field circuit 9
1.5.2 Secondary electron emission 10
1.6 Hall thruster types 11
1.6.1 Anode-layer thrusters 11
1.6.2 Dielectric wall thrusters 11
1.7 Computational modeling of Hall thrusters 12
1.7.1 Fluid modeling 13
1.7.2 Kinetic modeling 13
1.7.3 Hybrid modeling 14
1.8 Outline of the thesis 15

II. Governing Equations **16**

2.1 Overview 16
2.2 Magnetic field configuration 16
2.2.1 Magnetic field streamfunction 17
2.2.2 Thermalized potential 20

2.3 Heavy particle treatment . . . 21
2.3.1 Particle transport . . . 22
2.3.2 Shape factors . . . 22
2.3.3 Particle injection . . . 23
2.3.4 Boundary interaction . . . 24
2.4 Ionization algorithm . . . 24
2.4.1 Ground state ionization . . . 24
2.4.2 Stepwise ionization . . . 26
2.4.3 Collision multiplier technique . . . 26
2.4.3.1 Choosing the Collision Multiplier . . . 27
2.5 1-D Ohm's law . . . 28
2.5.1 Electron current density . . . 29
2.5.2 Ion current . . . 30
2.5.3 Current conservation . . . 31
2.5.4 Electron mobility . . . 33
2.5.4.1 Wall-Collision Approach . . . 33
2.5.4.2 Bohm Diffusion Approach . . . 34
2.6 Electron energy equation . . . 34
2.6.1 Volume integration . . . 36
2.6.2 Discretization . . . 38
2.6.3 Electron energy loss term . . . 44
2.7 Performance calculation . . . 46
2.8 Computational requirements . . . 47

III. Study of Numerical Parameters . . . 49

3.1 Overview . . . 49
3.2 Global timestep . . . 52
3.3 Physical grid refinement . . . 53
3.4 Magnetic field grid . . . 54
3.4.1 Virtual anode line . . . 59
3.4.2 Virtual cathode line . . . 65
3.4.3 Magnetic field grid refinement . . . 70
3.5 Electron energy studies . . . 72
3.5.1 Subcycling frequency . . . 72
3.5.2 Weighting factor . . . 74
3.6 Macroparticle count . . . 74
3.6.1 Induced Oscillations . . . 77
3.7 Conclusions . . . 83

IV. Physical Modeling Effects . . . 85

4.1 Virtual Anode Line Energy . . . 85
4.2 Electron-Wall Energy Losses . . . 88

4.3 Electron Energy Collision Losses . . . 92

V. Mobility Modeling and Experimental Validation . . . 97

5.1 UM/AFRL P5 Hall Thruster . . . 98
5.1.1 Computational Models for Anomalous Electron Mobility . . . 98
5.1.1.1 Performance Data . . . 100
5.1.1.2 Centerline Mobility . . . 102
5.1.1.3 Potential . . . 102
5.1.1.4 Mean Electron Energy . . . 110
5.1.1.5 Discussion . . . 114
5.1.2 Semi–Empirical Electron Mobility . . . 116
5.1.2.1 Experimental Data . . . 116
5.1.2.2 General Form . . . 116
5.1.2.3 Results . . . 121
5.1.2.4 Simulation using Semi-Empirical Electron Mobility 121
5.1.2.5 Discussion . . . 138
5.1.3 Semi-Empirical Self-Field Electron Mobility . . . 138
5.1.3.1 Magnetic Self-Field . . . 140
5.1.3.2 Thermalized Potential . . . 141
5.1.3.3 Mobility Results . . . 142
5.1.3.4 Discussion . . . 142
5.2 NASA-173Mv1 Hall Thruster . . . 145

VI. Summary and Future Work . . . 150

6.1 Conclusions . . . 150
6.2 Future Work . . . 152
6.2.1 2-D Electromagnetic Solver . . . 152
6.2.2 Mobility Modeling . . . 153
6.2.3 Ionization Algorithm . . . 153
6.2.4 Cathode Modeling . . . 153
6.2.5 Sheath Modeling and Wall Effects . . . 154
6.2.6 Neutral Collisions . . . 154
6.2.7 Charge-Exchange Collisions and Neutral Backpressure . . . 154

APPENDICES . . . 155

BIBLIOGRAPHY . . . 164

LIST OF FIGURES

Figure

1.1 UM/AFRL P5 Hall Thruster 8
1.2 NASA-173Mv1 Hall Thruster 8
1.3 Dielectric wall Hall thruster schematic 10

2.1 Magnetic field line geometry 18
2.2 NASA-173Mv1 Radial Magnetic Field 19
2.3 Hall Thruster Boundary Schematic 25
2.4 Electron energy equation geometry 37

3.1 NASA-173Mv1 Mean Centerline Potential 54
3.2 SPT-70 Magnetic Field Streamfunction 55
3.3 SPT-70 Lambda Grid Schematic 57
3.4 Ideal λ_a and λ_c configuration 57
3.5 SPT-70 Virtual Anode Lines 60
3.6 SPT-70 Mean Centerline Electron Energy 61
3.7 SPT-70 Mean Centerline Potential 61
3.8 SPT-70 Mean Centerline Source Rate 62
3.9 SPT-100 Virtual Anode Lines 63
3.10 SPT-100 Mean Centerline Electron Energy 64
3.11 SPT-100 Mean Centerline Source Rate 65
3.12 SPT-70 Virtual Cathode Lines 66
3.13 SPT-70 Mean Centerline Potential 67
3.14 SPT-100 Virtual Cathode Lines 68
3.15 SPT-100 Mean Centerline Potential 68
3.16 SPT-70 Lambda Grid ($\lambda = 23$) 71
3.17 SPT-70 Lambda Grid ($\lambda = 12$) 71
3.18 SPT-70 Mean Electron Energy 73
3.19 NASA-173Mv1 Macroparticle Count 76

3.20 NASA-173Mv1 Discharge Current – Experimental 77
3.21 NASA-173Mv1 Discharge Current – Computational (low macroparticle count) 78
3.22 NASA-173Mv1 Discharge Current – Computational 78
3.23 UM/AFRL P5 Discharge Current – Computational 79
3.24 NASA-173Mv1 Discharge Current – Computational (medium macroparticle count) 80
3.25 NASA-173Mv1 Discharge Current – Computational (high macroparticle count) 80
3.26 Collision Multiplier Effect 82

4.1 SPT-70 Mean Electron energy 87
4.2 UM/AFRL P5 Energy Loss Coefficient 89
4.3 UM/AFRL P5 Energy Loss Coefficient – U_{loss}=15 eV 91
4.4 UM/AFRL P5 Energy Loss Coefficient – α=0.05 91
4.5 UM/AFRL P5 Energy Loss Coefficient – α=0.20 92
4.6 UM/AFRL P5 Discharge Current - Vary α 93
4.7 UM/AFRL P5 Mean Electron Energy - Variation of energy loss rates 95
4.8 UM/AFRL P5 Discharge current trace - Variation of energy loss rates 96

5.1 UM/AFRL P5 Mean Centerline Mobility 104
5.2 UM/AFRL P5 Mean Potential (Wall-Collision mobility) 106
5.3 UM/AFRL P5 Mean Potential (Low Bohm mobility) 108
5.4 UM/AFRL P5 Mean Potential (High Bohm mobility) 109
5.5 UM/AFRL P5 Mean Potential (Mixed Outer mobility) 111
5.6 UM/AFRL P5 Mean Potential (Mixed Inner mobility) 112
5.7 UM/AFRL P5 Mean Centerline Energy 115
5.8 UM/AFRL P5 Plasma Properties 117
5.9 Idealized Ion Velocity Trace 120
5.10 UM/AFRL P5 Electron Current Density 122
5.11 UM/AFRL P5 Plasma Properties 123
5.12 UM/AFRL P5 Plasma Properties 124
5.13 UM/AFRL P5 Semi-Empirical Electron Mobility 126
5.14 UM/AFRL P5 Centerline Plasma Potential 127
5.15 UM/AFRL P5 Computational Mean Potential 128
5.16 UM/AFRL P5 Experimental Potential 129
5.17 UM/AFRL P5 Centerline Electron Temperature 130
5.18 UM/AFRL P5 Computational Discharge Current 131

5.19 UM/AFRL P5 Computational Centerline Properties 132
5.20 UM/AFRL P5 Instantaneous Plasma Temperature 133
5.21 UM/AFRL P5 Experimental Plasma Temperature 134
5.22 UM/AFRL P5 Computational Mean Plasma Density 135
5.23 UM/AFRL P5 Experimental Plasma Density 136
5.24 UM/AFRL P5 Magnetic Field Grid 137
5.25 Test Electron Current Densities 139
5.26 Semi-Empirical Electron Mobility 140
5.27 UM/AFRL P5 Radial Magnetic Field 141
5.28 UM/AFRL P5 Thermalized Potential 142
5.29 UM/AFRL P5 Semi-Empirical Mobility (Vacuum B_r) 143
5.30 UM/AFRL P5 Semi-Empirical Mobility (Plasma B_r) 143
5.31 UM/AFRL P5 Semi-Empirical Mobility (Vacuum B_r) 144
5.32 UM/AFRL P5 Semi-Empirical Mobility (Plasma B_r) 144
5.33 NASA-173Mv1 Kr Computational – Plasma Potential 147
5.34 NASA-173Mv1 Kr Computational – Plasma Properties 148

C.1 Xenon Ionization Rates 162
C.2 Xenon Energy Loss Rates 162
C.3 Krypton Ionization Rates 163
C.4 Krypton Energy Loss Rates 163

LIST OF TABLES

Table

3.1	SPT-70 Timestep Study	52
3.2	NASA-173Mv1 Mesh Spacing	54
3.3	SPT-70 Virtual Anode Line Study	60
3.4	SPT-100 Virtual Anode Line Study	63
3.5	SPT-70 Virtual Cathode Line Study	66
3.6	SPT-100 Virtual Cathode Line Study	67
3.7	SPT-70 Lambda Grid Refinement Study	72
3.8	SPT-70 Electron Energy Subcycling Frequency Performance Results	73
3.9	SPT-70 Electron Energy Weighting	74
4.1	SPT-70 Virtual Anode Line Energy	86
4.2	UM/AFRL P5 Rate Sensitivity	94
5.1	UM/AFRL P5 Xe Performance	99
5.2	UM/AFRL P5 Computational Mobility Model Performance Data	103
5.3	UM/AFRL P5 Computational Model Energy Loss Parameters	113
5.4	UM/AFRL P5 Xe Performance Data	125
5.5	NASA-173Mv1 Kr Performance	149

LIST OF APPENDICES

Appendix

A. Nomenclature 156

B. Effusion Sampling Routine 160

C. Ionization and Energy Loss Rates 161

CHAPTER I

Introduction

1.1 Objective

Hall thrusters are electrically powered space propulsion devices designed to efficiently provide low amounts of thrust ($\sim$ 100 mN) for a very long period of time (thousands of hours). These devices, first seriously studied in the 1960's, have a 30 year operational history in the Soviet/Russian space program and are presently entering use in Western space programs. Hall thrusters have a number of very desirable characteristics. Besides their efficiency and long life, they are also physically robust propulsion systems with relatively large performance envelopes (from "low" thrust station-keeping operation to "high" thrust orbit raising operation).

The early design heritage of Hall thrusters was largely experimental. This early design work provided the scaling laws and other design rules used today, with great success, to design newer, more efficient, high power Hall thrusters. Only recently, with the development of new computational models, has computational modeling of Hall thrusters begun to offer serious promise as a valuable tool for both understanding Hall thruster physics and designing new Hall thrusters. A variety of different approaches and numerical schemes for computational modeling of Hall thrusters have been developed in the last 10 years. Of these different models, hybrid modeling (i.e.

the use of a particle model to simulate the heavy particles and a fluid model to simulate the electrons) offers an attractive blend of physical accuracy and computational efficiency that makes it a promising candidate for further study.

Critical modeling challenges remain for all existing Hall thruster codes. The two greatest challenges are understanding how to model the electron mobility and how to incorporate the correct electron energy loss mechanisms. Fortunately, computational modeling of Hall thrusters is sufficiently advanced that, given some knowledge of the simulation output in order to calibrate the modeling parameters, fairly representative results can be achieved in a few hours on a desktop computer.

Understanding the impact of modeling parameters is very important to maturing computational codes to a level where computational simulation of Hall thrusters is widely accepted as a serious counterpart to experimental measurement. To this end, extensive work has been performed to understand and validate the effect of the electron mobility on a full hybrid code by *Hagelaar et al.* (2003) and *Bareilles et al.* (2004). This thesis is based on a similar 2-D axisymmetric code with related models for the electron mobility and the electron energy loss; however, different experimental validation is provided. In particular, the focus of the validation effort presented in this thesis is on the effect of different propellants and higher thruster voltages.

The following sections present a brief introduction to electric propulsion, a discussion of the historical background, operation and different types of Hall thrusters, a review of existing computational modeling approaches, and an outline of the main body of the dissertation.

1.2 Newton's 3^{rd} Law and the Rocket Equation

Both electric propulsion (EP) and conventional spacecraft propulsion (chemical rockets) are based on Newton's Third Law as follows:

$$m\frac{dV}{dt} = \dot{m}U_e \tag{1.1}$$

where the left hand side of Eqn. 1.1 represents the spacecraft acceleration and the right hand side represents the propellant thrust. Replacing $\dot{m}$ by $-\frac{dm}{dt}$ and integrating as follows:

$$\int_{V_i}^{V_f} -\frac{dV}{U_e} = \int_{m_i}^{m_f} \frac{dm}{m} \tag{1.2}$$

provides the classical "Rocket Equation" (for a single stage spacecraft)

$$\frac{m_f}{m_i} = e^{\frac{-\Delta V}{U_e}} \tag{1.3}$$

where the left hand side is the final non-propellant mass fraction of the spacecraft and ΔV represents the mission velocity requirement. (In Eq. 1.3, drag and gravity losses are ignored.) The "Rocket Equation" describes the relationship between the mission velocity requirement and the amount of propellant mass ($m_p = m_i - m_f$) required to achieve this velocity, and the performance of the propulsion system (characterized by a propellant exit velocity U_e). In particular, for a given mission velocity requirement, the higher the propellant exit velocity, the less propellant mass is required.

Specific Impulse

In the propulsion literature, the concept of specific impulse (I_{sp}) describes the amount of time that one pound of propellant can theoretically produce one pound of

thrust. The specific impulse is measured in seconds and is defined as follows (where g is the graviational acceleration at the earth's surface):

$$I_{sp} = \frac{T}{\dot{m}_p g} = \frac{U_e}{g} \tag{1.4}$$

From this definition, it is clear that I_{sp} is a direct measure of the propellant exit velocity of a given spacecraft propulsion system.

Example: Communications satellite

Consider a communications satellite requiring $\Delta V = 100$ m/s per year (Orbit correction plus E-W stationkeeping plus N-S stationkeeping) for 10 years (*Larson and Wertz* (1992)). If this satellite was equipped with a typical bipropellant chemical rocket propulsion system with $I_{sp} = 250$ s, then the propellant mass required for the mission duration would be 33% of the initial satellite mass. If a Hall thruster based propulsion system with $I_{sp} = 2{,}000$ s was used for the same mission, the propellant mass required would be only 5% of the initial satellite mass. This is a very clear example of how EP offers very attractive alternatives to conventional chemical space propulsion systems.

1.3 Electric propulsion

Electric propulsion (EP) refers to a class of space propulsion devices which use electric power to produce thrust. Generally speaking, these devices have much higher propellant exit velocities than chemical propulsion devices (typical bipropellant rockets have an I_{sp} between 250 s and 400 s). As a consequence, EP devices require much less propellant mass than chemical systems for a given mission requirement, making EP very attractive to spacecraft designers. The primary drawback of EP devices

is their relatively low thrust densities which precludes high thrust applications. EP devices can be broadly categorized into three principal types – (1) electrothermal, (2) electrostatic, and (3) electromagnetic devices. The brief treatment of each of these categories provided in this section is based on the mongraph by *Jahn and Choueiri* (2002).

Electrothermal

Electrothermal EP devices use electric power to heat the propellant which is then accelerated through a nozzle to produce thrust. Typical electrothermal EP devices are resistojets and arcjets. Resistojets use a heating element to raise the temperature of the propellant. Arcjets bypass the materials concerns of the heating element by directly depositing energy into the propellant using an electric arc. Since both types of thrusters contain very high temperature, high density gases, the performance is limited by the material properties of the thruster body and/or heating elements. The I_{sp} for a typical 1 kW class resistojet is ~ 350 s with a thrust of ~ 0.3 N. The I_{sp} for a typical 1.5 kW class hydrazine arcjet is $\sim 500 - 600$ s. The power level for arcjets has been extended as high as 100 kW.

Electrostatic

Electrostatic EP devices, such as ion thrusters and FEEPs (Field Electron Electric Propulsion), use electrostatic fields to accelerate a charged propellant. An electron source in the near-field plume neutralizes the positively charged propellant. By using electric power directly to accelerate the propellant rather than relying on thermal expansion (as in an electrothermal device), many materials limitations can be circumvented and very high propellant exit velocities can be achieved. Unfortunately, the thrust density of these devices is constrained by space-charge limitations. In

particular, across an acceleration gap, d, the maximum achievable current density is:

$$j_{sc} = \frac{4\epsilon}{9}\left(\frac{2q}{m_i}\right)^{1/2}\frac{V^{3/2}}{d^2} \tag{1.5}$$

Typical ion thrusters are characterized by specific impulses of 3,000 s – 4,000 s and power levels between a few hundred watts and 5 kW. Next generation ion thrusters planned by NASA (see *Foster et al.* (2004)) will raise the power level to more than 25 kW and specific impulses in excess of 7,000 s. FEEPs, which are used primarily for fine stationkeeping, use very little power and provide only micronewtons of thrust.

Electromagnetic

Electromagnetic EP devices use a combination of electric (E) and magnetic (B) fields to accelerate a propellant and produce thrust. In particular, a plasma is subject to perpendicular E and B fields to produce a net plasma current which experiences a body force of $F = j \times B$. The plasma typically remains neutral so space charge limitations are not a constraint on the thrust density of electromagnetic thrusters.

Typical electromagnetic EP devices are magnetoplasmadynamic thrusters (MPD) and Pulsed Plasma thrusters (PPT). MPD thrusters are high power (>100 kW), high thrust (>1 N) EP devices with I_{sp} ranges from 1,500 s to 8,000 s. PPTs use many of the same principles as MPD thrusters but operate in a pulsed mode. Electrical power is stored in capacitor banks and released over a relatively short time ($< 10\ \mu s$) in a high power electric discharge which ionizes the propellant and induces the requisite $E \times B$ force to accelerate the plasma. PPTs operate over a very large thrust range but suffer from low efficiency (typically < 20 %).

1.4 Hall thruster historical background

Hall thrusters, classified as either electrostatic or electromagnetic thrusters, operate in a power range from 200 W to greater than 50 kW with I_{sp} ranges from 1,000 s to 5,000 s. These EP devices, also known as closed drift thrusters or coaxial Hall plasma accelerators, were first studied in the early 1960's in both the US and the USSR. During the 1970's and 1980's, the US EP program shifted its focus away from Hall thrusters and towards other types of space propulsion devices. The Soviet EP program continued a robust Hall thruster development effort during this period and is credited with greatly maturing Hall thruster design. The Soviet (and later Russian) EP program is also credited with the first (1972) and vast majority (approximately 100) of Hall thrusters placed into orbit on operational satellites (*Zhurin et al.* (1999)).

Recent US, European, and Japanese interest in Hall thrusters has been driven by particular qualities of these thrusters, including their combination of relatively high thrust, high efficiency, and their demonstrated physical robustness (i.e. their high reliability after the severe vibrational loadings endured during launch). Hall thruster development in recent years has included the development of higher power thruster configurations for possible use in interplanetary space missions. These include both very large thrusters, such as the 50 kW NASA-457M, and clustering of existing thrusters, such as the 5 kilowatt – class UM/AFRL P5 (Fig. 1.1) and NASA-173Mv1 (Fig. 1.2). Finally, Hall thrusters are gaining acceptance as a favored means of on-orbit satellite propulsion for both civilian and military satellites. This work includes the development of dual mode (high thrust-to-power and high I_{sp}) thrusters suitable for both orbit insertion and orbit maintenance/station-keeping.



Figure 1.1: UM/AFRL P5 Hall thruster (*Courtesy of Plasmadynamics and Electric Propulsion Laboratory (PEPL) at the University of Michigan*)

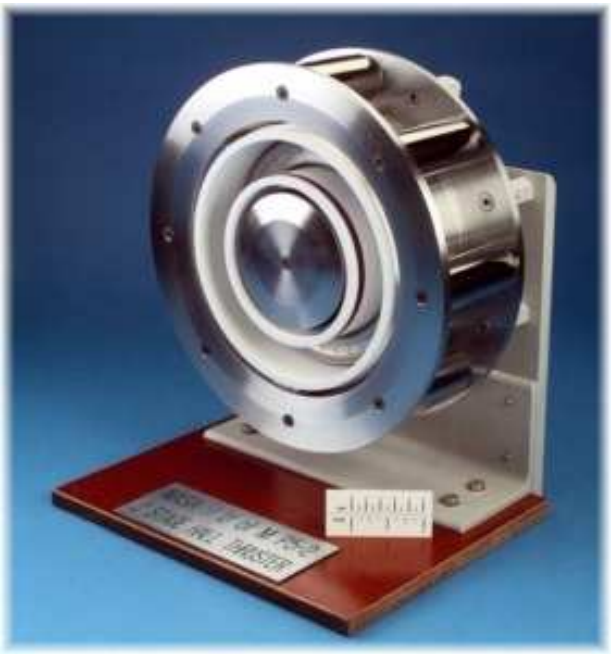


Figure 1.2: NASA-173Mv1 Hall thruster (*Courtesy of PEPL*)

1.5 Hall thruster operation

To produce thrust, a Hall thruster must ionize then accelerate the propellant. Both of these functions are achieved in a Hall thruster through the use of a carefully designed magnetic field circuit. A Hall thruster requires two power sources - (1) power is required to maintain a voltage drop between the anode and external cathode (this is known as the discharge voltage) and (2) power is required to energize the electromagnets that produce the characteristic magnetic field required in the thruster.

The propellant, typically xenon, is injected into the thruster at the anode. This neutral propellant diffuses down the acceleration channel and encounters a population of high energy ionizing electrons in the the region of high Hall current known as the "ionization zone". There is a high probability of ionization in this region, and, once ionized, the ions respond to the potential gradient and are accelerated out of the thruster. An external cathode provides a source of electrons to ensure that the ions in the plume are fully neutralized and an electron source for ionization of the propellant.

1.5.1 Magnetic field circuit

The twin goals of the magnetic field design in a Hall thruster are to maximize both the propellant ionization efficiency and the effective potential drop experienced by the ions. This is ideally achieved by locating the ionization zone upstream of the main potential gradient. The applied voltage drop between the anode and cathode provides an axial electric field throughout the acceleration channel. The magnetic field circuit is designed to provide a relatively strong (a few hundred gauss) radial magnetic field near the exit of the acceleration channel. The interaction of the axial

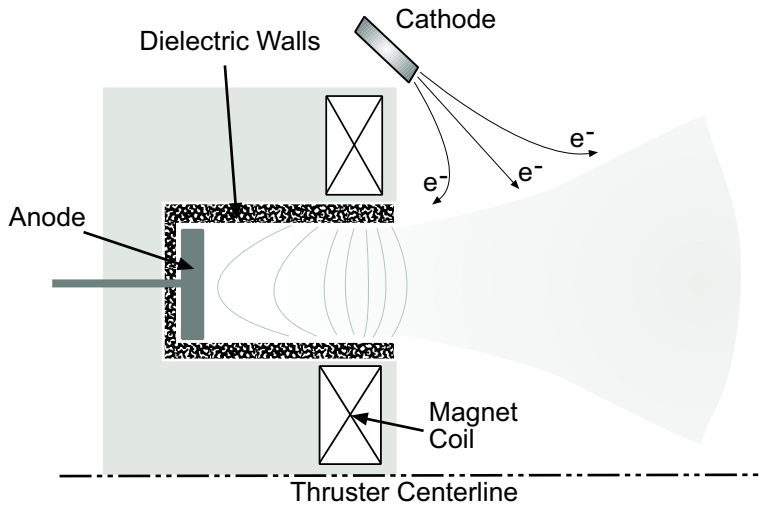


Figure 1.3: Dielectric wall Hall thruster schematic

electric field and the radial magnetic field near the exit of the acceleration channel provides an $E \times B$ force which accelerates the electrons azimuthally. The resulting azimuthal electron drift is known as the Hall current and provides the necessary high energy electron population for efficient propellant ionization.

1.5.2 Secondary electron emission

Electrons accelerated by the $E \times B$ drift frequently collide with the acceleration channel walls and deposit some of their energy into the walls. If the collision energy is high enough, "secondary" electrons are ejected after the high energy electrons collide with the walls. These secondary electrons emerge at significantly lower temperature than the primaries, resulting in a lower bulk plasma temperature and a non-Maxwellian velocity distribution function. The secondary electron emission (SEE) coefficient (itself a function of energy) describes the number of low energy electrons that result from the impact of a single high energy electron with a particular wall material.

1.6 Hall thruster types

There are two types of Hall thruster - metallic wall thrusters and dielectric wall thrusters. The former, known as TAL (Thruster with Anode Layer) thrusters, have a conductive material on the acceleration channel walls while the latter, known as SPT (Stationary plasma thrusters) thrusters, have dielectric material on the acceleration channel walls. The difference in the operating characteristics of SPT and TAL thrusters can be related directly to the disparate SEE coefficient and conductive properties of the different wall types.

1.6.1 Anode-layer thrusters

In an anode-layer (TAL) thruster, the metallic walls are conductive and have a very low SEE coefficient. Since the walls are conductive, a constant potential is observed along the entire wall. Very high electron temperatures (> 50 eV) are typically observed in TAL thrusters. These thrusters are typically designed with relatively short acceleration channels and rarely exceed 1 cm – 2 cm in length.

1.6.2 Dielectric wall thrusters

All of the thrusters modeled in this thesis are dielectric wall Hall thrusters. One particular lineage of dielectric wall Hall thrusters is a Russian design known as a Stationary Plasma Thruster (SPT). Since the dielectric walls are not conductive, charge builds up along the length of the acceleration channel and leads to a variable potential profile along the length of the acceleration channel walls. The dielectric walls can also promote the formation of an ion-attracting plasma sheath near the wall surface; however, the high SEE coefficient enables the reversal of this sheath to an electron-attracting plasma sheath if the electron energy is sufficiently high.

This large SEE effect also serves to moderate the temperature of the plasma in the acceleration channel by converting high energy electrons into low energy electrons. These thrusters are characterized by much lower electron energies than TAL thrusters and spatially lengthened acceleration zones.

1.7 Computational modeling of Hall thrusters

Due to the complicated physics of Hall thruster operation and the relatively immature computational tools available at the time, early Hall thruster studies were largely experimental. As a consequence, computational modeling of Hall thrusters is a relatively young field of study; however, many very compelling reasons exist to further this line of study.

Computational modeling of Hall thrusters offers a number of tantalizing possibilities for improving thruster-spacecraft integration and operation testing. In addition, simulation enables the effects of facility backpressure to be investigated in a very isolated fashion, thus avoiding one of the primary pitfalls (finite facility backpressures) of vacuum chamber based thruster testing. This role is even more crucial with the development of new, high power Hall thrusters which operate at very high mass flow rates that can swamp the ability of the cryopumps to maintain sufficiently high vacuum in test chambers. Finally, computational modeling can be developed to track wall-erosion characteristics of thrusters in order to verify thruster lifetime limitations from the erosion of the dielectric walls.

As a research tool, computational simulation offers the ability to isolate physical effects such as channel wall materials and anode presheath formation, resulting in a clearer understanding of the physics of these devices. Eventually, when Hall thruster physics are better understood, these computational codes will also become useful

design tools for future generations of Hall thrusters.

Computational modeling of Hall thrusters can be broken up into three main categories - (1) fluid, (2) kinetic, and (3) hybrid codes. Important aspects of these approaches are discussed in this section.

1.7.1 Fluid modeling

Fluid modeling of Hall thrusters considers both electrons and heavy species (ions and neutrals) to be fluids. This approach to thruster modeling is very fast (measured in minutes) and can be adapted to both 1-D and 2-D axisymmetric geometries and to both steady state and time-dependent solvers. The primary drawback of fluid codes is the fundamental inability to model the velocity (VDF) and the energy distribution functions (EDF) dynamically. Typical fluid codes ignore the ion thermal pressure (cold ions) and use a single temperature (assuming a Maxwellian form) for the electrons.

Examples of these codes are a 1-D steady state model with an anode sheath region and an effective near-field plume region by *Ahedo et al.* (2001), a 1-D steady state model with a detailed wall presheath treatment by *Keidar et al.* (2002) and a 2-D model by *Roy and Pandey* (2001).

1.7.2 Kinetic modeling

Kinetic (particle-based) modeling of Hall thrusters uses discrete particles to simulate both electrons and heavy species. The discrete particles automatically model the VDF and EDF, thus allowing these codes to handle the non-Maxwellian distribution functions expected in Hall thrusters. This additional accuracy comes at the expense of much greater computational cost. Since the electrons are several orders of magnitude lighter than the ions, they move on a much smaller timescale.

This requirement forces the use of timesteps which are about 500 times smaller than timesteps consistent with ion dynamics alone.

The work of *Szabo* (2001) is the most advanced fully kinetic 2-D code developed to date. Further work by *Blateau et al.* (2001) has extended this code to high powers and *Sullivan et al.* (2004) have extended the work from 50 W TAL thrusters to kilowatt-class SPT thrusters. This code circumvents some of the computational expense of fully kinetic modeling by increasing the electron mass and free space permittivity in order to increase the electron timestep. Despite these efforts, the computational expense of fully kinetic codes is still very high, with typical simulations lasting from days to weeks.

1.7.3 Hybrid modeling

Hybrid modeling offers a compromise between fluid modeling and kinetic modeling. By considering heavy species as particles and electrons as a fluid, hybrid codes can capture non-Maxwellian features for the heavy species without incurring the severe timestep penalty associated with fluid electron modeling. Both 1-D and 2-D axisymmetric hybrid codes exist, with early development pioneered by *Fife* (1998) and *Boeuf and Garrigues* (1998). Further development of hybrid codes has been performed by *G. J. M. Hagelaar and Boeuf* (2002) and *Koo and Boyd* (2004).

These codes all share the common elements of Particle-In-Cell (PIC) treatment of the heavy particles and some form of a 1-D Ohm's Law equation using the thermalized potential to evaluate the electrostatic potential. The electron EDF is assumed to be Maxwellian for all the models cited in this section, although other EDFs could be incorporated. Typical run times for this type of code are between 6-24 hours on a SUNBlade 1500 for a converged thruster simulation.

1.8 Outline of the thesis

Computational modeling of Hall thrusters has reached an important development phase. Reasonable numerical solutions are computationally tractable on desktop computers and results can be guided to very near to experimental values; however, the use of computational models in a predictive capacity as a design tool for new generations of thrusters requires deeper understanding of both the numerical behavior and modeling choices on which present Hall thruster codes are based. Accordingly, this thesis is broken up into four main sections covering these tasks. Chapter II presents the governing equations represented in the 2-D axisymmetric hybrid Hall thruster code developed for this thesis. In Chapter III, the numerical implementation of these equations in the code is considered. Chapter IV presents the results of different physical effects on thruster operation. In Chapter V, extensive experimental validation is presented for the UM/AFRL P5 thruster. Finally, Chapter VI provides a summary of this work and outlines suggestions of future research paths.

CHAPTER II

Governing Equations

2.1 Overview

The governing equations for a 2-D axisymmetric PIC-MCC Hall thruster code are presented in this section. Heavy particles (ions and neutrals) are modeled with a Particle-In-Cell (PIC) treatment and undergo collisions via a Monte Carlo Collision (MCC) algorithm. The electric field is calculated based on a 1-D Ohm's Law formulation of current conservation. Finally, electrons are considered to behave as a fluid with a Maxwellian energy distribution according to an explicit energy balance equation.

2.2 Magnetic field configuration

The magnetic field configuration of a Hall thruster is a critical factor in the operation of these devices. Combinations of internal and external electromagnets make it possible to shape the magnetic field throughout the device and thus influence the plasma distribution throughout the acceleration channel.

Two magnetic field states are generally referenced. These are the vacuum magnetic field and the magnetic field during thruster operation (when the thruster is filled with plasma). Traditional Hall thruster studies assume that the vacuum magnetic

field is roughly equivalent to the magnetic field during thruster operation. Although the work of *Peterson et al.* (2002) hints at the possibility that the magnetic field is dynamically influenced by thruster operation, the static approach is still considered acceptable for this class of simulations. Consequently, the static magnetic field configuration used in this code is based on the vacuum magnetic field values.

The vacuum magnetic field can be obtained in a number of ways. It can be measured experimentally using a Hall probe, it can be calculated from a combination of experimentally derived boundary values and a $\nabla \times \vec{B} = 0$ condition, or it can be calculated purely computationally using an electromagnetic field solver program. The vacuum magnetic field values are used directly to evaluate the electron mobility. In addition, they are used to convert the 2-D axisymmmetric domain to a 1-D domain by establishing roughly radial slices along magnetic field lines.

2.2.1 Magnetic field streamfunction

The shortest of Maxwell's equations, shown below, guarantees that the divergence of the magnetic field is zero everywhere inside and outside the thruster.

$$\nabla \cdot \vec{B} = 0 \tag{2.1}$$

In the two-dimensional divergence-free vector field that is the static magnetic field configuration, it is therefore possible to construct a magnetic field streamfunction, λ. The relationships between the magnetic field streamfunction and the magnetic field vector components in cylindrical coordinates are:

$$B_r = \frac{-1}{r}\frac{\partial \lambda}{\partial z} \tag{2.2}$$

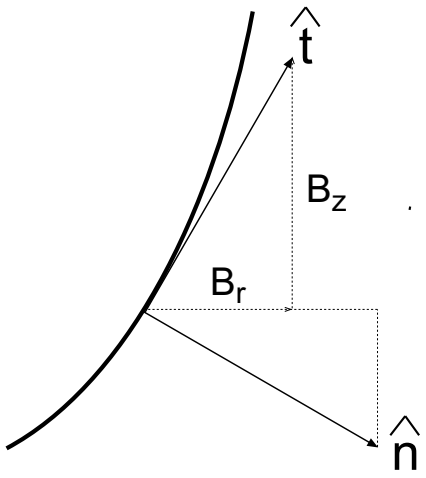


Figure 2.1: Magnetic field line geometry

$$B_z = \frac{1}{r}\frac{\partial \lambda}{\partial r} \tag{2.3}$$

Equipotentials of the magnetic field streamfunction represent magnetic field lines while the gradient of the magnetic field streamfunction indicates the local strength of the magnetic field. In particular, regions with large λ gradients have strong magnetic fields. By choosing equally spaced λ intervals, a series of magnetic field lines are generated which enable the discretization of the 2-D axisymmetric domain into a 1-D domain (see Sec. 3.4).

Since the magnetic field lines defining the 1-D domain are not strictly radial, as shown in Fig. 2.2, it is necessary to develop an expression for the normal and normal derivative to the magnetic field lines. The normal vector $\hat{n}$ and tangential vector $\hat{t}$ are shown in Fig. 2.1.

$$\hat{t} = \frac{B_r}{B}\hat{r} + \frac{B_z}{B}\hat{z} \tag{2.4}$$

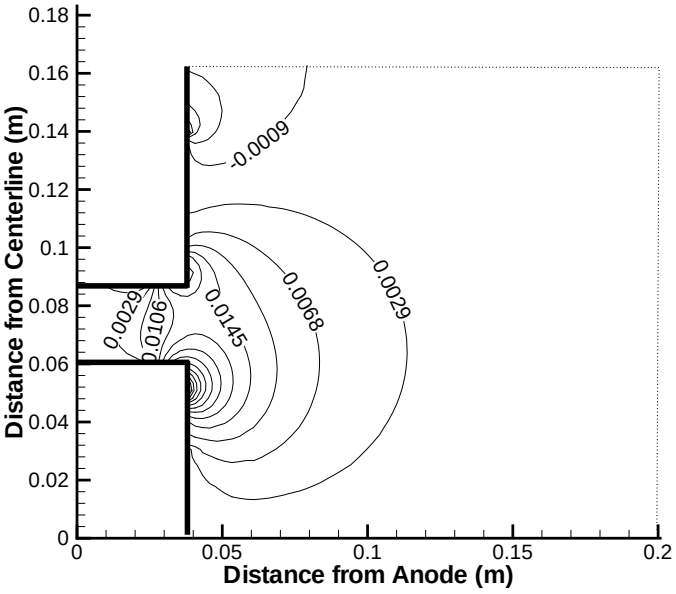


Figure 2.2: NASA-173Mv1 Radial Magnetic Field

$$\hat{n} = \frac{B_z}{B}\hat{r} - \frac{B_r}{B}\hat{z} \tag{2.5}$$

To evaluate the normal derivative to the magnetic field lines, the following formula is used, where the derivative of λ with respect to the normal vector is simply the gradient of λ:

$$\frac{\partial}{\partial \hat{n}} = \frac{\partial}{\partial \lambda}\frac{\partial \lambda}{\partial \hat{n}} = \nabla\lambda\frac{\partial}{\partial \lambda} \tag{2.6}$$

Evaluating the gradient of λ reveals:

$$\nabla\lambda = \frac{\partial \lambda}{\partial r}\hat{r} + \frac{\partial \lambda}{\partial z}\hat{z} = rB_z\hat{r} - rB_r\hat{z} \tag{2.7}$$

Finally, combining Eqn. 2.6 and Eqn. 2.7 yields:

$$\frac{\partial}{\partial \hat{n}} = rB\frac{\partial}{\partial \lambda}\hat{n} \tag{2.8}$$

2.2.2 Thermalized potential

Charged particles in Hall thrusters develop cyclotron orbits about magnetic field lines (see *Chen* (1984)). The radius of these orbits, known as the Larmor radius, is as follows:

$$r_L \equiv \frac{v_\perp}{\omega_c} = \frac{mv_\perp}{|q|\,B} \tag{2.9}$$

In the acceleration channel (see Fig. 2.3), the average magnetic field is ~ 0.01 T. For newly created Xe^{++} ions, this leads to a minimum ion Larmor radius of ~ 2.7 cm. For electrons with an energy of 20 eV, this leads to a maximum Larmor radius of ~ 0.6 mm. This simple analysis illustrates a general property of Hall thrusters (where d is the channel diameter):

$$r_{L_e} \ll d < r_{L_i} \tag{2.10}$$

Since ions in a Hall thruster have a larger Larmor radius than the acceleration channel, they behave in an effectively unmagnetized manner in this region. The smaller Larmor radii of the electrons reflects the ability of the high radial magnetic field in the acceleration channel to retard bulk electron motion towards the anode.

Although the motion of electrons is constrained across the radial magnetic field, their motion is not constrained along magnetic field lines. As a consequence, the electron diffusion coefficient is much higher along field lines than across them. Therefore, it is possible to consider a simple balance of pressure and electric forces along field

lines as follows:

$$\frac{\partial(n_e k_B T_e)}{\partial \hat{t}} = e n_e \frac{\partial \phi}{\partial \hat{t}} \tag{2.11}$$

Since the electron dynamics occur much faster than the timestep considered in this code, it can be assumed that the electrons reach thermal equilibrium along field lines very rapidly. Since the electrons are isothermal along field lines, this equation can be simplified to:

$$k_B T_e \frac{\partial n_e}{\partial \hat{t}} = e n_e \frac{\partial \phi}{\partial \hat{t}} \tag{2.12}$$

This equation can then be integrated to obtain:

$$\phi^*(\lambda) = \phi - \frac{k_B T_e}{e} ln(n_e) \tag{2.13}$$

This particular formulation is known as the thermalized potential and was introduced by *Morozov et al.* (1972). It is calculated on the centerline of the thruster at the beginning of each iteration and enables a reduced description of a plasma potential along any magnetic field line with a single thermalized potential value. With knowledge of the local plasma density and electron temperature, this thermalized potential can be converted back to the traditional electrostatic potential.

Another interpretation of the thermalized potential, provided by *Bittencourt* (1986), is as an equilibrium balance of electrons in a conservative forcefield. Thus, along a magnetic field line from a given location with properties, $T_e, n_{e,0}, \phi_0$, the plasma potential at some other location (with local plasma density $n_{e,1}$) is:

$$\phi_1 - \frac{k_B T_e}{e} ln(n_{e,1}) = \phi_0 - \frac{k_B T_e}{e} ln(n_{e,0}) \tag{2.14}$$

2.3 Heavy particle treatment

Heavy particles in the simulation (neutrals and ions) are treated with a Particle-In-Cell (PIC) technique as described by *Birdsall and Langdon* (1991). Rather than

tracking individual particles of each species, agglomerations of particles, known as macroparticles, are tracked instead. Typical macroparticles represent between 10^8 to 10^{10} real particles. The data associated with each macroparticle are the particle numerical weight, species type, two position coordinates (axial and radial) and three cartesian velocity coordinates.

2.3.1 Particle transport

The motion of the heavy particles is based on a classical leapfrog update scheme. This represents a first order advection scheme for both the position and velocity with the two quantities updated on a half timestep differential. Specifically, the ion positions are calculated on integer timesteps while the ion velocities are calculated at half-timesteps relative to ion positions. The formulas used are:

$$\vec{x}(t+\delta t) = \vec{x}(t) + \vec{u}(t+\frac{\delta t}{2})\Delta t \tag{2.15}$$

$$\vec{u}(t+\frac{\delta t}{2}) = \vec{u}(t-\frac{\delta t}{2}) + \frac{q\vec{E}(t)}{M}\Delta t \tag{2.16}$$

Since velocities are calculated in cartesian coordinates, after each position update, the velocity vector must be rotated back to the $(r, z, \theta = 0)$ plane.

2.3.2 Shape factors

To evaluate particle density at each timestep, the macroparticle weights are distributed to the nodes of a cartesian grid using a combination of radial and axial shape factors. In the axial direction, linear interpolation is used to obtain the proper shape factor as follows:

$$S_i = \frac{z_{i+1} - z}{z_{i+1} - z_i} \tag{2.17}$$

$$S_{i+1} = \frac{z - z_i}{z_{i+1} - z_i} = 1 - S_i \tag{2.18}$$

In the radial direction, the following shape factors, specified by *Ruyten* (1993), are used to conserve charge density:

$$S_j = \frac{(r_{j+1} - r)(2r_{j+1} + 3r_j - r)}{2(r_{j+1}^2 - r_j^2)} \tag{2.19}$$

$$S_{j+1} = \frac{(r - r_j)(3r_{j+1} + 2r_j - r)}{2(r_{j+1}^2 - r_j^2)} = 1 - S_j \tag{2.20}$$

Once the shape factors are known for a given macroparticle, its contribution to a given node is the product of the macroparticle weight and the two relevant shape factors.

2.3.3 Particle injection

Neutral macroparticles (typically 6-10 per iteration) are introduced into the simulation at the anode at every timestep. These macroparticles are created with a Maxwellian velocity distribution corresponding to an anode reservoir temperature of 1000 K. (The anode is presumed to reach thermal equilibrium around this temperature.) If a finite neutral backpressure is desired, then neutral macroparticles are also injected inwards across the domain exit with a Maxwellian velocity distribution corresponding to a vacuum tank temperature of 300 K. The velocity distribution sampling routine used in both cases can be found in Appendix B.

All ion macroparticles in the simulation are the result of ionization events occuring inside the computational domain. The direct coupling of neutrals and ions through the MCC algorithm described in Sec. 2.4 ensures strict mass conservation throughout the computational domain.

2.3.4 Boundary interaction

Neutral macroparticles undergo full thermal accommodation when they strike any thruster surface (thick lines in Fig. 2.3). Similarly, ion macroparticles recombine to form fully accommodated neutral macroparticles when they hit any thruster surface. The thruster body is assumed to be at a temperature of 1000 K for all simulations. Experimental data by *Massey et al.* (2004) indicates slightly lower temperatures in the acceleration channel (from 650 K to 900 K). The velocity distribution routine from Appendix B is also used for wall interactions.

At the domain exit (both along the top and far end of the simulation domain), macroparticles of all types can exit the simulation domain. Once a macroparticle leaves the simulation domain, its contribution to the performance of the thruster is catalogued and then it is deleted. Finally, a radial symmetry condition is used along the thruster centerline outside the acceleration channel.

2.4 Ionization algorithm

2.4.1 Ground state ionization

Neutral depletion due to ground state ionization is calculated using a Monte Carlo Collision (MCC) model (*Birdsall and Langdon* (1991)). The first step for each neutral macroparticle is to evaluate the probability of an $e^- + Xe \rightarrow 2e^- + Xe^+$ collision based on the local plasma density, electron energy and timestep. This probability, P_C (generally $<< 1$), is calculated as follows:

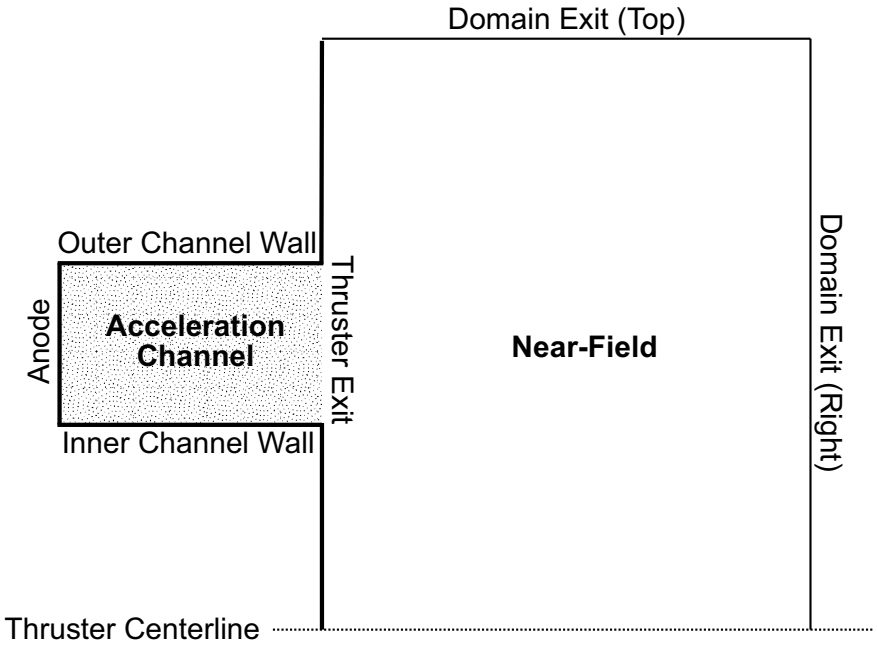


Figure 2.3: Hall Thruster Boundary Schematic

$$P_C = n_e k^i_{Xe^+}(\varepsilon)\Delta t \tag{2.21}$$

Next, the neutral macroparticle is assigned a random number from 0 to 1. If this random number is less than P_C, then a collision event is simulated and the neutral macroparticle is changed into a singly charged ion macroparticle with the same physical properties (particle weight, location, velocity) as the parent neutral macroparticle.

If the neutral macroparticle survives this test, then a second collision probability, representing an $e^- + Xe \rightarrow 3e^- + Xe^{++}$ collision, is calculated as follows:

$$P_C = n_e k^i_{Xe^{++}}(\varepsilon)\Delta t \tag{2.22}$$

Next, the neutral macroparticle is assigned another random number from 0 to 1. If this random number is less than P_C, then a collision event is simulated and the

neutral macroparticle is changed into a doubly charged ion macroparticle with the same physical properties as the parent neutral macroparticle.

The actual ground state ionization rates used in the computational model are from *Garrigues et al.* (2001) and are presented in Fig. C.1 and Fig. C.3 for xenon and krypton, respectively.

2.4.2 Stepwise ionization

To calculate neutral depletion due to stepwise ionization, an MCC model is again used. As in ground state ionization, for each Xe^+ macroparticle, the collision probability P_C of an $e^- + Xe^+ \rightarrow 2e^- + Xe^{++}$ collision, based on the local plasma density, electron energy and timestep, is calculated as follows:

$$P_C = n_{Xe^+} k^i_{stepwise}(\varepsilon)\Delta t \tag{2.23}$$

The Xe^+ macroparticle is assigned a random number from 0 to 1. If this random number is less than P_C, then a collision event is simulated and the singly charged ion macroparticle is changed into a doubly charged ion macroparticle with the same physical properties.

The stepwise ionization rates used in the computational model are from *Garrigues et al.* (2001) and are presented in Fig. C.1 and Fig. C.3 for xenon and krypton, respectively.

2.4.3 Collision multiplier technique

In practice, since the ionization probability for very small timesteps is quite low ($1 \cdot 10^{-6} \geq P_c \geq 1 \cdot 10^{-9}$), the number of ion macroparticles generated in many of the computational simulations (< 1 ion macroparticle per cell) is well below the minimum number required for acceptable particle statistics ($\sim 10-25$ macroparticles

per cell). In order to alleviate this problem, a collision multiplier technique is applied to the MCC algorithm.

The collision multiplier, γ, increases the likelihood of a successful collision process by increasing the sampling frequency and decreasing the collision magnitude. The local collision probability, P_C, is increased by this collision multiplier to form a modified collision probability, P_C^* as follows:

$$P_C^* = \gamma P_C \tag{2.24}$$

This modified collision probability is used in the same sense as the original collision probability to evaluate whether or not an ionization collision occurs; however, the outcome of such a collision is not to completely change the macroparticle species, but rather to split the original macroparticle into two smaller macroparticles. By lowering the numerical weight of the collision product in this manner, the probability of collisions is increased by a factor of γ. The two daughter macroparticles are created with the same position and velocity as the parent macroparticle but with different particle weights. The daughter macroparticle of the same species as the parent retains $\frac{\gamma-1}{\gamma}$ of the parent macroparticle weight while the daughter macroparticle of the new species is created with $\frac{1}{\gamma}$ of the macroparticle weight.

2.4.3.1 Choosing the Collision Multiplier

At the beginning of a simulation, an initial collision multiplier is required as an input. This inital collision multiplier (typically between 2 and 16) must be chosen carefully to ensure that the ion macroparticle count does not increase too rapidly as a function of time. In order to ensure that the ion macroparticle count remains high enough for statistical accuracy, for some periods of the simulation, the collision

multiplier must be elevated even further. To accomplish this while ensuring that the individual macroparticle weighting varies as smoothly as possible, the following algorithm is used:

$$P_C^* = \gamma^* P_C \tag{2.25}$$

$$\gamma^* = \frac{\sqrt{\gamma P_C}}{P_C} \tag{2.26}$$

Again, the daughter macroparticle fraction must be weighted properly to ensure that the overall particle count is maintained. In this case, the daughter macroparticle of the same species as the parent retains $\frac{\gamma^*-1}{\gamma^*}$ of the parent macroparticle weight while the daughter macroparticle of the new species is created with $\frac{1}{\gamma^*}$ of the macroparticle weight. For more discussion on this algorithm, see Sec. 3.6.1.

2.5 1-D Ohm's law

The electric field in a Hall thruster can be reasonably approximated to be two-dimensional in the $r-z$ plane. Through discretization of this domain using magnetic field lines, it is possible to calculate the electric field using a 1-D version of Ohm's Law. This formulation is based on the assumption that there is no charge buildup in the thruster during operation. Since there are no sources or sinks in the device, then the total current through the device must, at every moment, be the same throughout. This implies that through any magnetic field line which reaches from the inner to the outer wall of the thruster, the total current must be identically equal to the total current through any other field line reaching from the inner to the outer wall of the thruster. The 1-D Ohm's Law equation is solved from the virtual anode line (λ_a) to the virtual cathode line (λ_c) as shown in Sec. 3.4.

2.5.1 Electron current density

The electron current density perpendicular to the magnetic field is a combination of an electron drift term (caused by the electric field) and an electron diffusion term (caused by the pressure forces). It is written as:

$$j_{e_\perp} = en_e\mu E_\perp + \frac{eD_m}{kT_e}\nabla_\perp p_e \tag{2.27}$$

where,

$$p_e = n_e k_B T_e \tag{2.28}$$

The diffusivity and the mobility are related by the well known Einstein relationship as follows:

$$\frac{D_m}{\mu} = \frac{kT_e}{e} \tag{2.29}$$

Now the electron current density can be written in terms of the conductivity as follows:

$$j_{e_\perp} = \sigma(E_\perp + \frac{1}{n_e e}\nabla_\perp p_e) \tag{2.30}$$

where,

$$E_\perp = -\frac{\partial\phi}{\partial\hat{n}} \tag{2.31}$$

and mobility, μ, is related to the conductivity, σ, by the following relationship:

$$\sigma = en_e\mu \tag{2.32}$$

Next, take the thermalized potential:

$$\phi^* = \phi - \frac{k_B T_e}{e} ln\left(\frac{n_e}{{n_e}^*}\right) \tag{2.33}$$

where ${n_e}^*$ is a reference plasma density (typically chosen to be $1 \cdot 10^{12}$ $[\frac{\#}{m^3}]$) and evaluate the derivative normal to the magnetic field to obtain:

$$\frac{\partial \phi^*}{\partial \hat{n}} = \frac{\partial \phi}{\partial \hat{n}} - \frac{k_B T_e}{e}\frac{\partial ln(n_e)}{\partial \hat{n}} - \frac{k_B}{e}\frac{\partial T_e}{\partial \hat{n}} ln\left(\frac{n_e}{{n_e}^*}\right) \tag{2.34}$$

This can be used to reformulate Eqn. 2.30 into:

$$j_{e_\perp} = \sigma(-\frac{\partial \phi^*}{\partial \hat{n}} - \frac{k_B T_e}{e}\frac{\partial ln(n_e)}{\partial \hat{n}} - \frac{k_B}{e}\frac{\partial T_e}{\partial \hat{n}}\left(\frac{n_e}{{n_e}^*}\right) + \frac{1}{ne}\frac{\partial n k_B T_e}{\partial \hat{n}}) \tag{2.35}$$

Expanding the last term and cancelling terms gives:

$$j_{e_\perp} = \sigma(-\frac{\partial \phi^*}{\partial \hat{n}} - [ln\left(\frac{n_e}{{n_e}^*}\right) - 1]\frac{k}{e}\frac{\partial T_e}{\partial \hat{n}}) \tag{2.36}$$

Next, it is possible to use Eqn. 2.8 to obtain:

$$j_{e_\perp} = \sigma r B(-\frac{\partial \phi^*}{\partial \lambda} - [ln\left(\frac{n_e}{{n_e}^*}\right) - 1]\frac{k}{e}\frac{\partial T_e}{\partial \lambda}) \tag{2.37}$$

The final form for the electron current density used in the code is as follows:

$$j_{e_\perp} = e n_e \mu r B(-\frac{\partial \phi^*}{\partial \lambda} - [ln\left(\frac{n_e}{{n_e}^*}\right) - 1]\frac{k}{e}\frac{\partial T_e}{\partial \lambda}) \tag{2.38}$$

2.5.2 Ion current

The ion current through a given field line can be calculated by integrating the contribution of the ion macroparticles. The final form of the ion current is:

$$I_i = \int_S e n_i u_{i,\perp} \, \partial S \tag{2.39}$$

Note that the ion drift current must be changed to reflect the contribution of the Xe^{++} ions.

$$I_i = \int_S e n_i u_i \, \partial S = \int_S e(n_i u_{i,\perp})_{Xe^+} \, \partial S + \int_S 2e(n_i u_{i,\perp})_{Xe^{++}} \, \partial S$$

2.5.3 Current conservation

The total current through a given field line is the sum of the electron and ion currents as shown below:

$$\begin{aligned} I_T &= \int_S j_e \, \partial S + \int_S j_i \, \partial S \\ &= \int_S e n_e \mu r B (-\frac{\partial \phi^*}{\partial \lambda} - [ln\left(\frac{n_e}{{n_e}^*}\right) - 1]\frac{k_B}{e}\frac{\partial T_e}{\partial \lambda}) \, \partial S + \int_S e n_i u_i \, \partial S \end{aligned} \tag{2.40}$$

Along a given field line, derivatives with respect to λ are constant, so:

$$I_T = -\frac{\partial \phi^*}{\partial \lambda} \int_S e n_e \mu r B \, \partial S - \int_S e n_e \mu r B [ln\left(\frac{n_e}{{n_e}^*}\right) - 1]\frac{k_B}{e}\frac{\partial T_e}{\partial \lambda} \, \partial S + \int_S e n_i u_i \, \partial S \tag{2.41}$$

Now rearrange as follows:

$$\frac{\partial \phi^*}{\partial \lambda} = -I_T \frac{1}{\int_S e n_e \mu r B \, \partial S} - \frac{\int_S e n_e \mu r B [ln\left(\frac{n_e}{{n_e}^*}\right) - 1]\frac{k_B}{e}\frac{\partial T_e}{\partial \lambda} \, \partial S}{\int_S e n_e \mu r B \, \partial S} + \frac{\int_S e n_i u_i \, \partial S}{\int_S e n_e \mu r B \, \partial S} \tag{2.42}$$

Summation can be performed over the 1-D domain as follows:

$$\sum_{\lambda=\lambda_a}^{\lambda_c} \frac{\partial \phi^*}{\partial \lambda} d\lambda = -\sum_{\lambda=\lambda_a}^{\lambda_c} I_T \frac{1}{\int_S e n_e \mu r B \; \partial S} d\lambda - \sum_{\lambda=\lambda_a}^{\lambda_c} \frac{\int_S e n_e \mu r B [ln\left(\frac{n_e}{n_e{}^*}\right) - 1] \frac{k_B}{e} \frac{\partial T_e}{\partial \lambda} \; \partial S}{\int_S e n_e \mu r B \; \partial S} d\lambda + \sum_{\lambda=\lambda_a}^{\lambda_c} \frac{\int_S e n_i u_i \; \partial S}{\int_S e n_e \mu r B \; \partial S} d\lambda \tag{2.43}$$

Since the total current I_T is a constant across all field lines, it can be moved outside of the sum as follows:

$$\phi^*(\lambda_c) - \phi^*(\lambda_a) = -I_T \sum_{\lambda=\lambda_a}^{\lambda_c} \frac{1}{\int_S e n_e \mu r B \; \partial S} d\lambda - \sum_{\lambda=\lambda_a}^{\lambda_c} \frac{\int_S e n_e \mu r B [ln\left(\frac{n_e}{n_e{}^*}\right) - 1] \frac{k_B}{e} \frac{\partial T_e}{\partial \lambda} \; \partial S}{\int_S e n_e \mu r B \; \partial S} d\lambda + \sum_{\lambda=\lambda_a}^{\lambda_c} \frac{\int_S e n_i u_i \; \partial S}{\int_S e n_e \mu r B \; \partial S} d\lambda \tag{2.44}$$

Since every variable is known except for the total current, I_T, Eqn. 2.44 represents a closed form solution for the total current. This result can then be used to retrieve the thermalized potential gradient and, eventually, the full 1-D thermalized potential. Using the concept of the thermalized potential to evaluate the electrostatic potential along magnetic field lines, it is further possible to retrieve the complete electrostatic potential throughout the 2-D domain. Finally, the electric field can be found through evaluation of the familiar relation:

$$\vec{E} = -\nabla \phi \tag{2.45}$$

2.5.4 Electron mobility

The classical formulation for electron mobility perpendicular to magnetic field lines is:

$$\mu_{e,\perp} = \frac{e}{m\nu_m} \frac{1}{1 + \frac{\omega_{B,e}^2}{\nu_m^2}} \tag{2.46}$$

where the electron cyclotron frequency is written as:

$$\omega_{B,e} = \frac{eB}{m_e} \tag{2.47}$$

and the the electron-neutral collision frequency is evaluated as:

$$\nu_m = n_a \times 2.5 \cdot 10^{-13} \tag{2.48}$$

The dominant collision term, the electron momentum transfer frequency, ν_m is taken to be the frequency of electron-neutral collisions (ν_{neut}). However, the electron mobility obtained by this procedure is not sufficient to reproduce experimental results. As a consequence, an additional "anomalous electron transport" is provided through augmentation of the electron momentum transfer frequency. Two models for this additional term are presented below. These models can be used as a stand alone mobility model throughout the domain or can be used concurrently in different regions of the thruster.

2.5.4.1 Wall-Collision Approach

The wall-collision correction to the ν_m term, based on the idea that electrons collide with the sheath with a relative frequency based on their thermal energy and the height of the acceleration channel, was used by *Boeuf and Garrigues* (1998). A simple form for this correction can be obtained by using an *a priori* averaged thermal

energy to calculate a global wall-collision rate. For these computations, the modified form of the electron momentum transfer frequency (with wall-collisions), where α is a coefficient matched with the equivalent wall-energy loss coefficient, is:

$$\nu_m = \nu_{neut} + \alpha \cdot 10^7 \tag{2.49}$$

2.5.4.2 Bohm Diffusion Approach

The Bohm diffusion correction to the ν_m term is based on the idea that anomalous Bohm diffusion drives the additional electron mobility observed experimentally. For these computations, the modified form of the electron momentum transfer frequency (with Bohm diffusion), where α_B is an empirically chosen coefficient, is as follows:

$$\nu_m = \nu_{neut} + \alpha_B \omega_{B,e} \tag{2.50}$$

2.6 Electron energy equation

The electrons in Hall thrusters move orders of magnitude faster than the ions due to their extremely low inertia relative to the heavy particles. As a consequence, they collide rapidly both with each other and with the acceleration channel walls. The balance between thermalizing and non-thermalizing collisions determines whether or not the electron distribution function approaches a Maxwellian.

Work by *Latocha et al.* (2002) demonstrates that even though the distribution function of electrons in a Hall thruster is not classically Maxwellian, the resulting ionization and energy loss rates correlate well to the behavior of a Maxwellian distribution at the same averaged energy. Similar work by *Boyd* (2003), considering crossed electric and magnetic fields, ionization collisions with neutral atoms, and interactions

with dielectric walls, indicates only a marginal perturbation from a Maxwellian electron energy distribution.

Based on these studies, the form of the electron energy equation used in this model is founded on the assumption that the electron energy distribution behaves similarly enough to a Maxwellian to justify the use of a local single fluid approximation with the single parameter of energy to describe the electron energy distribution function.

The implementation of this equation (as detailed in this section) is heavily influenced by *Fife* (1998). The form of the electron energy equation involves an advection-diffusion term on the LHS and ohmic heating and energy loss on the RHS as follows:

$$\frac{\partial}{\partial t}(\frac{3}{2}n_e k_B T_e) + \nabla \cdot (\frac{5}{2}n_e k_B T_e \vec{u_e} + \vec{q_e}) = S_h - S_i \tag{2.51}$$

where

$$\vec{q_e} = -K_e \nabla T_e \tag{2.52}$$

$$S_h = \vec{j_e} \cdot \vec{E} = -n_e e \vec{u_e} \cdot \vec{E} \tag{2.53}$$

$$S_i = n_e e \varepsilon \nu(\varepsilon) \tag{2.54}$$

Here, S_h represent ohmic heating and S_i represents the inelastic energy losses (both ionization and other inelastic processes). It is possible to express the thermal conductivity in terms of the thermal diffusivity for a monatomic species as follows:

$$K_e = \rho c_p D_h = \frac{5}{2} n k_B D_h \tag{2.55}$$

By equating the heat diffusion coefficient and mass diffusion coefficient as demonstrated by *Fife* (1998), it is possible to show that:

$$K_e = \frac{5 n_e k_B^2 T_e \mu_{e,\perp}}{2e} \tag{2.56}$$

Now the electron energy equation can be rearranged to read:

$$\frac{\partial}{\partial t}(\frac{3}{2} n_e k_B T_e) + \nabla \cdot (\frac{5}{2} n_e k_B T_e \vec{u_e} - \frac{5 n_e k_B^2 T_e \mu_{e,\perp}}{2e} \nabla T_e) = -n_e e \vec{u_e} \cdot \vec{E} - n_e e \varepsilon \nu(\varepsilon) \tag{2.57}$$

The following relationship between the mean electron energy ε (eV) and the electron temperature T_e (K) is used throughout the thesis:

$$\varepsilon e = \frac{3}{2} k_B T_e \tag{2.58}$$

it is possible to obtain:

$$\frac{\partial}{\partial t}(n_e \varepsilon e) + \nabla \cdot (\frac{5}{3} n_e e \varepsilon \vec{u_e} - \frac{10 n_e \mu_{e,\perp} \varepsilon e}{9} \nabla \varepsilon) = -n_e e \vec{u_e} \cdot \vec{E} - n_e e \varepsilon \nu(\varepsilon) \tag{2.59}$$

Now cancel the e's to retrieve the complete electron energy loss equation shown below:

$$\frac{\partial}{\partial t}(n_e \varepsilon) + \nabla \cdot (\frac{5}{3} n_e \varepsilon \vec{u_e} - \frac{10 n_e \mu_{e,\perp} \varepsilon}{9} \nabla \varepsilon) = -n_e \vec{u_e} \cdot \vec{E} - n_e \varepsilon \nu(\varepsilon) \tag{2.60}$$

2.6.1 Volume integration

Simply evaluating the differential equation describing the electron energy along the centerline of the thruster both ignores the contribution of the plasma off the centerline and leads to numerical stability problems. By volume integrating the

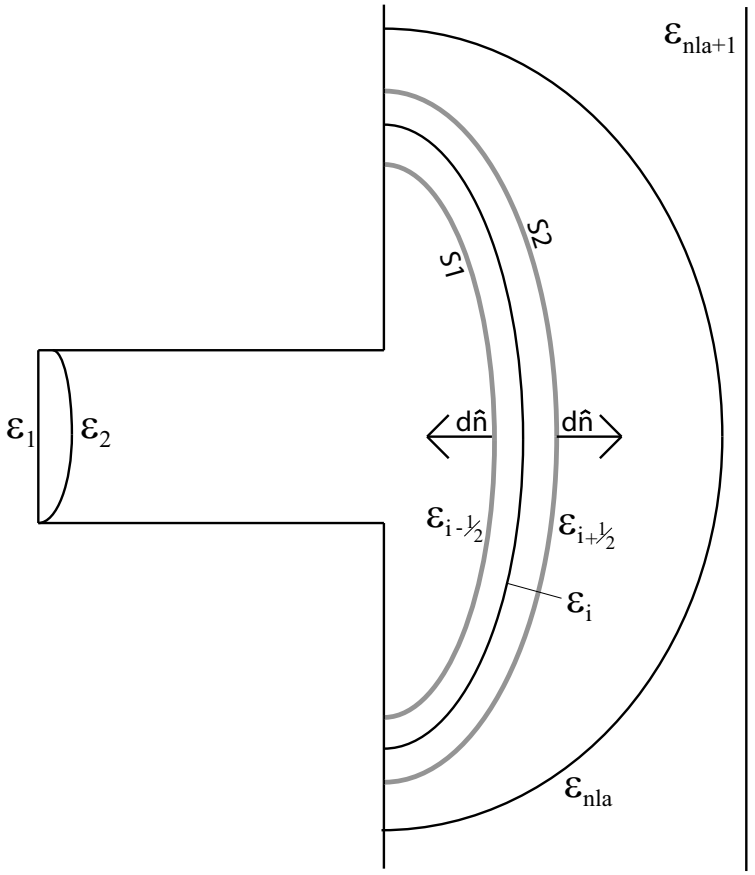


Figure 2.4: Electron energy equation geometry – Bottom of picture represents thruster centerline.

electron energy equation over each slice of the domain in Fig. 2.4, it is possible to recognize the contribution of the entire plasma field while also better conditioning the numerical properties of the equation.

Note: S1 integrals are evaluated on the surface marked $\varepsilon_{i-\frac{1}{2}}$ and S2 integrals are evaluated at the surface marked $\varepsilon_{i+\frac{1}{2}}$. Volume integrals are evaluated over the volume centered at ε_i. The integrated form of the electron energy equation is as follows:

$$\iiint \frac{\partial}{\partial t}(n_e\varepsilon)\ d\mathcal{V} + \iiint \nabla\cdot(\frac{5}{3}n_e\varepsilon\vec{u_e})\ d\mathcal{V} - \iiint \nabla\cdot(\frac{10n_e\mu_{e,\perp}\varepsilon}{9}\nabla\varepsilon)\ d\mathcal{V}$$
$$= -\iiint n_e\vec{u_e}\cdot\vec{E}\ d\mathcal{V} - \iiint n_e\varepsilon\nu(\varepsilon)\ d\mathcal{V} \quad (2.61)$$

2.6.2 Discretization

Since $\vec{u}_{e,\hat{n}}$ and $\vec{E}_{\hat{n}}$ can be written as functions of ε, it is possible to write an ordinary differential equation for the electron energy. This effort is justified by the ability to subcycle the electron energy equation while needing to update only the electron energy loss coefficient.

Electron Velocity

Begin with the form of the electron velocity previously used to calculate the electron current:

$$\vec{u}_{e,\hat{n}} = \mu_{e,\perp}rB\left(\frac{\partial\phi^*}{\partial\lambda} + [ln\left(\frac{n_e}{n_e^*}\right) - 1]\frac{2}{3}\frac{\partial\varepsilon}{\partial\lambda}\right)$$
$$= k_1\frac{\partial\phi^*}{\partial\lambda} + k_2\frac{\partial\varepsilon}{\partial\lambda} \quad (2.62)$$
$$k_1 = \mu_{e,\perp}rB \quad (2.63)$$
$$k_2 = [ln\left(\frac{n_e}{n_e^*}\right) - 1]\frac{2}{3}\mu_{e,\perp}rB \quad (2.64)$$

Further, $\frac{\partial\phi^*}{\partial\lambda}$ is also a function of ε as follows:

$$\frac{\partial\phi^*}{\partial\lambda} = \frac{-I_T + \int enu_i\ d\mathcal{S}}{\int en\mu_{e,\perp}rB\ d\mathcal{S}} - \frac{\int en_e\mu_{e,\perp}rB[ln\left(\frac{n_e}{n_e^*}\right) - 1]\frac{2}{3}\frac{\partial\varepsilon}{\partial\lambda}\ d\mathcal{S}}{\int en\mu_{e,\perp}rB\ d\mathcal{S}}$$
$$= j_1 + j_2\frac{\partial\varepsilon}{\partial\lambda} \quad (2.65)$$

$$j_1 = \frac{-I_T + \int en_e u_i \; d\mathcal{S}}{\int en_e \mu_{e,\perp} rB \; d\mathcal{S}} \tag{2.66}$$

$$j_2 = \frac{\int en_e \mu_{e,\perp} rB[ln\left(\frac{n_e}{n_e^*}\right) - 1]^{\frac{2}{3}} \; d\mathcal{S}}{\int en_e \mu_{e,\perp} rB \; d\mathcal{S}} \tag{2.67}$$

This leads to the following expression for $\vec{u}_e$:

$$\vec{u}_{e,\hat{n}} = k_1 \frac{\partial \phi^*}{\partial \lambda} + k_2 \frac{\partial \varepsilon}{\partial \lambda} \tag{2.68}$$

$$= k_1(j_1 + j_2 \frac{\partial \varepsilon}{\partial \lambda}) + k_2 \frac{\partial \varepsilon}{\partial \lambda} \tag{2.69}$$

$$= k_1 j_1 + (k_1 j_2 + k_2) \frac{\partial \varepsilon}{\partial \lambda} \tag{2.70}$$

Electric Field

Begin with the following formula for the electric field perpendicular to the magnetic field lines:

$$\begin{aligned} \vec{E}_{\hat{n}} &= -\frac{\partial \phi}{\partial \hat{n}} \\ &= -\frac{\partial \phi^*}{\partial \hat{n}} - \frac{2}{3}\varepsilon \frac{\partial ln(n_e)}{\partial \hat{n}} - \frac{2}{3}\frac{\partial \varepsilon}{\partial \hat{n}} ln\left(\frac{n_e}{n_e^*}\right) \\ &= -rB\frac{\partial \phi^*}{\partial \lambda} - \frac{2}{3}rB\frac{\partial ln(n_e)}{\partial \lambda}\varepsilon - \frac{2}{3}rBln\left(\frac{n_e}{n_e^*}\right)\frac{\partial \varepsilon}{\partial \lambda} \\ &= h_1 \frac{\partial \phi^*}{\partial \lambda} + h_2 \varepsilon + h_3 \frac{\partial \varepsilon}{\partial \lambda} \end{aligned} \tag{2.71}$$

$$h_1 = -rB \tag{2.72}$$

$$h_2 = -\frac{2}{3}rB\frac{\partial ln(n_e)}{\partial \lambda} \tag{2.73}$$

$$h_3 = -\frac{2}{3}rBln\left(\frac{n_e}{n_e^*}\right) \tag{2.74}$$

Substituting for $\frac{\partial \phi^*}{\partial \lambda}$ leads to:

$$\begin{aligned}\vec{E}_{\hat{n}} &= h_1 \left(j_1 + j_2 \frac{\partial \varepsilon}{\partial \lambda} \right) + h_2 \varepsilon + h_3 \frac{\partial \varepsilon}{\partial \lambda} \\ &= h_1 j_1 + (h_1 j_2 + h_3) \frac{\partial \varepsilon}{\partial \lambda} + h_2 \varepsilon \end{aligned} \tag{2.75}$$

First Term

The first term from Eqn. 2.61 becomes:

$$\begin{aligned}\iiint \frac{\partial}{\partial t}(n_e \varepsilon) \, d\mathcal{V} &= \iiint n_e \frac{\partial \varepsilon}{\partial t} \, d\mathcal{V} + \iiint \varepsilon \frac{\partial n_e}{\partial t} \, d\mathcal{V} \\ &= \left[\iiint n_e d\mathcal{V} \right] \, \frac{\partial \varepsilon}{\partial t} + \left[\iiint \frac{\partial n_e}{\partial t} d\mathcal{V} \right] \, \varepsilon \\ &= A_1 \frac{\partial \varepsilon_V}{\partial t} + A_2 \varepsilon_V \end{aligned} \tag{2.76}$$

$$A_1 = \left[\iiint n_e d\mathcal{V} \right] \tag{2.77}$$

$$A_2 = \left[\iiint \frac{\partial n_e}{\partial t} d\mathcal{V} \right] \tag{2.78}$$

Second Term

Use the divergence theorem and $\vec{u}_{e,\hat{n}}$ on the second term from Eqn. 2.61 to obtain:

$$\begin{aligned}\iiint \nabla \cdot (\frac{5}{3} n_e \varepsilon \vec{u_e}) \, d\mathcal{V} &= \iint (\frac{5}{3} n_e \varepsilon \vec{u_e}) \cdot \hat{n} \, d\mathcal{S} = \iint \frac{5}{3} n_e \varepsilon \vec{u}_{e,\hat{n}} \, d\mathcal{S} \\ &= \int \frac{5}{3} n_e k_1 j_1 \varepsilon \, d\mathcal{S} + \int \frac{5}{3} n_e (k_1 j_2 + k_2) \epsilon \frac{\partial \epsilon}{\partial \lambda} \, d\mathcal{S} \\ &= \left[\int -\frac{5}{3} n_e k_1 j_1 \, d\mathcal{S} \right]_{S1} \varepsilon_{S1} \end{aligned}$$

$$
\begin{aligned}
&+\left[\int -\frac{5}{3}n_e(k_1j_2+k_2)\ d\mathcal{S}\right]_{S1}\left(\epsilon\frac{\partial\epsilon}{\partial\lambda}\right)_{S1}\\
&+\left[\int \frac{5}{3}n_ek_1j_1\ d\mathcal{S}\right]_{S2}\varepsilon_{S2}\\
&+\left[\int \frac{5}{3}n_e(k_1j_2+k_2)\ d\mathcal{S}\right]_{S2}\left(\epsilon\frac{\partial\epsilon}{\partial\lambda}\right)_{S2}\\
=&A_3\varepsilon_{S1}+A_4\left(\epsilon\frac{\partial\epsilon}{\partial\lambda}\right)_{S1}+A_5\varepsilon_{S2}+A_6\left(\epsilon\frac{\partial\epsilon}{\partial\lambda}\right)_{S2} \qquad (2.79)
\end{aligned}
$$

$$A_3=\left[\int -\frac{5}{3}n_ek_1j_1\ d\mathcal{S}\right]_{S1} \qquad (2.80)$$

$$A_4=\left[\int -\frac{5}{3}n_e(k_1j_2+k_2)\ d\mathcal{S}\right]_{S1} \qquad (2.81)$$

$$A_5=\left[\int \frac{5}{3}n_ek_1j_1\ d\mathcal{S}\right]_{S2} \qquad (2.82)$$

$$A_6=\left[\int \frac{5}{3}n_e(k_1j_2+k_2)\ d\mathcal{S}\right]_{S2} \qquad (2.83)$$

Third Term

Again, use the divergence theorem on the third term from Eqn. 2.61 to obtain:

$$
\begin{aligned}
\iiint \nabla\cdot(\frac{10n_e\mu_{e,\perp}\varepsilon}{9}\nabla\varepsilon)\ d\mathcal{V}&=\iint(\frac{10n_e\mu_{e,\perp}\varepsilon}{9}\nabla\varepsilon)\cdot\hat{n}\ d\mathcal{S}\\
&=\iint(\frac{10n_e\mu_{e,\perp}\varepsilon}{9}rB\frac{\partial\varepsilon}{\partial\lambda}\hat{n})\cdot\hat{n}\ d\mathcal{S}\\
&=\left[\iint\frac{-10n_e\mu_{e,\perp}rB}{9}\ d\mathcal{S}\right]_{S1}\left(\varepsilon\frac{\partial\varepsilon}{\partial\lambda}\right)_{S1}\\
&\quad+\left[\iint\frac{10n_e\mu_{e,\perp}rB}{9}\ d\mathcal{S}\right]_{S2}\left(\varepsilon\frac{\partial\varepsilon}{\partial\lambda}\right)_{S2}\\
&=A_7\left(\varepsilon\frac{\partial\varepsilon}{\partial\lambda}\right)_{S1}+A_8\left(\varepsilon\frac{\partial\varepsilon}{\partial\lambda}\right)_{S2} \qquad (2.84)
\end{aligned}
$$

$$A_7=\left[\iint\frac{-10n_e\mu_{e,\perp}rB}{9}\ d\mathcal{S}\right]_{S1} \qquad (2.85)$$

$$A_8=\left[\iint\frac{10n_e\mu_{e,\perp}rB}{9}\ d\mathcal{S}\right]_{S2} \qquad (2.86)$$

Fourth Term

The fourth term from Eqn. 2.61 with correct $\vec{u}_{e,\hat{n}}$ and $\vec{E}_{\hat{n}}$ substitutions is:

$$\begin{aligned}
\iiint n_e \vec{u_e} \cdot \vec{E}\ d\mathcal{V} = &\iiint n_e \left(k_1 j_1 + (k_1 j_2 + k_2)\frac{\partial \varepsilon}{\partial \lambda}\right) \\
&\cdot \left(h_1 j_1 + (h_1 j_2 + h_3)\frac{\partial \varepsilon}{\partial \lambda} + h_2 \varepsilon\right)\ d\mathcal{V} \\
= &\iiint [n_e k_1 j_1 h_1 j_1] + [n_e k_1 j_1 (h_1 j_2 + h_3) + n_e (k_1 j_2 + k_2) h_1 j_1]\frac{\partial \varepsilon}{\partial \lambda} \\
&+ [n_e (k_1 j_2 + k_2)(h_1 j_2 + h_3)]\frac{\partial \varepsilon}{\partial \lambda}\frac{\partial \varepsilon}{\partial \lambda} + [n_e (k_1 j_2 + k_2) h_2]\frac{\partial \varepsilon}{\partial \lambda}\varepsilon \\
&+ [n_e k_1 j_1 h_2]\varepsilon\ d\mathcal{V} \\
= &A_9 + A_{10}\frac{\partial \varepsilon_V}{\partial \lambda} + A_{11}\frac{\partial \varepsilon_V}{\partial \lambda}\frac{\partial \varepsilon_V}{\partial \lambda} + A_{12}\left(\frac{\partial \varepsilon}{\partial \lambda}\varepsilon\right)_V + A_{13}\varepsilon_V \qquad (2.87)
\end{aligned}$$

$$A_9 = \left[\iiint n_e k_1 j_1 h_1 j_1\ d\mathcal{V}\right] \qquad (2.88)$$

$$A_{10} = \left[\iiint n_e k_1 j_1 (h_1 j_2 + h_3) + n_e (k_1 j_2 + k_2) h_1 j_1\ d\mathcal{V}\right] \qquad (2.89)$$

$$A_{11} = \left[\iiint n_e (k_1 j_2 + k_2)(h_1 j_2 + h_3)\ d\mathcal{V}\right] \qquad (2.90)$$

$$A_{12} = \left[\iiint n_e (k_1 j_2 + k_2) h_2\ d\mathcal{V}\right] \qquad (2.91)$$

$$A_{13} = \left[\iiint n_e k_1 j_1 h_2\ d\mathcal{V}\right] \qquad (2.92)$$

Fifth Term

Finally, the last term from Eqn. 2.61 is:

$$\begin{aligned}
\iiint n_e \varepsilon \nu(\varepsilon)\ d\mathcal{V} = &\left[\iiint n_e \nu(\varepsilon) d\mathcal{V}\right] \varepsilon_V \\
= &\left[\iiint n_e (\nu(\varepsilon)_{e-Xe} + \nu(\varepsilon)_{walls} + \nu(\varepsilon)_{e-Xe^+}) d\mathcal{V}\right] \varepsilon_V
\end{aligned}$$

$$= A_{14} k_{e-Xe}(\varepsilon_V)\varepsilon_V + A_{15}\nu(\varepsilon_V)_{walls}\varepsilon_V + A_{16} k_{e-Xe^+}(\varepsilon_V)\varepsilon_V \quad (2.93)$$

$$A_{14} = \left[\iiint n_e n_a \, d\mathcal{V}\right] \quad (2.94)$$

$$A_{15} = \left[\iiint n_e d\mathcal{V}\right] \quad (2.95)$$

$$A_{16} = \left[\iiint n_e n_{Xe^+} \, d\mathcal{V}\right] \quad (2.96)$$

Culmination

Substituting the new discretizations into Eqn. 2.61 provides:

$$\begin{aligned} A_1\frac{\partial \varepsilon_V}{\partial t} + A_2\varepsilon_V + A_3\varepsilon_{S1} + A_4\left(\epsilon\frac{\partial \epsilon}{\partial \lambda}\right)_{S1} + A_5\varepsilon_{S2} + A_6\left(\epsilon\frac{\partial \epsilon}{\partial \lambda}\right)_{S2} - A_7\left(\varepsilon\frac{\partial \varepsilon}{\partial \lambda}\right)_{S1} \\ - A_8\left(\varepsilon\frac{\partial \varepsilon}{\partial \lambda}\right)_{S2} = -A_9 - A_{10}\frac{\partial \varepsilon_V}{\partial \lambda} - A_{11}\frac{\partial \varepsilon_V}{\partial \lambda}\frac{\partial \varepsilon_V}{\partial \lambda} - A_{12}\left(\frac{\partial \varepsilon}{\partial \lambda}\varepsilon\right)_V \\ - A_{13}\varepsilon_V - A_{14}k_{e-Xe}(\varepsilon_V)\varepsilon_V - A_{15}\nu(\varepsilon_V)_{walls}\varepsilon_V - A_{16}k_{e-Xe^+}(\varepsilon_V)\varepsilon_V \quad (2.97) \end{aligned}$$

Divide by A_1 and rearrange as follows:

$$\begin{aligned} \frac{\partial \varepsilon_V}{\partial t} = &- \frac{A_2}{A_1}\varepsilon_V \\ &- \frac{A_3}{A_1}\varepsilon_{S1} \\ &- \frac{A_4}{A_1}\left(\epsilon\frac{\partial \epsilon}{\partial \lambda}\right)_{S1} \\ &- \frac{A_5}{A_1}\varepsilon_{S2} \\ &- \frac{A_6}{A_1}\left(\epsilon\frac{\partial \epsilon}{\partial \lambda}\right)_{S2} \\ &+ \frac{A_7}{A_1}\left(\varepsilon\frac{\partial \varepsilon}{\partial \lambda}\right)_{S1} \\ &+ \frac{A_8}{A_1}\left(\varepsilon\frac{\partial \varepsilon}{\partial \lambda}\right)_{S2} \end{aligned}$$

$$
\begin{aligned}
&- \frac{A_9}{A_1} \\
&- \frac{A_{10}}{A_1}\frac{\partial \varepsilon_V}{\partial \lambda} \\
&- \frac{A_{11}}{A_1}\frac{\partial \varepsilon_V}{\partial \lambda}\frac{\partial \varepsilon_V}{\partial \lambda} \\
&- \frac{A_{12}}{A_1}\left(\frac{\partial \varepsilon}{\partial \lambda}\varepsilon\right)_V \\
&- \frac{A_{13}}{A_1}\varepsilon_V \\
&- \frac{A_{14}}{A_1}k_{e-Xe}(\varepsilon_V)\varepsilon_V \\
&- \frac{A_{15}}{A_1}\nu(\varepsilon_V)_{walls}\varepsilon_V \\
&- \frac{A_{16}}{A_1}k_{e-Xe^+}(\varepsilon_V)\varepsilon_V
\end{aligned} \tag{2.98}
$$

The following discretizations are used in the code:

$$\varepsilon_V = \varepsilon_i \tag{2.99}$$

$$\varepsilon_{S1} = \frac{\varepsilon_i + \varepsilon_{i-1}}{2} \tag{2.100}$$

$$\varepsilon_{S2} = \frac{\varepsilon_i + \varepsilon_{i+1}}{2} \tag{2.101}$$

$$\left(\varepsilon\frac{\partial \varepsilon}{\partial \lambda}\right)_{S1} = \frac{\varepsilon_i + \varepsilon_{i-1}}{2}\frac{\varepsilon_i - \varepsilon_{i-1}}{\lambda} \tag{2.102}$$

$$\left(\varepsilon\frac{\partial \varepsilon}{\partial \lambda}\right)_{S2} = \frac{\varepsilon_i + \varepsilon_{i+1}}{2}\frac{\varepsilon_{i+1} - \varepsilon_i}{\lambda} \tag{2.103}$$

$$\frac{\partial \varepsilon_V}{\partial \lambda} = \frac{\varepsilon_{i+1} - \varepsilon_{i-1}}{2\lambda} \tag{2.104}$$

2.6.3 Electron energy loss term

The loss terms on the right hand side of Eqn. 2.93 represent a number of different physical processes. The basis for each term in the loss term is as follows:

(a) Neutral Losses

$$\nu(\varepsilon)_{e-Xe} = n_a k_{e-Xe}(\varepsilon) \tag{2.105}$$

This term represents the frequency of electron energy loss associated with ionization and excitation from the ground state (for both single and double ionization).

(b) Ion losses

$$\nu(\varepsilon)_{e-Xe^+} = n_{Xe^+} k_{e-Xe^+}(\varepsilon) \tag{2.106}$$

This term represents the electron energy losses associated with stepwise ionization and excitation of Xe^+. The electron energy loss rates used in the computational model are from *Garrigues et al.* (2001) and are presented in Fig. C.2 and Fig. C.4 for xenon and krypton, respectively.

(c) Wall losses

$$\nu(\varepsilon)_{walls} = \alpha \cdot 10^7 \exp\left(\frac{-U_{loss}}{\varepsilon}\right) \tag{2.107}$$

This term represents the frequency of electron energy loss to the walls of the acceleration channel. It is based on a model used by *Boeuf and Garrigues* (1998). This model incorporates two free parameters, α and U_{loss}. These free parameters are held constant during all simulations (with exceptions noted) but different combinations provide noticeably different simulation outcomes. In order to achieve good agreement with experimental measurements, it is almost always necessary to adjust these parameters whenever a different thruster or operating condition is studied.

The α term represents the relative frequency of electron collisions with the dielectric walls. This term can be approximated by calculating the mean thermal speed of electrons in the channel and dividing by the channel height. The U_{loss} term in the exponent represents the electrostatic potential barrier caused by the formation of a dielectric sheath on the channel walls. In effect, this sheath repels low energy electrons (i.e. electrons with energy less than the sheath energy).

2.7 Performance calculation

Thruster performance is calculated by summing the properties of the heavy particles leaving the domain (i.e. beginning the timestep inside the domain and ending the timestep outside the domain). The following formulae are used at each timestep:

Mass Flow Rate

$$\dot{m}_i = M \left[\sum_{boundary} w_{Xe^+} + \sum_{boundary} w_{Xe^{++}} \right] \tag{2.108}$$

$$\dot{m} = M \left[\sum_{boundary} w_{Xe} \right] + \dot{m}_i \tag{2.109}$$

Ion Current

$$I_i = e \sum_{boundary} w_{Xe^+} + 2e \sum_{boundary} w_{Xe^{++}} \tag{2.110}$$

$$\tag{2.111}$$

Thrust

$$T = M \left[\sum_{boundary} (wv_z)_{Xe} + \sum_{boundary} (wv_z)_{Xe^+} + \sum_{boundary} (wv_z)_{Xe^{++}} \right] \tag{2.112}$$

Specific Impulse

$$I_{sp} = \frac{T}{\dot{m} g} \tag{2.113}$$

These values are averaged over time to provide mean performance parameters. Efficiency parameters are calculated based on these mean performance parameters as follows:

Thruster Efficiency

$$\eta = \frac{T^2}{2\dot{m} I_T V_d} \tag{2.114}$$

Propellant Utilization Efficiency

$$\eta_u = \frac{\dot{m}_i}{\dot{m}} \tag{2.115}$$

2.8 Computational requirements

The computational model is compiled with SUN f90 to run on a SunBlade-1500 workstation. A simulation typically contains 50,000-200,000 macroparticles for each charged species and 200,000-500,000 neutral macroparticles on a grid of 2,000-4,000 cells. The heavy particle timestep is limited to the time needed for a perfectly accelerated particle to cross a computational cell (which results in a timestep of

about $5 \cdot 10^{-8}$ seconds for Xe propellant with a discharge voltage of 300 V). Typical solution time is 6-24 hours.

CHAPTER III

Study of Numerical Parameters

3.1 Overview

The complex behavior of this code depends on many factors, including physical modeling choices (such as the electron mobility coefficient), numerical modeling choices (such as the global timestep) and combinations of the two. In theory, physical modeling choices can be validated through comparison with experimental results, while numerical modeling choices should be decoupled from the particular physics of a given thruster simulation. In practice, however, it is nearly impossible to strictly isolate physical modeling choices from numerical modeling choices. Nevertheless, it is possible to qualify the sensitivity of the code to particular numerical modeling choices in order to minimize the projected uncertainty in the simulation results. This chapter presents a series of simulations demonstrating the behavior of this code with respect to the most significant numerical modeling choices.

There are some numerical modeling choices in this code which are well understood throughout the modeling community. In particular, parameters such as the global timestep and physical grid (mesh) spacing are very typical numerical modeling

choices which are studied extensively in classical CFD. For many of these numerical modeling choices, it is possible to demonstrate the existence of a parameter space in which the code produces consistent results.

For other numerical modeling choices unique to this code, the existence of a similar parameter space in which the code produces consistent results is not clear. In particular, the locations of the magnetic field grid boundaries are highly sensitive inputs into the code. The sensitivity of the code results to these parameters is coupled tightly to the particular thruster geometry which is being studied. For these numerical modeling choices, it is possible, at best, only to qualify the sensitivity of the code to these choices.

In evaluating the code, the term "numerical sensitivity" applies to the magnitude of the change in the simulation results with respect to changes in the input parameter values. Desirable code operation is referred to as "numerical consistency" and implies an extremely small numerical sensitivity.

Evaluation metrics

Assessing the performance of a numerical simulation requires the selection of appropriate metrics. Some difficulty occurs due to random number generation used in the ionization and collision subroutines. This particular difficulty means that simulations which are numerically consistent will tend to display a random but finite numerical sensitivity. Longer averaging intervals and/or ensemble averaging can reduce the effect of this randomness on the evaluation metrics. Choosing appropriate metrics is further complicated by the oscillatory nature of Hall thruster operation. Obviously, since the code simulates a thruster with oscillatory behavior, it should also produce oscillatory solutions. Fortunately, for typical simulations produced by

this code, time-averaged performance parameters and mean centerline values remain bounded.

In practice, the most relevant and accessible time-averaged performance parameters are thrust, specific impulse, and ion current. These are used extensively throughout this chapter to evaluate numerical sensitivity; however, other evaluation metrics are frequently used to demonstrate numerical sensitivity. These include profiles of mean centerline potential, mean centerline ionization rates, and mean electron energies. Many further evaluation metrics do exist but their use is limited in this chapter.

Device specific comparison

The numerical sensitivity of the code to the numerical modeling parameters is not the same for different thrusters and operating conditions. Therefore, it is not important that the simulations reflect a particular thruster operational condition. Indeed, if a particular validated simulation were being studied, due to the coupling between physical and numerical modeling choices, while exploring the numerical parameter space, it would be necessary, at almost each data point, to re-value the physical modeling coefficients in order to match the experimental data. Although some of the results presented in this section are clearly not optimal, the simulations do provide sufficiently representative results to demonstrate the numerical characteristics of the code.

Most of the results presented in this section are based on an SPT-70 thruster operated at 300 V with a Bohm mobility model. Additional results are based on an SPT-100 thruster operated at 300 V with a wall-collision mobility model and a NASA-173Mv1 thruster operated at 700 V on krypton with a mixed mobility model.

Since the results presented in this section are intended only to provide representative solutions, in order to simplify the data collection procedure, the energy loss coefficients for these models are not validated against experimental data.

3.2 Global timestep

The global timestep for the code is determined by the cell width (Δx) and the theoretical maximum speed of a perfectly accelerated ion as follows:

$$\Delta t = \alpha_t \Delta x \sqrt{\frac{m_i}{2qV_d}} \tag{3.1}$$

In this formulation, α_t is a safety factor (< 1) to account for the possibility of ion superacceleration (i.e., ion energies greater than V_d) and ion trajectories which do not cut directly across the maximum cell width.

A range of global timesteps is tested on an SPT-70 configuration. The starting point for this test is a single simulation run to a steady state solution (about 100,000 iterations with $\alpha_t = 1.00$). Each of the data points in Table 3.1 represents the average of two to four separate runs with different seeds in the random number generator.

Table 3.1: Time Averaged Data from SPT-70 Timestep Study (Elapsed Time $2.98 \cdot 10^{-3}$ s)

α_t	Timestep (s)	Thrust (mN)	I_{sp} (s)	Mass Flow Rate (mg/s)
1.00	$4.96 \cdot 10^{-8}$	38.3	1672	2.336
0.75	$3.72 \cdot 10^{-8}$	38.4	1675	2.336
0.50	$2.48 \cdot 10^{-8}$	38.6	1684	2.342
0.25	$1.24 \cdot 10^{-8}$	39.7	1731	2.343
0.125	$0.62 \cdot 10^{-8}$	39.8	1739	2.352

The results presented in Table 3.1 clearly demonstrate that the numerical sensitivity of the code for timesteps of $\alpha_t \leq 1.00$ is low ($< 4\%$ difference in thrust between

$\alpha_t = 1.00$ and $\alpha_t = 0.125$). It is also clear that the higher mass flow rates observed for smaller timesteps corresponds directly to higher thrust levels. In theory, if all the cases were run for an infinitely long period of time, then the time-averaged mass flow rates should approach the nominal mass flow rate (2.34 mg/s) and all the thrust data should coalesce. However, since the simulations of the smallest timestep took over two days to complete, in the interest of computational tractability, a reasonable safety factor of $\alpha_t = 0.50$ is assumed for all simulations presented in this thesis (unless otherwise indicated). More importantly, the time-averaged mass flow rate must fall within 0.5% of the nominal mass flow rate before a simulation is considered to be converged.

3.3 Physical grid refinement

Since a rectangular structured grid is used to mesh the computational domain, only certain grid spacing combinations can be used in this code. Smaller grid spacing leads to more accurate simulations and the ability to resolve smaller physical details in the simulation. The price of these benefits is the greater computational expense and time penalty for using more detailed grids.

The code is tested with two different grid resolutions, 79 cells axially x 64 cells radially (1 mm x 1 mm per cell) and 158 cells axially x 128 cells radially (0.5 mm x 0.5 mm per cell). The results are presented in Table 3.2. These results show that the difference in thrust and specific impulse are both $\sim 4\%$ while the difference in ion current is less than 1%.

A comparison of the mean centerline potential profiles of the two grid spacings is presented in Fig. 3.1. From this data, it is clear that the potential gradient remains centered on the same physical location for both grid spacings. The only deviation

Table 3.2: NASA-173Mv1 Mesh Spacing

Cell Size	Thrust (mN)	I_{sp} (s)	Ion Current (A)
1 mm x 1 mm	233.6	3284	8.096
0.5 mm x 0.5 mmm	243.7	3416	8.175

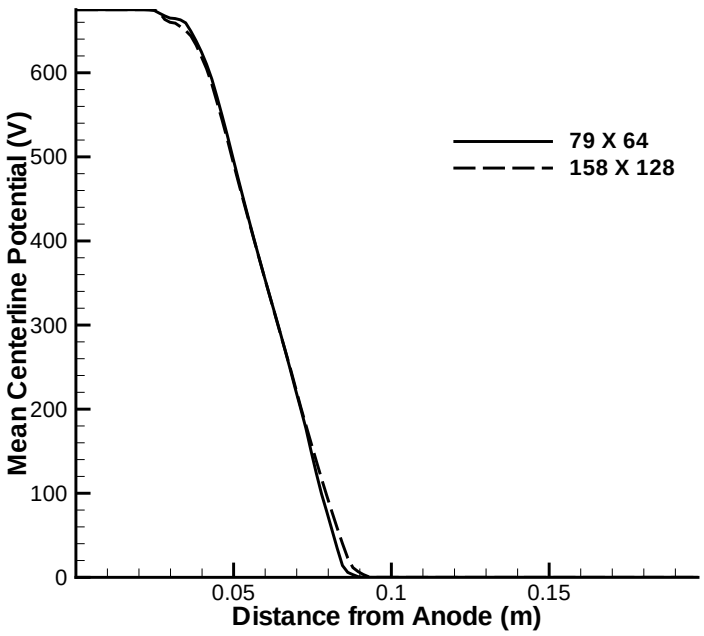


Figure 3.1: NASA-173Mv1 Mean Centerline Potential (Variable Mesh Spacing)

between these profiles is directly due to the resolution of the mesh spacing at the beginning and end of the potential gradient. Based on these results, grid spacings of around 1 mm x 1 mm are used for other thruster configurations.

3.4 Magnetic field grid

Since induced magnetic fields in Hall thrusters are small in comparison to the static magnetic field (see Sec. 2.2), no significant magnetic field dynamics are expected in the simulation. Consequently, only a single static magnetic field configuration is necessary for a thruster simulation. As shown in Fig. 3.2, the magnetic field is used

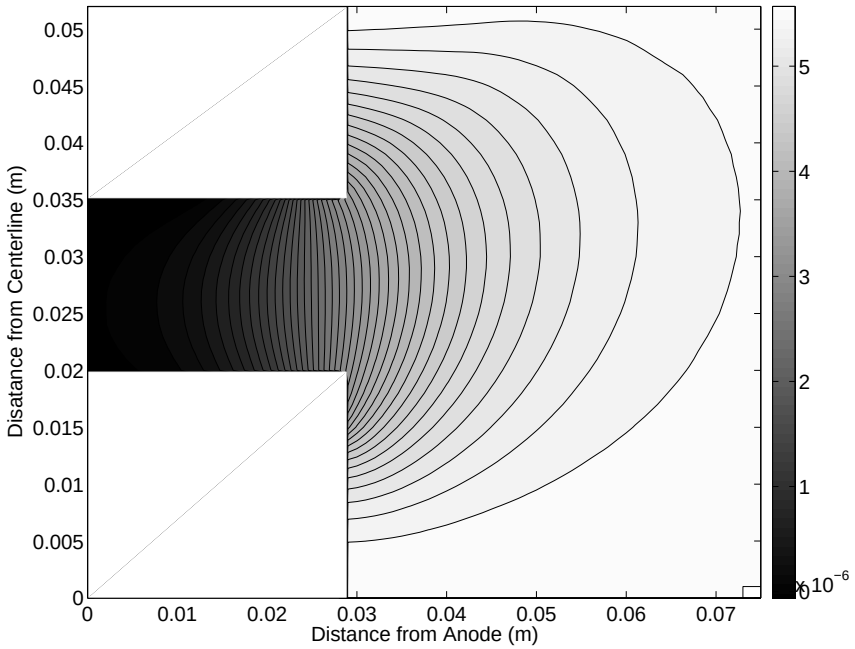


Figure 3.2: SPT-70 Magnetic Field Streamfunction

to generate magnetic field lines by tracing equipotentials of the magnetic streamfunction. This leads directly to a 1-D discretization of the domain. Since electrons are assumed isothermal along magnetic field lines, this 1-D discretization is a natural discretization for the electron energy equation. Likewise, since the thermalized potential is assumed constant along field lines, this 1-D discretization is also a natural discretization for the electrostatic potential.

The SPT-70 magnetic field was provided by *Fife* (2004). The SPT-100 magnetic field was generated using a combination of experimental data and computational methods. Experimental radial magnetic field measurements along the inner and outer acceleration channel walls were provided from experimental sources. The remaining radial magnetic field (on surfaces perpendicular to $\hat{n}$) and axial magnetic field (on surfaces perpendicular to $\hat{r}$) boundary conditions were estimated. Since

the induced magnetic field in the thruster is assumed to be small ($\nabla \times B \approx 0$), the interior magnetic field of the thruster is then calculated by matrix inversion of $\nabla^2 B = 0$. The UM/AFRL P5 magnetic field was measured experimentally using a Hall probe. Finally, the NASA-173Mv1 magnetic field is generated computationally using MagNet 6.0, a commercial software package. Since efficient operation of Hall thrusters typically requires that the magnetic field configuration be varied to minimize the discharge current, the magnetic field grid geometry also changes at different thruster operating conditions.

Overview

The locations of the virtual cathode line (λ_c) and virtual anode line (λ_a) define the physical domain over which the electron energy and electrostatic potential are solved actively. (This region will henceforth be referred to as the "active domain".) Upstream of λ_a and downstream of λ_c, the boundary values for the electron energy and electrostatic potential are extended to the anode and exit plane, respectively. Presented in Fig. 3.3 is a schematic showing the location of λ_a and λ_c on the lambda grid.

Due to constraints in the code, the locations of λ_c and λ_a must be existing magnetic field lines. In addition, boundary values for the electron energy and electrostatic potential must be applied at both λ_c and λ_a. These boundary conditions can be either Dirichlet or Neumann conditions (but not both Neumann boundary conditions). Typically, a Dirichlet boundary condition is used at λ_c and a Neumann or Dirichlet boundary condition is used at λ_a.

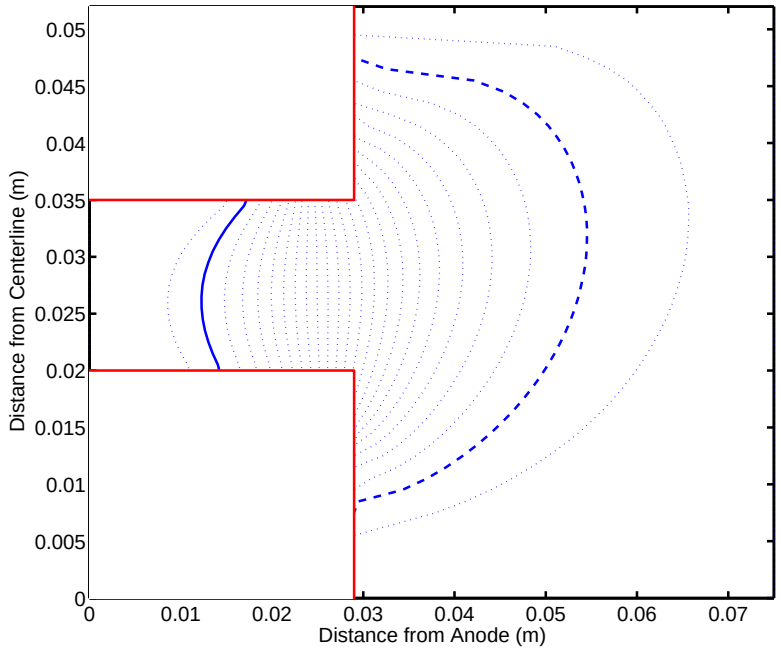


Figure 3.3: SPT-70 Lambda Grid Schematic(λ_a solid, λ_c dashed)

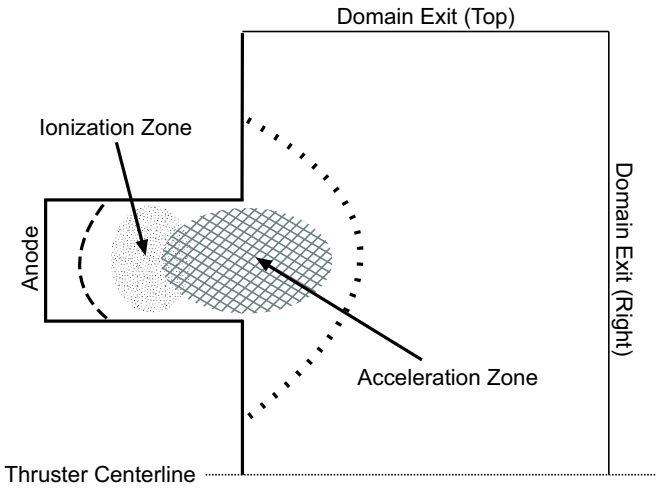


Figure 3.4: Ideal λ_a and λ_c configuration (λ_a dashed, λ_c dotted)

Ideal λ_a and λ_c configuration

A thruster schematic showing the optimum placement of λ_a and λ_c is shown in Fig. 3.4. Ideally, λ_a is located well upstream of the ionization zone. Otherwise, the ionization rate will be fixed by the $\varepsilon(\lambda_a)$ boundary condition and since the electron energy upstream of λ_a is not dynamically updated (since it is outside the active domain), significant ionization will be neglected and thruster performance will be artificially supressed.

Choosing $\lambda_a = 1$ (the anode face) would greatly simplify the process of locating λ_a by consistently offering a thruster-independent choice for λ_a; however, two primary concerns preclude this choice. First, for numerical reasons, the present version of the code is unstable due to excessive ionization in the vicinity of the anode injection site. Although there are ways to deal with this problem, there is a more significant physical reason not to locate λ_a at the anode face. This reason is related to questions regarding the physical applicability of the 1-D electron energy equation and 1-D potential solver to the anode region. In particular, the anode region is dominated by an electron diffusion transport process and lacks a significant radial magnetic field, thus leading to the breakdown of the physical assumptions underlying the use of the thermalized potential to formulate the 1-D potential and electron energy models.

In practice, the ionization zone and acceleration zone are considerably less well spatially defined than as shown in Fig. 3.4. In addition, the electron energy model and mobility model also play crucial roles in the ionization and acceleration processes, thereby influencing the location of the ionization zone and acceleration zone. As a result of these considerations, in order to establish the optimum locations for λ_a and λ_c in a thruster simulation, it is necessary to test a range of λ_a and λ_c locations.

For some simulations, it may be possible to establish an "ideal" λ_a location to

minimize the numerical sensitivity of the code; however, for other simulations, the ionization region is sufficiently diffuse as to preclude the possibility of finding an "ideal" λ_a location. Obviously, it is desirable to be able to establish that λ_a is situated in an optimum location upstream of the ionization zone; nevertheless, in the absence of such an "ideal" λ_a region, the code can still serve as a useful tool as long as sufficient care is taken to understand the impact of the λ_a location on the results.

Experimental measurements can establish the location of an effective cathode plane at the local plasma potential minimum in the near-field of the thruster. Placing λ_c at this location is the ideal configuration. If experimental data do not exist, then to ensure that the acceleration zone is not artificially compressed, the optimum placement of λ_c is well downstream of the acceleration zone.

3.4.1 Virtual anode line

In this section, simulation results are presented for a series of locations of λ_a for different Hall thrusters with various mobility models. The results presented in this section demonstrate the significant influence of λ_a on simulation performance and the difficulty in establishing an optimum λ_a.

SPT-70

An SPT-70 thruster simulation using a Bohm mobility model is tested with boundary conditions of $\varepsilon(\lambda_a) = 5\ eV$, $\lambda_c = 3$, and $\varepsilon(\lambda_c) = 2\ eV$. The different λ_a locations shown in Fig. 3.5 generate the results presented in Table 3.3. *Note: Ionization is not considered upstream of λ_a in this simulation.*

The mean centerline electron energies for the SPT-70 corresponding to these four λ_a locations are presented in Fig. 3.6. With an electron energy $> 10\ eV$ and a

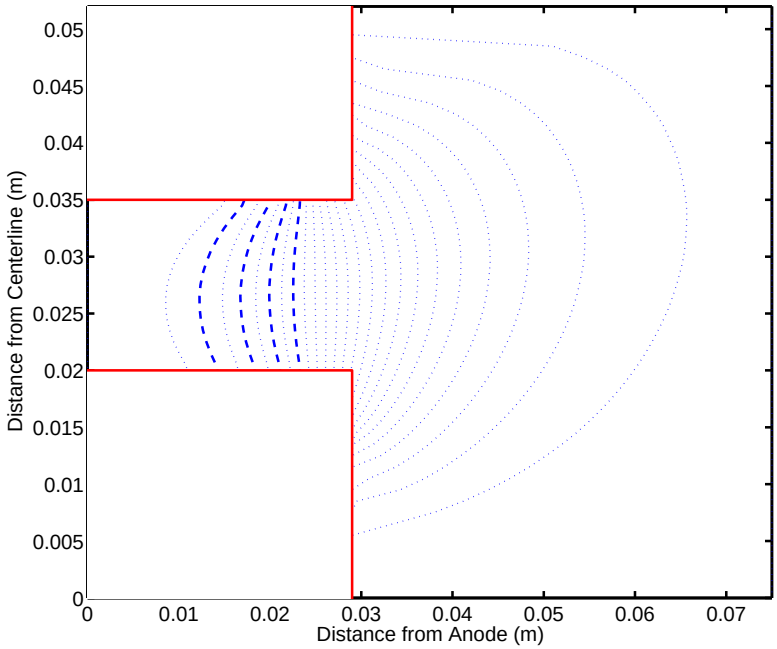


Figure 3.5: SPT-70 Virtual Anode Lines (Dashed Lines - from left, $\lambda_a = 3, 5, 7, 9$)

Table 3.3: SPT-70 Virtual Anode Line Study

λ_a	Exit Thrust (mN)	I_{sp} (s)	Ion Current (A)
3	39.6	1729	1.63
5	37.1	1655	1.56
7	35.5	1620	1.50
9	31.6	1505	1.34

significant ($> 1 \cdot 10^{19} \frac{\#}{m^3}$) population of neutrals in most of the acceleration channel, significant ionization is expected in this region.

The mean centerline potentials for the SPT-70 are presented in Fig. 3.7. From these data, it is clear that the mean centerline potential has only a weak dependence on the λ_a location. Since the acceleration zone is expected to be near the thruster exit, the numerical sensitivity of the potential gradient to reasonable choices of λ_a (i.e. close to the anode) is very low.

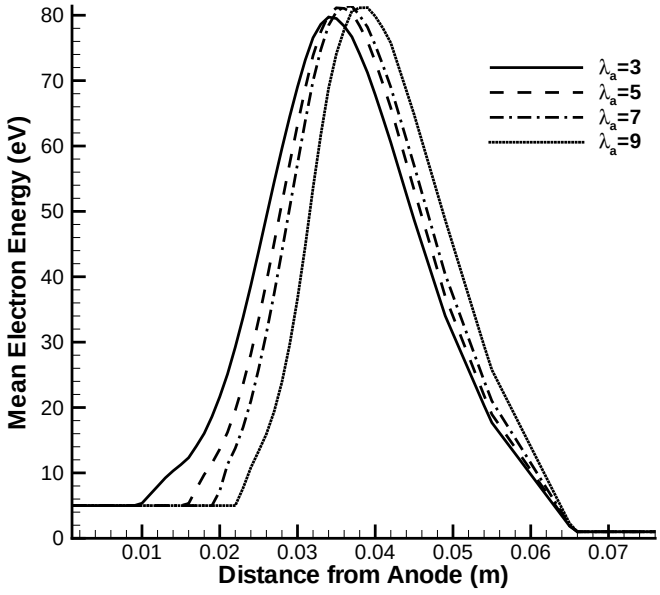


Figure 3.6: SPT-70 Mean Centerline Electron Energy

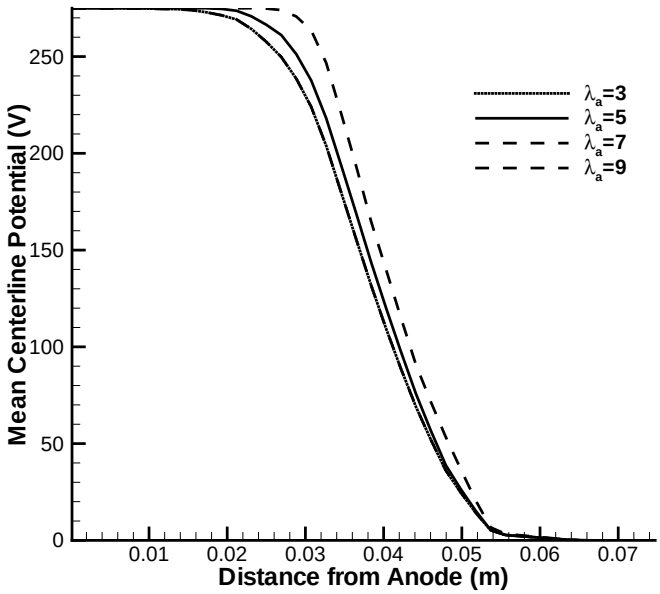


Figure 3.7: SPT-70 Mean Centerline Potential ($\lambda_a = 3$ and $\lambda_a = 7$ are nearly colinear)

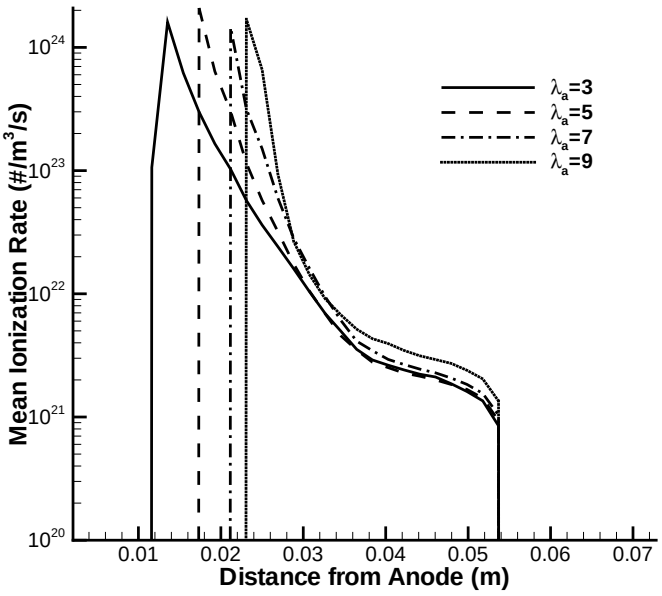


Figure 3.8: SPT-70 Mean Centerline Source Rate

The mean centerline source rates for the SPT-70 are presented in Fig. 3.8. It is clear that the λ_a location has a strong influence on the size of the ionization zone. Because the electron energy rises so sharply downstream of λ_a, choosing λ_a close to the anode results in a larger ionization zone than a choice of λ_a closer to the thruster exit.

SPT-100

An SPT-100 simulation using a wall-collision mobility model is tested with boundary conditions of $\varepsilon(\lambda_a) = 3\ eV$, $\lambda_c = 3$, $\varepsilon(\lambda_c) = 2\ eV$. The different λ_a locations shown in Fig. 3.9 generate the results presented in Table 3.4.

The mean centerline electron energies for the SPT-100 are presented in Fig. 3.10. Unlike the SPT-70, the mean centerline electron energy in the acceleration channel is lower in some of the configurations tested. For these configurations ($\lambda_a = 6$ and

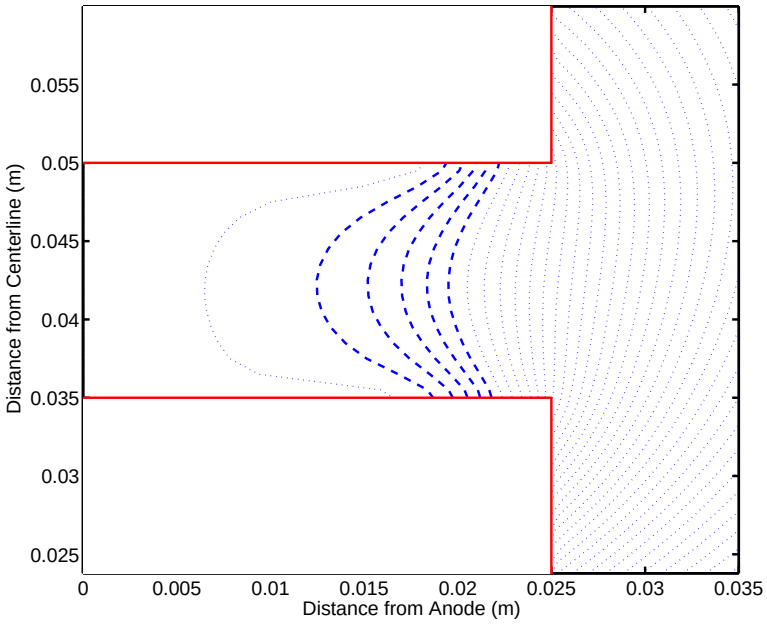


Figure 3.9: SPT-100 Virtual Anode Lines (Dashed Lines - from left, $\lambda_a = 3, 4, 5, 6, 7$)

Table 3.4: SPT-100 Virtual Anode Line Study

λ_a	Exit Thrust (mN)	I_{sp} (s)	Ion Current (A)
3	69.9	1425	3.48
4	66.2	1354	3.41
5	55.8	1147	3.41
6	31.0	634	1.57
7	24.9	509	1.16

$\lambda_a = 7$), the much lower peak electron energies results in very sharp reduction in simulation performance. The $\lambda_a = 3$, $\lambda_a = 4$ and $\lambda_a = 5$ lines all have a mean centerline electron energy of $< 10\ eV$ to within $\sim 16\ mm$ of the anode, implying that significant ionization does not occur in this region.

The mean centerline source rates are presented in Fig. 3.11. From these data it is clear that the choices of $\lambda_a = 5$, $\lambda_a = 6$ and $\lambda_a = 7$ intrude into the main ionization zone. $\lambda_a = 3$ and $\lambda_a = 4$ show some differences between 2 mm and 15 mm of the

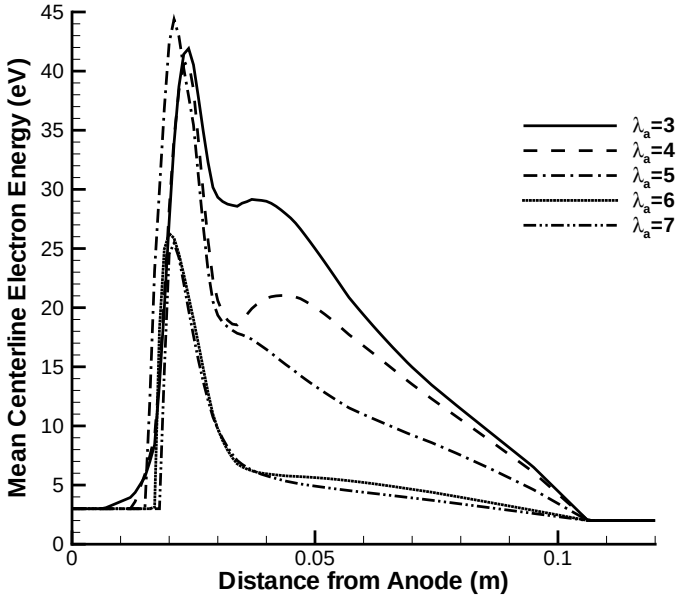


Figure 3.10: SPT-100 Mean Centerline Electron Energy

anode but both capture the main ionization peak at approximately 20 mm from the anode.

Analysis

For the Bohm mobility model configuration presented in this section, it is not possible to find an ideal λ_a location which completely encompasses the ionization zone. The principal difficulty in establishing an ideal λ_a resides in an inability to establish a clear upstream bound of the ionization zone.

For the wall-collision mobility model configuration presented in this section, it is sometimes possible to chose an optimum λ_a location (usually $\lambda_a = 3$ or $\lambda_a = 4$) which encompasses most of the ionization zone. This is due to the relatively well-defined and compact ionization zone predicted by the simulation of this particular thruster magnetic field geometry with a wall-collision mobility model.

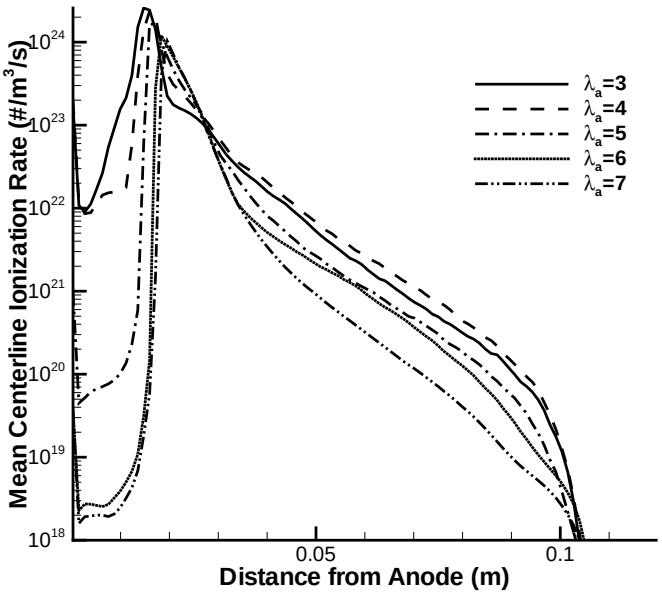


Figure 3.11: SPT-100 Mean Centerline Source Rate

In general, the existence of an ideal λ_a location requires that a particular thruster simulation produce a well-defined ionization zone which does not extend all the way to the anode. These characteristics of the ionization zone are strongly dependent on the mobility model used in the simulation and the raw thruster magnetic field geometry. In practice, placing λ_a at approximately 1 cm away from the anode face and using a low enough $\lambda_a(\varepsilon)$ usually ensures that anode ionization does not dominate the overall ionization process inside the acceleration channel and is sufficiently far upstream of the peak ionization zone to actively simulate most of the critical ionization dynamics.

3.4.2 Virtual cathode line

In this section, results are presented for various locations of λ_c for two different Hall thruster simulations with various mobility models. The results presented in this section demonstrate the significant influence of λ_c on simulation performance and

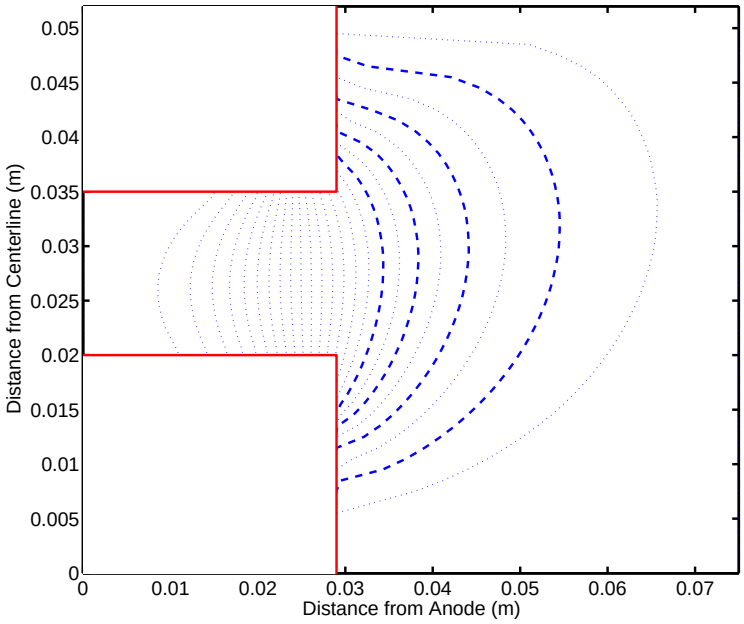


Figure 3.12: SPT-70 Virtual Cathode Lines (Dashed Lines - from right, $\lambda_a = 3, 5, 7, 9$)

the variation of this influence on different thrusters and mobility models.

SPT-70

An SPT-70 thruster simulation using a Bohm mobility model is tested with boundary conditions of $\varepsilon(\lambda_c) = 1\ eV$, $\lambda_a = 3$, and $\varepsilon(\lambda_a) = 5\ eV$. The different λ_a locations shown in Fig. 3.12 generate the results presented in Table 3.5. The mean centerline potentials for the SPT-70 are presented in Fig. 3.13.

Table 3.5: SPT-70 Virtual Cathode Line Study

λ_c	Exit Thrust (mN)	I_{sp} (s)	Ion Current (A)
3	39.6	1729	1.63
5	43.4	1873	1.74
7	46.0	1968	1.76
9	46.5	2004	1.74

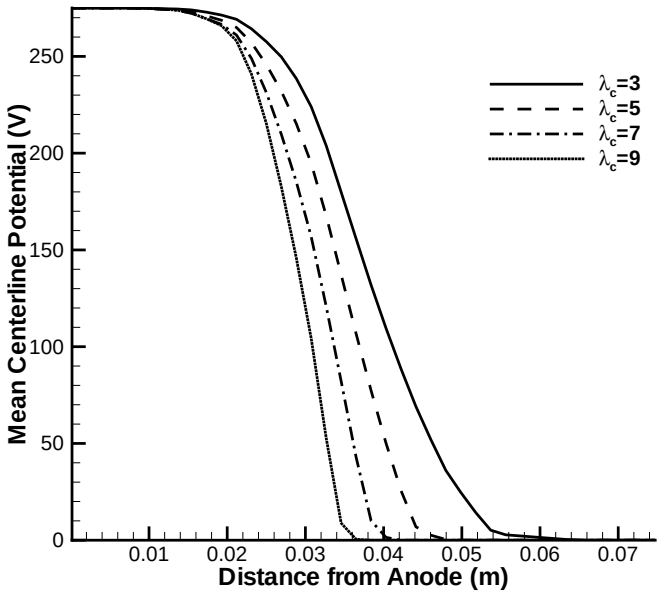


Figure 3.13: SPT-70 Mean Centerline Potential

SPT-100

An SPT-100 simulation using a wall-collision mobility model is tested with boundary conditions of $\varepsilon(\lambda_c) = 2\ eV$, $\lambda_a = 3$, $\varepsilon(\lambda_a) = 3\ eV$. The different λ_c locations shown in Fig. 3.14 generate the results presented in Table 3.6. The mean centerline potentials for the SPT-100 are presented in Fig. 3.15.

Table 3.6: SPT-100 Virtual Cathode Line Study

λ_c	Exit Thrust (mN)	I_{sp} (s)	Ion Current (A)
3	68.9	1420	3.47
5	70.0	1464	3.44
11	72.1	1511	3.44

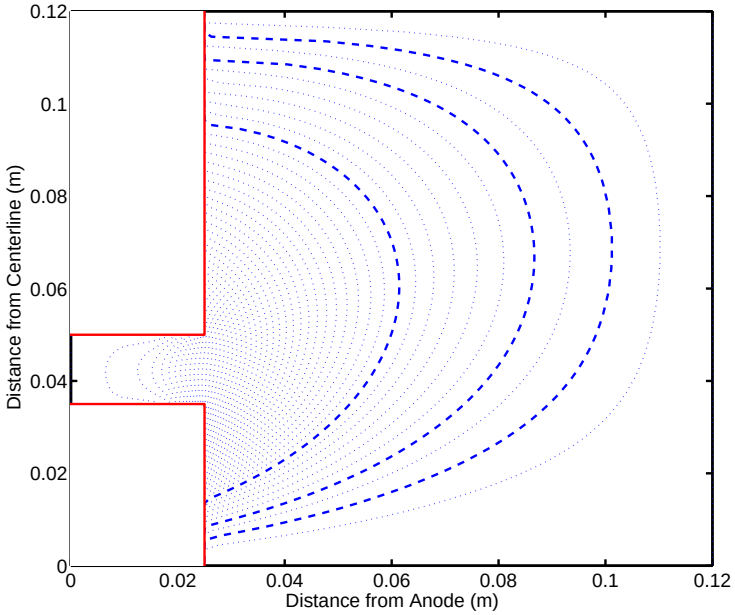


Figure 3.14: SPT-100 Virtual Cathode Lines (Dashed Lines - from right, $\lambda_a = 3, 5, 11$)

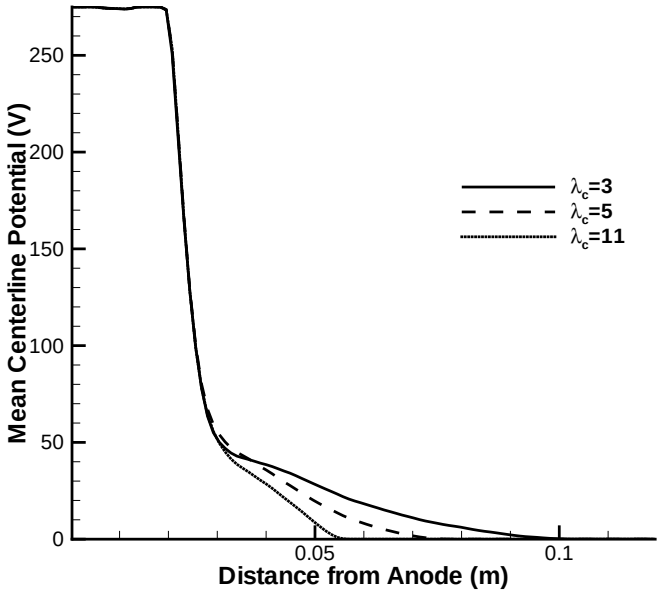


Figure 3.15: SPT-100 Mean Centerline Potential

Analysis

From these data, it is clear that moving λ_c towards the domain exit results in decreased thrust. It is also demonstrated that the numerical sensitivity of the simulation performance to λ_c is less than the numerical sensitivity to λ_a. The reason for this reduced sensitivity is that the ionization process upstream of the main potential gradient has greater impact on thruster performance than the ionization process downstream of the main potential gradient. Again, the SPT-70 shows a greater numerical sensitivity than the SPT-100 to the λ_c location.

The enhanced thruster performance (for both thrusters) due to a λ_c location closer to the thruster exit can be directly related to the increased potential gradient associated with this choice. In essence, by compressing the actively solved region, the potential solver must apply the same imposed potential drop over a smaller distance. This means that the bulk of the ion acceleration is completed closer to the thruster exit where the magnetic field curvature is less. As a consequence, ions which are fully accelerated close to the thruster exit show less plume divergence than ions which are not fully accelerated until further downstream from the thruster exit. (Note: The ion current remains largely independent of λ_c, indicating that the ionization zone is not being affected by the λ_c location.)

Since the λ_c location is used to define the active domain, the thermalized potential should be physically applicable in the region upstream of λ_c. In general, this precludes the arbitrary choice of the domain exit as the λ_c location in the simulation. Since the cathode flow is not effectively included in this model, the location of λ_c is not expected to duplicate exact physical conditions. (A 25 V reduction in the magnitude of the discharge voltage is used to correct for the fact that the cathode is actually below the plasma potential in the far field of the thruster.) Furthermore,

as will be demonstrated in Sec. 5.1.1.1, the electron current at λ_c must remain positive to ensure that the model assumptions remain physically consistent. In practice, choosing the correct λ_c location is an exercise in estimating the expected spatial extent of the main potential gradient (unless experimental data is available, in which case λ_c can simply be located at the effective cathode plane). Fortunately, sensitivity of the thruster performance to the λ_c location is not as high as when choosing the λ_a location, so even a non-optimal location of λ_c typically results in reasonable thruster performance.

3.4.3 Magnetic field grid refinement

The magnetic field grid is based on the spacing of the magnetic field lines from the initial thruster configuration. To generate these field lines, equipotentials of the magnetic streamfunction are calculated. Since the streamfunction is a continuous function between the anode and domain exit, an infinite number of lambda cells can be generated if the equipotentials evaluated are infinitely close together. In practice, however, the minimum grid spacing between the magnetic field grid lines near the exit of the acceleration channel cannot be significantly smaller than the physical grid spacing without requiring a smaller global timestep.

A series of simulations are performed with various magnetic field grid resolutions. Representative plots of the highest and lowest grid resolutions are shown in Fig. 3.16 and Fig. 3.17.

The results presented in Table 3.7 clearly demonstrate that for the entire range of $12 < \lambda < 23$, the integrated performance parameters remain relatively stable. As expected, the numerical sensitivity of the thrust is lower for finer magnetic field grids.

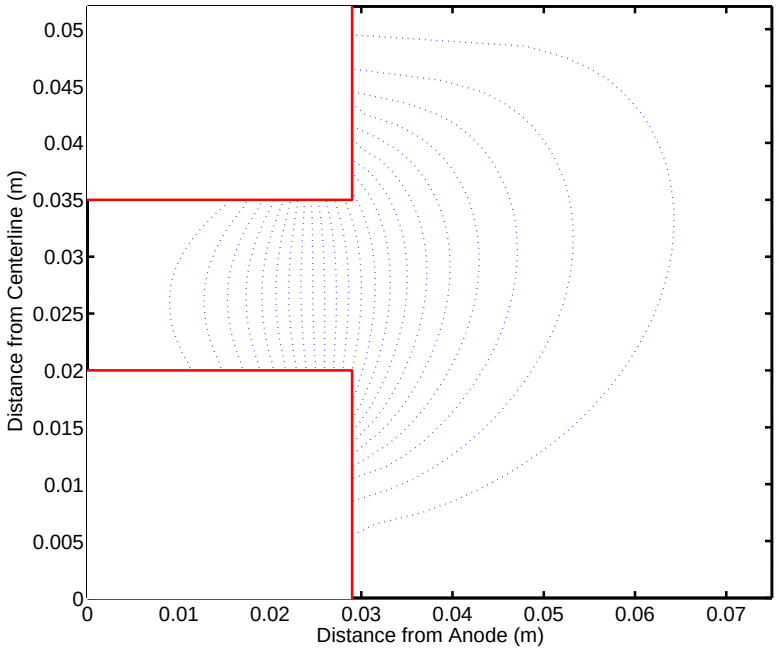


Figure 3.16: SPT-70 Lambda Grid ($\lambda = 23$)

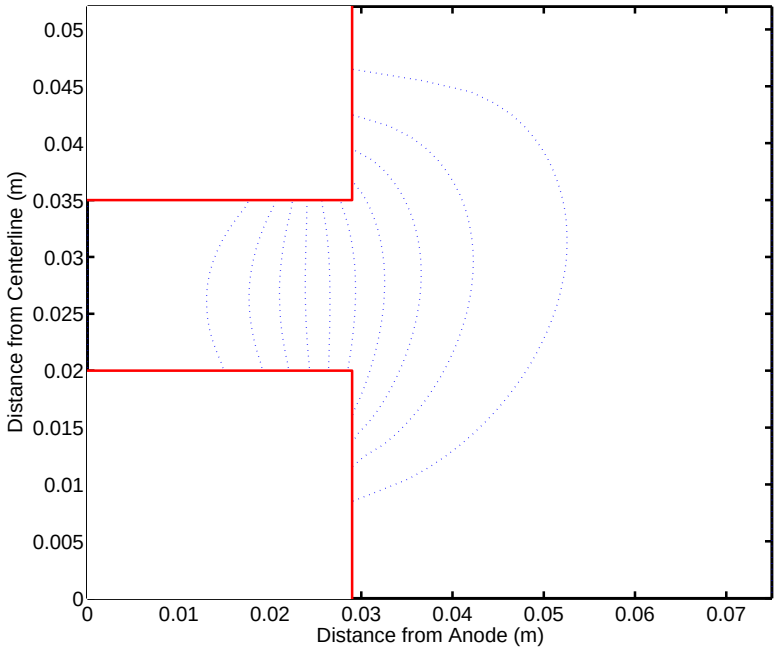


Figure 3.17: SPT-70 Lambda Grid ($\lambda = 12$)

Table 3.7: SPT-70 Lambda Grid Refinement Study

λ	Thrust (mN)	I_{sp} (s)	Ion Current (A)
23	37.93	1677	1.705
21	38.64	1701	1.715
19	36.17	1599	1.694
17	39.43	1723	1.730
15	38.65	1697	1.715
14	41.24	1824	1.710
13	40.90	1808	1.710

The mean electron energy profiles of these simulations are provided in Fig. 3.18. Small differences exist between the mean electron energy profiles at different lambda grid resolutions. The values of peak mean electron energy and the location of the peak mean electron energy remain virtually unchanged for different grid resolutions. Fortunately, the ionization region (roughly considered to begin when $\varepsilon > 10$ eV) begins at about the same location ($\sim$15 mm from the anode) for all the magnetic field grid resolutions. The greatest variation between the mean electron energy profiles is in the near-field of the thruster. Since the main ionization zone and steepest potential gradient are near the thruster exit, the discrepancies in the mean electron energy profiles in the near-field of the thruster have a relatively small impact on the thruster performance. Based on these results, the typical magnetic field grid resolution is chosen to ensure that the minimum magnetic field grid spacing is between 75% to 125% of the physical grid spacing.

3.5 Electron energy studies

3.5.1 Subcycling frequency

The explict electron energy formulation derived in Sec. 2.6 is updated at a subcycling frequency which is an integer divison of the global timestep. Since the electrons are more than 80,000 times lighter than the heavy particles, they experience much

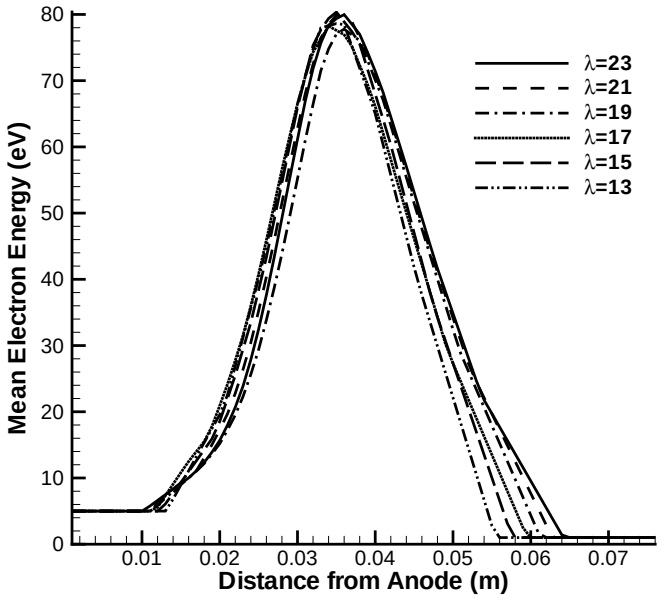


Figure 3.18: SPT-70 Mean Electron Energy

faster dynamics than the heavy particles. Thus, to capture the dynamical evolution of the electron energy, it is necessary to iterate the electron energy equation faster than the global ion timestep. The simulation results for various electron timesteps are presented in Table. 3.8 for the SPT-70.

Table 3.8: SPT-70 Electron Energy Subcycling Frequency Performance Results

Ion Timestep Divisor	Electron Timestep (s)	Thrust (mN)	Ion Current (A)
1000	$2.48 \cdot 10^{-11}$	37.95	1.71
500	$4.96 \cdot 10^{-11}$	37.90	1.71
200	$1.24 \cdot 10^{-10}$	36.71	1.66
150	$1.65 \cdot 10^{-10}$	36.91	1.66
100	$2.48 \cdot 10^{-10}$	37.95	1.71

As is clearly shown in Table. 3.8, for the range of divisors presented, the thrust performance and ion current has only small numerical sensitivity to the electron energy subcycling frequency. An electron subcycling frequency divisor of 200, suggested

by *Fife* (1998), is used in all subsequent simulations.

3.5.2 Weighting factor

The electron energy can, at times, be a rapidly varying quantity. As a consequence, it is desirable to introduce a relaxation factor to provide numerical stability to the electron energy equation. The relaxation factor α_{relax} is used as follows:

$$\epsilon_{corrected} = (1 - \alpha_{relax})\epsilon_{new} + \alpha_{relax}\epsilon_{old} \tag{3.2}$$

The goal in choosing the smoothing factor is to stabilize the code as much as possible without greatly affecting the numerical performance. Too large an α_{relax} can result in an artificial numerical lag in the evolution of the electron energy. Results for a series of smoothing factors are presented in Table 3.9.

Table 3.9: SPT-70 Electron Energy Weighting (Elapsed Time $1.239 \cdot 10^{-3}$ s)

α_{relax}	Thrust (mN)	I_{sp} (s)	Ion Current (A)
0.9	40.7	1738	1.78
0.7	40.1	1731	1.66
0.5	39.6	1729	1.63
0.3	38.9	1690	1.62
0.1	38.5	1673	1.61

Trends from Table 3.9 indicate that for a very broad range of α_{relax}, the performance of the simulation is only marginally affected. In the interest of numerical stability, $\alpha_{relax} = 0.5$ is used throughout the simulations presented in this thesis.

3.6 Macroparticle count

In any particle code, having a sufficient number of macroparticles in the simulation is critical to numerical accuracy. Although particle codes are very robust, working even when macroparticle counts are very low, since the error in the statistics

of a cell decreases as $\frac{1}{\sqrt{N}}$ (where N is the number of macroparticles in the cell), a large number of macroparticles per cell is desired to improve accuracy. Typical particle codes aim to balance computational tractability and accuracy by maintaining a particle count of 10-50 macroparticles per cell.

Control over the number of macroparticles in this code is different for charged and neutral species. Neutrals are injected at the anode and boundaries at a fixed rate (measured in macroparticles per global timestep). The actual number of macroparticles in the simulation is entirely dependent on these input conditions and the rate at which neutrals are removed due to ionization processes and created due to wall recombination processes. The number of macroparticles of each charged species is directly controlled by the collision multiplier in the MCC ionization algorithm (see Sec. 2.4.3). The desired numbers of ion macroparticles (both singly and doubly charged) are inputs to the code. Based on these macroparticle targets, the collision multiplier can be temporarily increased to attempt to match the target. This procedure does not guarantee that the ion target is matched exactly; however, it does consistently drive the macroparticle count towards the target number.

The purpose of this study is to identify a satisfactory ion macroparticle target by varying the target number of macroparticles and observing the resulting thrust and ion current to identify a region with very low numerical sensitivity to the macroparticle count. The results presented in Fig. 3.19 are referenced against the average macroparticle count per cell (based on 3,984 active grid cells).

From the data in Fig. 3.19, it is clear that if the target total ion macroparticle count is too small, then the performance of the thruster is artificially enhanced. The sensitivity of the simulation data is minimized at counts of over 30 macroparticles per cell (which roughly corresponds to a target macroparticle count of 125,000).

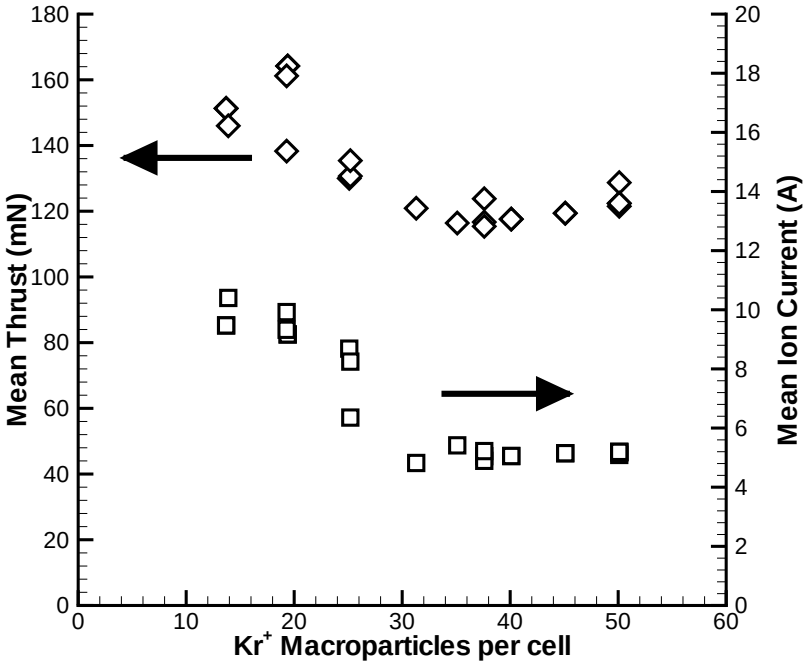


Figure 3.19: NASA-173Mv1 Macroparticle Count

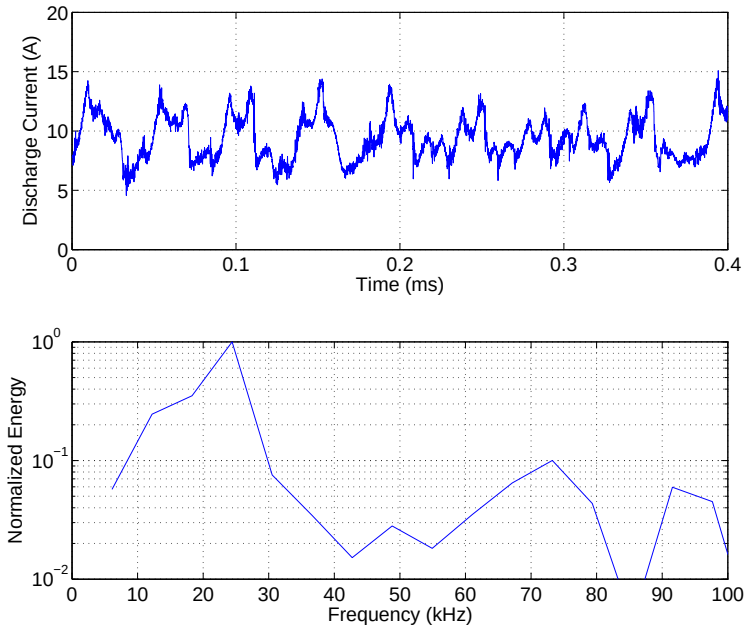


Figure 3.20: NASA-173Mv1 Experimental Discharge Current (*Upper – Discharge Current; Lower – Energy Spectrum*)

Adding more macroparticles to the simulation achieves virtually the same thruster performance at higher computational expense. For the duration of this thesis, a target ion macroparticle count of at least 30 macroparticles per cell is maintained.

3.6.1 Induced Oscillations

There are many different oscillatory processes in a Hall thruster plasma. Many of these oscillations can be seen in the trace of the discharge current. One type of axial oscillation in the 10-30 kHz range is referred to as the "breathing-mode" oscillation by *Boeuf and Garrigues* (1998). This type of oscillation, which occurs only at certain thruster operating conditions, is characterized by oscillation magnitudes of up to the order of the mean current and is typically the most dominant oscillation in the low frequency (less than 50 kHz) spectrum.

From an experimental discharge current trace for the NASA-173Mv1 shown in

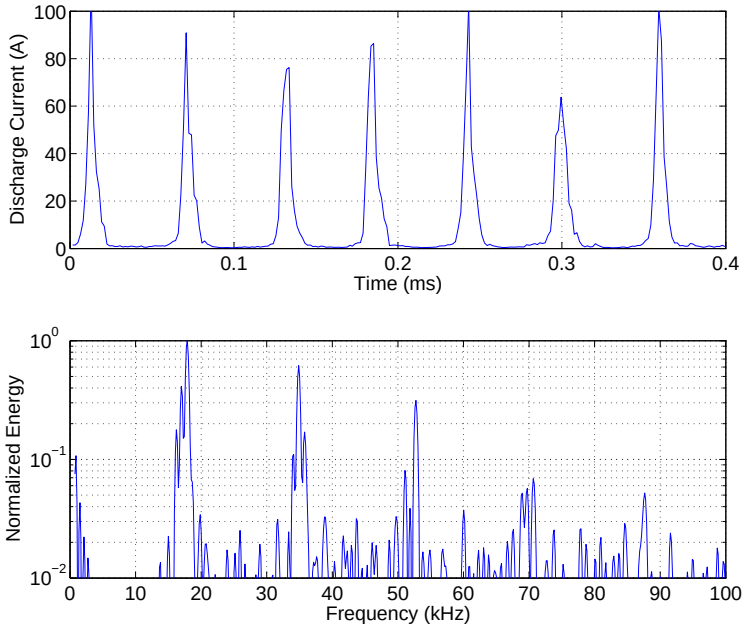


Figure 3.21: NASA-173Mv1 – 13 Kr^{+} macroparticles/cell, 11 Kr^{++} macroparticles/cell (*Upper – Discharge Current; Lower – Energy Spectrum*)

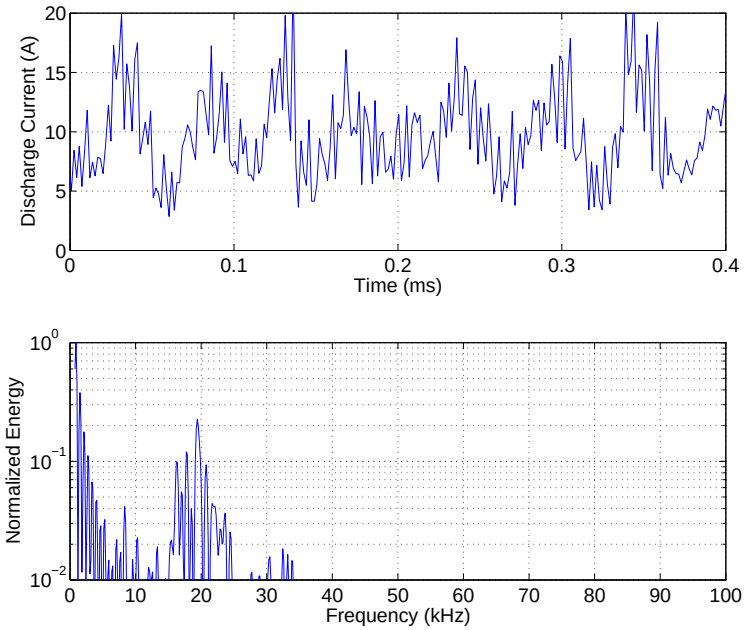


Figure 3.22: NASA-173Mv1 Discharge Current – Computational (*Note: Different λ_a and $\epsilon(\lambda_a)$ than other computational results presented in this section.*)

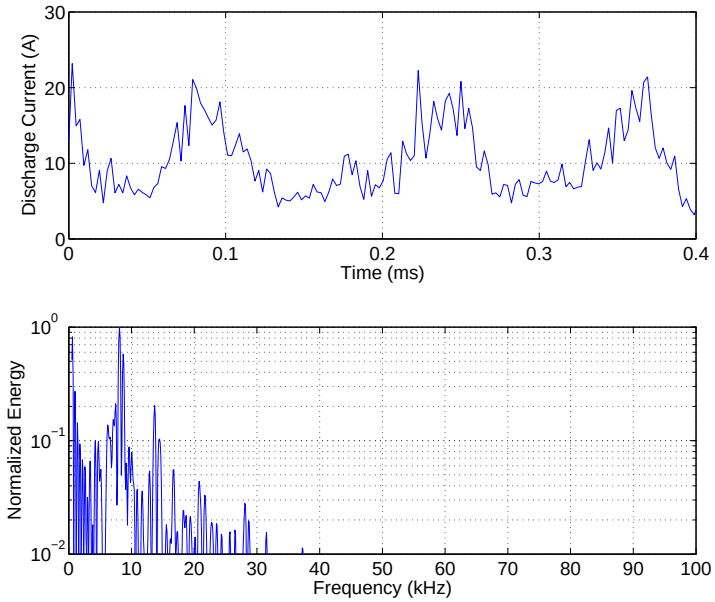


Figure 3.23: UM/AFRL P5 Discharge Current – Computational (300 V Nominal discharge voltage) (*Breath mode oscillation observed experimentally at 11 kHz for discharge voltage of 500 V*)

Fig. 3.20, a breathing mode oscillation clearly exists at a frequency of about 23 kHz. The simulation results provided in Fig. 3.21 present a very strong oscillatory behavior at 18 kHz. Although the magnitude of the oscillation in this particular simulation is about five times greater than that observed experimentally, realistic breathing mode oscillations can be seen in other computational simulations of the NASA-173Mv1 shown in Fig. 3.22 and of the UM/AFRL P5 as shown in Fig. 3.23 .

Evidence of the breathing mode oscillation in the simulation deteriorates as the number of macroparticles in the simulation is increased. In Fig. 3.24, as the macroparticle count is roughly doubled, the regular breathing mode oscillation begins to degrade and significant oscillations appear at 14 kHz and 30 kHz. Finally, as the macroparticle count is further increased in Fig. 3.25, evidence of any significant breathing mode oscillation is completely absent.

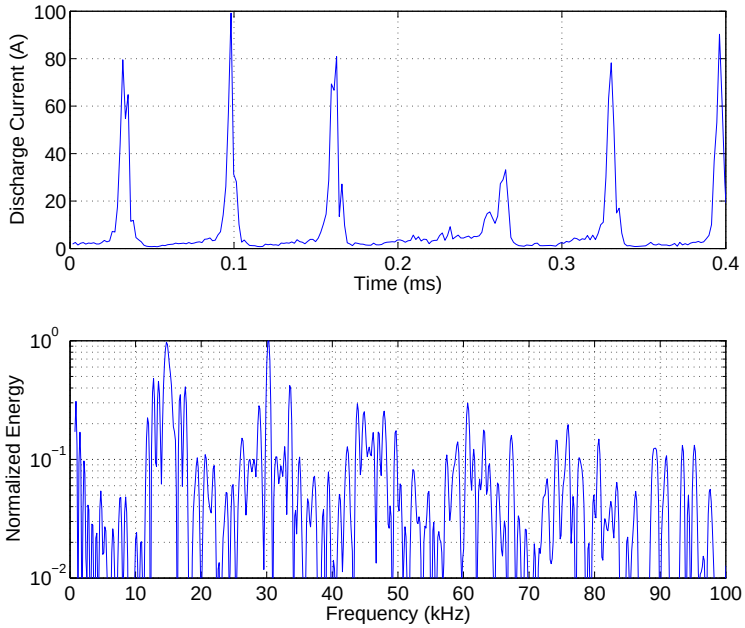


Figure 3.24: NASA-173Mv1 – 25 Kr^{+} macroparticles/cell, 22 Kr^{++} macroparticles/cell (*Upper – Discharge Current; Lower – Energy Spectrum*)

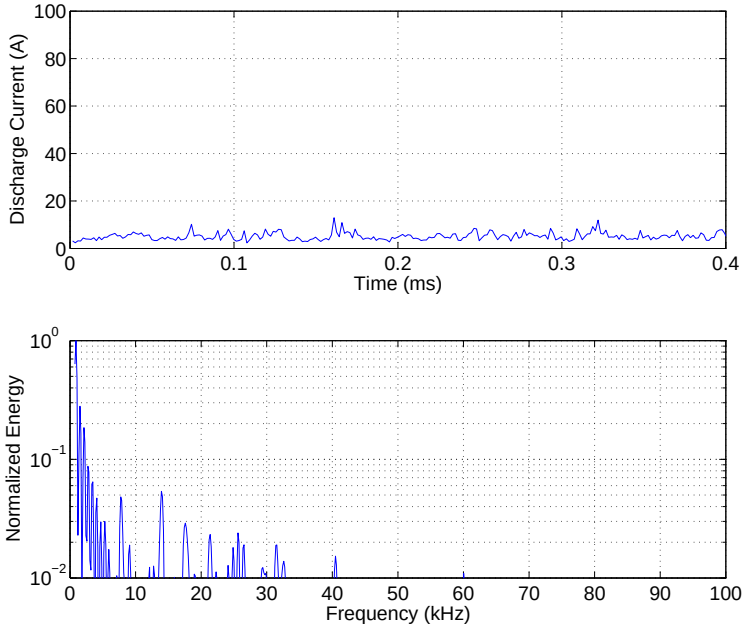


Figure 3.25: NASA-173Mv1 – 37 Kr^{+} macroparticles/cell, 33 Kr^{++} macroparticles/cell (*Upper – Discharge Current; Lower – Energy Spectrum*)

Since the experimental discharge current demonstrates the existence of a breathing mode oscillation at this thruster operating condition, the code should reproduce this behavior regardless of macroparticle count. Unfortunately, in this computer simulation, the presence of a breathing mode oscillation is dependent on the ion macroparticle count. This dependence on numerical parameters, rather than experimental parameters, leads to serious questions about why a high macroparticle count completely masks the breathing mode oscillations. The answer to this question lies in the mechanism by which ion macroparticles are generated.

In theory, the collision multiplier, γ, while increasing the number of ion macroparticles, should have no additional effect on the overall ion density since the presence of many smaller macroparticles or a few large macroparticles results in the same ionization statistics. In practice, for the low macroparticle count case shown in Fig. 3.21, the collision multiplier spikes very sharply during the course of a breathing mode oscillation, allowing the capture of relevant time dependent features. On the other hand, in the high macroparticle count case of Fig. 3.25, the number of macroparticles leaving the simulation during a breathing mode oscillation is relatively low compared to the total number particles in the domain, so the collision multiplier is not raised significantly. This consistently low collision multiplier results in such low collision probabilities that successful ionization events tend to occur very infrequently and, as a result, the creation of ion macroparticles is insufficient to resolve the breathing mode oscillation. In addition, this consistently low collision multiplier results in seemingly sporadic ionization events (producing very large macroparticles) which, because they are out of phase with the physical driven oscillations, actually dampen the breathing mode oscillation. A test problem illustrating this behavior is shown in Fig. 3.26.

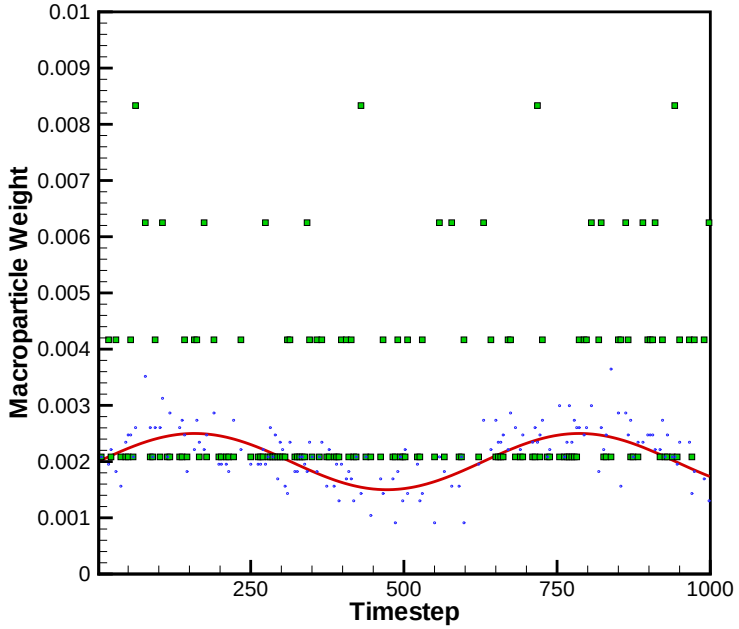


Figure 3.26: Collision Multiplier Effects (*Solid line – Test Collision Probability; Squares – Low Collision Multiplier* [$\gamma = 16$]*; Dots – High Collision Multiplier* [$\gamma = 256$]) This figure presents the output of the ionization algorithm with two different collision multipliers.

At a given timestep, the test collision probability indicates the total desired weight of ionized macroparticles. A source population of 30 equally weighted neutral macroparticles is provided at each timestep. The ionization algorithm uses the test collision probability to determine the actual number of ion macroparticles ionized at each timestep. The weight of the newly created ion macroparticles is summed at each timestep and presented above. After each timestep, the ion macroparticles are deleted and the neutral macroparticle population is reset to 30 macroparticles.

The results presented above demonstrate clearly that if the collision multiplier is too low, then the ionization algorithm does not create enough ion macroparticles to resolve the characteristic oscillation in the test collision probability. (In fact, spurious oscillation frequencies are actually induced by this mechanism.) A high collision multiplier allows the ionization algorithm to accurately reproduce the oscillatory features of the test collision probability.

It appears that the approach taken to ionization in this code (direct neutral macroparticle to ion macroparticle MCC ionization with a variable collision multiplier) has a direct influence on the physics modeled in the simulation. Unfortunately, for low collision multipliers, this influence results in the dampening of oscillatory behavior.

3.7 Conclusions

Based on the results presented in this section, it is clear that there is a significant coupling between some of the numerical parameters (location of λ_a, location of λ_c and desired macroparticle count) and the physical behavior demonstrated by the simulation; however, judicious choices for all the remaining numerical parameters, including the global timestep, physical and magnetic field grid spacing, electron energy subcycling frequency and electron energy relaxation factor, ensures that the simulation results are relatively insensitive to these numerical parameters, thus allowing the physical modeling effects to dominate.

To assign a finite estimate for the error due to specific numerical parameter choices requires a baseline simulation which is very nearly completely insensitive to numerical parameter choices (such as $\alpha_t \ll 1$ or $\Delta x \rightarrow 0$). Establishing such a baseline simulation for each numerical parameter choice is exceedingly difficult as such an analysis may potentially need to be repeated for multiple physical modeling configurations (as has been demonstrated in the analysis of the λ_a location for two different mobility models). Since the simulation sensitivity to physical modeling parameters for both the electron energy (Chapter IV) and the electron mobility (Chapter V) is extremely high, by establishing that the simulation sensitivity to most of the numerical parameter choices is small (generally ≤ 5 %) and by taking care to

understand the simulation sensitivity to the remaining numerical parameter choices, reasonable confidence can be gained that it is the physical modeling choices, not the numerical parameter choices, which are actually driving the simulation results.

CHAPTER IV

Physical Modeling Effects

The Hall thruster code developed for this thesis also requires many different physically based model parameters. The primary difference between these physically-based code parameters and the numerical parameters discussed in Chapter III is that perturbing physically-based code parameters should result in different simulation results while perturbing well-chosen numerical parameters should ideally result in identical simulation results. The physical parameters discussed in this chapter include the virtual anode line energy, the electron energy wall loss term and the electron energy collision loss terms.

4.1 Virtual Anode Line Energy

The virtual anode line, λ_a, represents the upstream boundary of the active simulation region in which the electrostatic field and the electron energy are solved self-consistently. Section 3.4.1 details the criteria governing where to locate λ_a in the simulation to ensure that physical effects are most effectively captured. This section deals with the electron energy boundary condition at λ_a. This boundary condition is critical because, in theory, λ_a should be located just upstream of the main ionization zone. Since the electron energy boundary condition effectively establishes the ion-

ization rate and local plasma density at λ_a, a well-chosen electron energy boundary condition must provide a smooth transition from the constant plasma properties in the anode region upstream of λ_a to the active simulation region downstream of λ_a.

Experimental measurements of the electron temperature in this location are complicated by the difficulties in obtaining reliable data in this region of the thruster. In particular, if probe-based diagnostics are considered, then entry from the downstream end of the acceleration channel risks disturbing the main plasma body in the Hall current region. Furthermore, physical access to this region is limited by probe dimensions and experimental alignment requirements. As a result, data collected by *Haas* (2001) for the UM/AFRL P5 thruster operating on xenon includes electron temperature information only to within 10 mm of the anode. The electron energies at the furthest upstream location range from 3-7 eV. Data presented by *Bishaev and Kim* (1978) provides the electron temperature all the way to the anode for an SPT-100 Hall thruster operating on xenon. The electron energies in the vicinity of the anode in that study are around 6 eV.

A series of simulations are conducted on the SPT-70 thruster using a Bohm mobility model to determine the impact of the $\lambda_a = 3$ energy boundary condition on the performance of the thruster simulation. A range of anode energies, $\varepsilon(\lambda_a)$, are applied as boundary conditions at $\lambda_a = 3$ and the results are presented in Table 4.1.

Table 4.1: SPT-70 Virtual Anode Line energy

$\varepsilon(eV)$	Exit Thrust (mN)	I_{sp} (s)	Ion Current (A)
1	32.2	1529	1.36
3	35.8	1644	1.50
5	39.6	1729	1.63
7	40.6	1747	1.66

Table 4.1 reveals the extreme sensitivity of the computed thruster performance

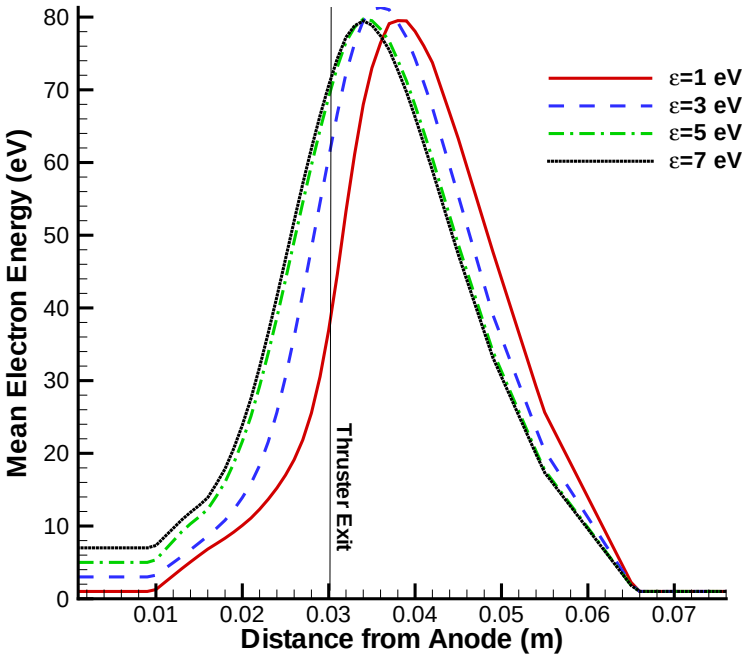


Figure 4.1: SPT-70 Mean Electron energy

on the anode electron energy. The profiles of the mean electron energy for the simulations listed in Table 4.1 are presented in Fig. 4.1. These results clearly demonstrate that raising the electron energy at λ_a shifts the mean electron energy curve upstream. Physically, this has the effect of moving the plasma density profile upstream by the same amount, effectively shifting the ionization zone deeper into the acceleration channel.

The effect of the $\varepsilon(\lambda_a)$ condition is very pronounced in this simulation due to the extended ionization zone characteristic of Bohm mobility models. As discussed in Sec. 3.4.1, in this case it is not possible to locate λ_a in a region which is clearly outside the acceleration zone, so the $\varepsilon(\lambda_a)$ condition simply determines how "far" λ_a is in the ionization zone. A high value of $\varepsilon(\lambda_a)$ implies that λ_a is deeper in the

ionization zone while a very low value of $\varepsilon(\lambda_a)$ implies that λ_a impinges only slightly into the acceleration zone.

As described in Sec. 3.4.1, the need to offset λ_a from the high neutral density at the anode forces a location about 1 cm downstream from the anode face. Depending on the mobility model chosen for the simulation, the choice of $\varepsilon(\lambda_a)$ can be highly sensitive (for a Bohm type mobility model) or not as sensitive (for a wall-collision mobility model). In any case, experimental measurements suggest an anode electron energy of 3-6 eV, and since λ_a represents the downstream border of this region, a $\varepsilon(\lambda_a)$ choice of 3-5 eV is generally an acceptable modeling compromise.

The simulation shows virtually no dependence on the $\varepsilon(\lambda_c)$ boundary condition for reasonable electron energy boundary conditions at the cathode ($\varepsilon(\lambda_c) \leq 5eV$). In practice, $\varepsilon(\lambda_c)$ is usually set to 2 eV.

4.2 Electron-Wall Energy Losses

As detailed in Sec. 2.6.3, the electron energy loss rate can be broken into a function of three primary loss mechanisms. The last of these mechanisms, the electron-wall energy loss frequency (the rate is obtained by multiplying by the plasma density), represents the energy lost by electrons through collisions with the acceleration channel walls. The form of this term, shown below, includes two coefficients: α, which corresponds to the frequency of electron encounters with the wall sheath, and U_{loss}, which represents the sheath energy. This term behaves in a monotonic fashion, acting to apply a larger energy loss to higher energy electron populations.

$$\nu(\varepsilon)_{walls} = \alpha \cdot 10^7 \exp\left(\frac{-U_{loss}}{\varepsilon}\right) \tag{4.1}$$

A series of simulations are conducted on the UM/AFRL P5 Hall thruster with a mobility curve fitted to the semi-empirical mobility. (This mobility curve is an

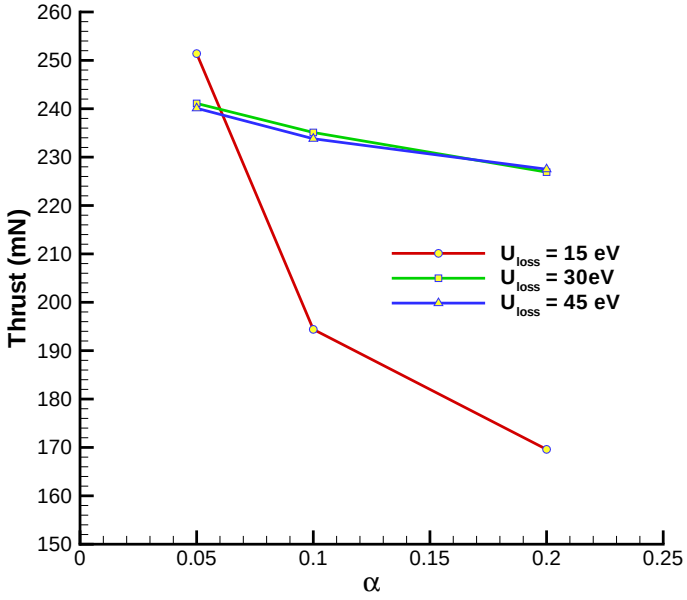


Figure 4.2: UM/AFRL P5 Energy Loss Coefficient

unoptimized version of the best fit curve presented in Sec. 5.1.2.4.) The results are shown in Fig. 4.2.

As the results make clear, the gross effect of increasing the electron-wall energy loss frequency by increasing α is to diminish thruster performance by lowering the mean energy, ε, and thus lowering the ionization rate. The dependence on U_{loss} is not as clear. In theory, increasing U_{loss} should result in a higher electron temperature, greater ionization, and higher thrust. In practice, the effect of changing U_{loss} does not always exhibit such clear trends. In Fig. 4.2, for relatively small variation in electron-wall energy losses (by varying α) there is a clear system response as expected correlating higher electron-wall energy losses with decreased thrust performance. Since the exponential term involves much larger changes in the energy range observed in the simulation (0-60 eV), the wall-loss terms frequently become so small that collisional energy loss terms dominate.

The overall trends in the density-averaged electron energy profiles do confirm the expected trends that either raising α (Fig. 4.3) or lowering U_{loss} (Fig. 4.4 and Fig. 4.5) reduces the magnitude of the electron energy. For the particular case of $\alpha = 0.05$, it is surprising that the case with the highest electron-wall energy loss also produces the most thrust while the lowest electron-wall energy loss rate results in the least thrust. A cursory inspection of the mean electron energy profiles at this condition, shown in Fig. 4.4, only add to this paradox, since the peak electron energy is higher when the thrust is lower and vice versa.

To explain this paradox, notice that the magnitude of the electron energy in Fig. 4.4 is greater than 40 eV at the thruster exit for all three curves. This results in the entire acceleration zone residing inside the acceleration channel. Thus, for the lowest electron-wall energy loss case ($U_{loss} = 45\ eV$), the electron energy rises fastest. This results in plasma creation deeper in the acceleration channel and a greater chance for ions with a positive axial velocity to impact the channel walls and neutralize before exiting the thruster. As a result, the case with the lowest peak electron energy ($U_{loss} = 15\ eV$) had the fewest ion-wall collisions (25% less than $U_{loss} = 45\ eV$) and thus produced more thrust.

Finally, it is clear from Fig. 4.6 that changing the electron-wall energy loss term can introduce radical changes to the oscillatory behavior of the simulation. In the case of low electron-wall energy loss (α=0.05), the electron temperature is sufficiently high that the ionization process acts virtually instantaneously, whereas in the case of high electron-wall energy loss (α=0.20), the lower electron temperature permits the action of the finite ionization rate dynamics of the breathing mode oscillation.

This section details the very significant effect on thruster performance, centerline energy profiles, and transient behavior that the electron-wall energy loss term has

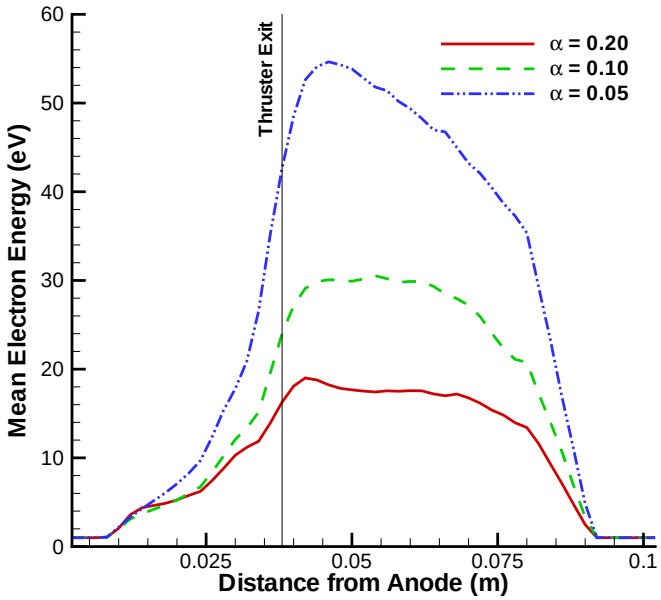


Figure 4.3: UM/AFRL P5 Energy Loss Coefficient – U_{loss}=15 eV

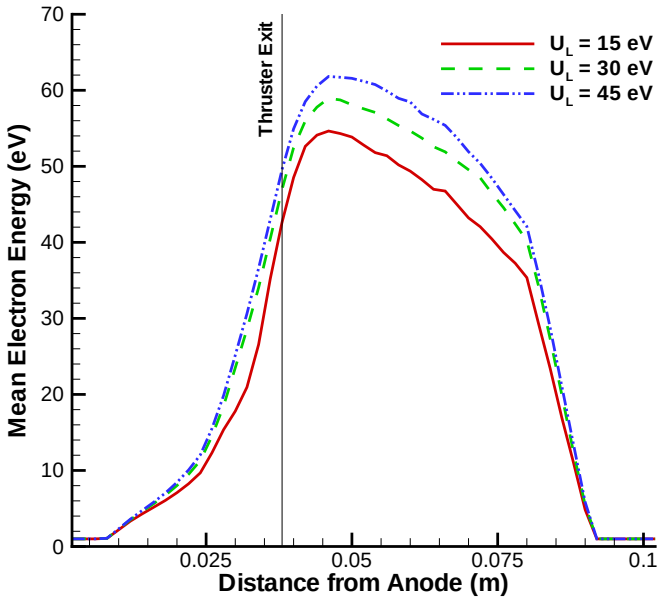


Figure 4.4: UM/AFRL P5 Energy Loss Coefficient – α=0.05

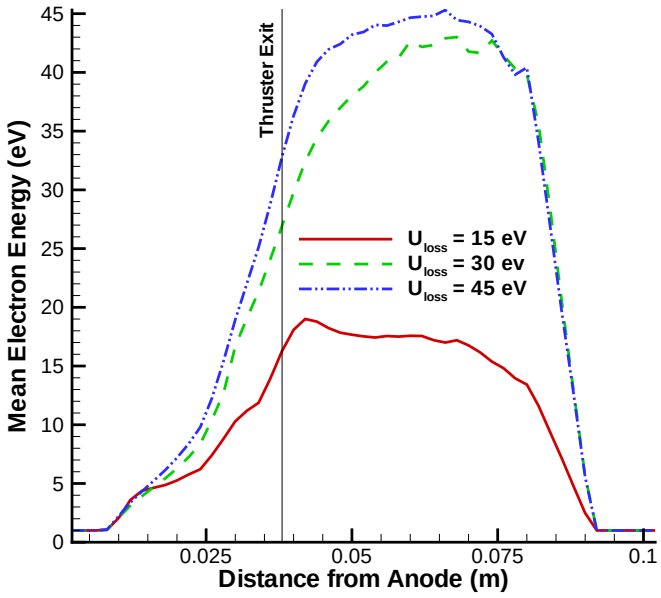


Figure 4.5: UM/AFRL P5 Energy Loss Coefficient – α=0.20

on the simulation of the UM/AFRL P5. Many more effects are not covered, but two important modeling guidelines can be discovered in this section. First, the nonlinear behavior of the exponential term in the electron-wall energy loss formulation couples into the simulation in a far less predictable manner than the multiplicative coefficient α. Second, if the expected maximum electron energy is not known for a simulation running on xenon and finite rate dynamics are expected, the maximum electron energy should be limited to relatively low energies ($\leq 30\ eV$).

4.3 Electron Energy Collision Losses

The ionization and electron energy collision loss rates used in this code are highly sensitive to electron energy. In this thruster simulation, these nonlinear source rates (for ionization) and sink rates (for collisional electron energy loss) represent critical inputs to the code. The complex coupling of ionization and energy transport means

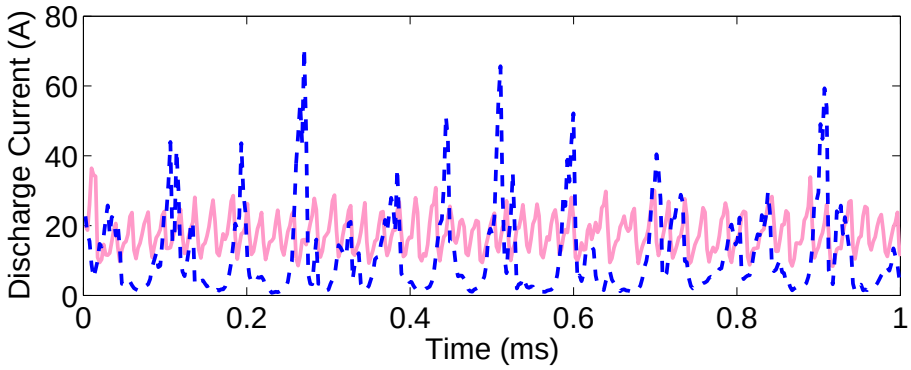


Figure 4.6: UM/AFRL P5 Discharge Current – Constant U_{loss}=15 eV (Solid line – $\alpha = 0.05$, Dashed Line – α=0.20

that even small changes in these rates can lead to simulation of thruster operation in vastly different operating regimes. Evidence of this behavior based on the electron-wall energy loss component of the energy loss frequency is presented in Sec. 4.2. This section deals only with sensitivity to energy loss rates, not ionization rates.

In the code, the total electron energy loss frequency (again, the rate is obtained by multiplying the frequency by the plasma density) is a combination of the electron-wall energy loss frequency and two collision loss terms corresponding to the frequency of inelastic collisions between electrons and the two principle heavy species, Xe and Xe^+. The total electron energy loss frequency is written as:

$$\nu(\varepsilon) = \nu_{walls}(\varepsilon) + \nu_{e-Xe}(\varepsilon) + \nu_{e-Xe^+}(\varepsilon) \tag{4.2}$$

A series of simulations is conducted on the UM/AFRL P5 thruster using the best fit mobility from Sec. 5.1.2.4 in which the component of the electron energy loss frequency due to collisional processes ($\nu_{e-Xe}(\varepsilon)$ and $\nu_{e-Xe^+}(\varepsilon)$) is decreased by 10% and increased by 10%, 20%, and 30% while the electron-wall energy losses are held constant at α=0.20 and U_{loss}=20 eV. The results are presented in Table 4.2. From this data, it is clear that increasing the electron energy collision loss frequency more

than 10% above its baseline value causes significant performance degradation (in the range of ±10%, performance differences can likely be attributed to statistical noise).

Table 4.2: UM/AFRL P5 Rate Sensitivity

ELC	Exit Thrust (mN)	I_{sp} (s)	Efficiency (%)	Discharge Current (A)
-10%	184.3	1830	51.2	11.8
no change	179.3	1791	50.5	11.3
+10%	183.5	1820	51.6	11.5
+20%	167.4	1665	47.9	10.4
+30%	141.7	1418	40.6	8.8

The mean energy profiles for the electron energy collision loss frequency sensitivities in Table 4.2 are provided in Fig. 4.7. These results demonstrate that varying the electron energy collision loss frequency has a profound impact on the mean energy profile. It is clear from these results that the electron energy collision loss frequency must be very accurate to reproduce the correct spatial features of thruster behavior.

The discharge current traces for some of the electron energy collision loss cases studied in Table 4.2 are provided in Fig. 4.8. These results demonstrate that varying the electron energy collision loss frequency greatly influences the oscillation characteristics of the thruster simulation. Again, it is clear from these results that the electron energy collision loss frequency must be very accurate to reproduce the correct temporal features of thruster behavior.

This section illustrates the dependence of the model on the electron energy collision frequency parameter. Although the code needs no particular input since it uses the rates taken directly from Appendix C, there is a substantial degree of uncertainty in the contents of Appendix C itself. Therefore, it is helpful to know that with a relatively high electron-wall energy loss term, even a ±10% error in the electron energy collision loss frequency will not significantly affect thruster performance.

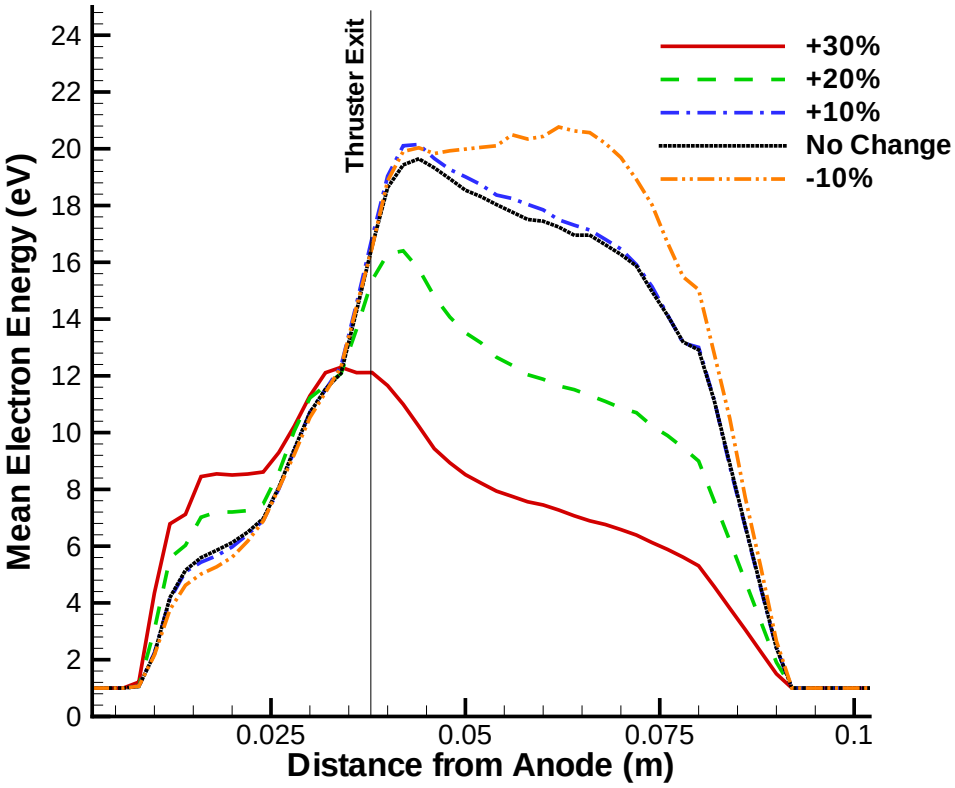


Figure 4.7: UM/AFRL P5 Mean Electron Energy - Variation of energy loss rates

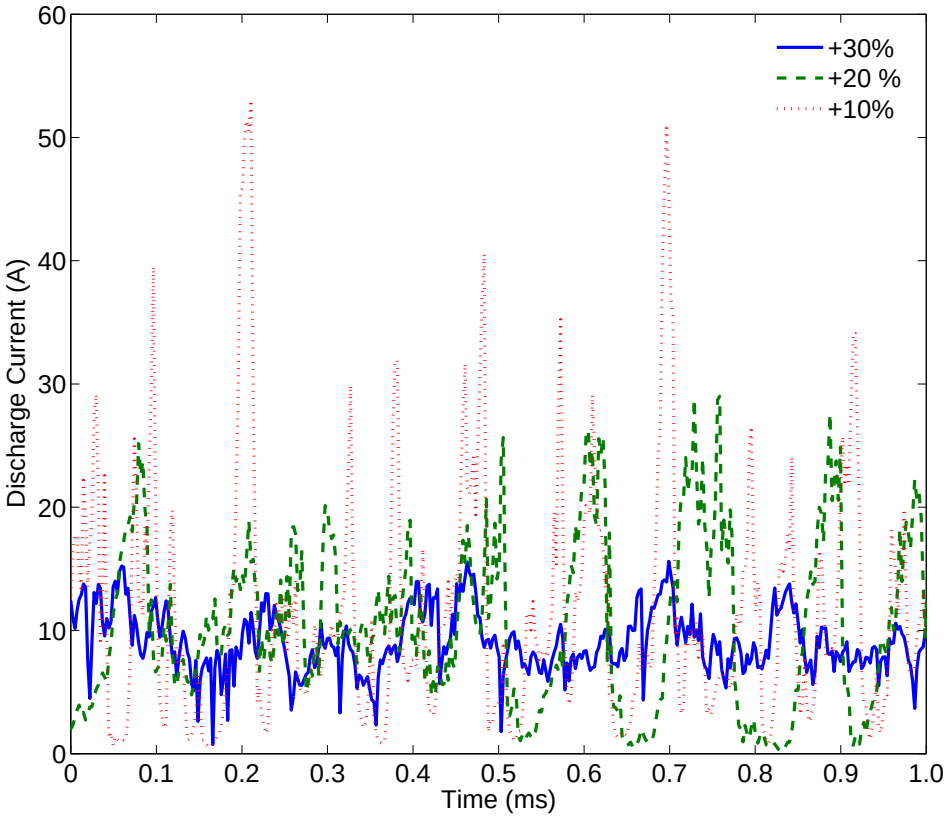


Figure 4.8: UM/AFRL P5 Discharge current trace - Variation of energy loss rates

CHAPTER V

Mobility Modeling and Experimental Validation

Among the many modeling choices necessary in the computational simulation of Hall thrusters, the modeling of one particular physical phenomenon, the electron mobility, stands out as a particularly difficult task. Modeling of the electron mobility is so challenging in part due to an incomplete understanding of the particular physics associated with this phenomenon and in part due to the extreme difficulty in isolating this phenomenon experimentally.

As mentioned in Sec. 2.5.4, the operation of Hall thrusters involves an electron mobility greater than that predicted by classical theory. The fact that Hall thrusters operate so reliability is undeniable proof that additional electron transport mechanisms must exists to allow enough electrons to move across magnetic field lines towards the anode to maintain the necessary discharge current. Since the enhanced electron mobility is so fundamental to thruster operation, it is difficult to isolate its effect experimentally; nevertheless, correctly modeling this additional electron transport mechanism, also known as the "anomalous" mobility, is absolutely critical to the successful numerical simulation of Hall thrusters.

In this section, the performance characteristics of the two principal existing "anomalous" electron mobility models are evaluated through the simulation of the

UM/AFRL P5 Hall thruster operating at 3.0 kW on xenon propellant. In an attempt to explain the performance of these models, a semi-empirical electron mobility, based in part on experimental data, is presented and used in a simulation of the same thruster. These results are validated against an existing dataset of the internal and near-field plasma properties of this thruster configuration. Finally, the NASA-173 Mv1 operating at 7.0 kW on krypton propellant is simulated and a limited performance validation is presented.

5.1 UM/AFRL P5 Hall Thruster

The performance characteristics of the UM/AFRL P5 Hall thruster configuration presented in this section are provided in Table 5.1. As listed in the footnotes to Table 5.1, plasma properties were measured at slightly different flow rates and background pressures than for the measurements of performance data. The numerical simulations presented in this section simulate the nominal configuration used to obtain performance data. This introduces an additional source of error when validating the simulation against the internal and near-field datasets; however, in comparison to the estimated experimental uncertainties in the measured plasma properties (electron temperature – $\pm 20\%$, plasma density – $\pm 50\%$), this uncertainty is considered to lie within acceptable limits.

5.1.1 Computational Models for Anomalous Electron Mobility

Wall-collision mobility and Bohm diffusion are the two most commonly cited mechanisms to provide the "anomalous" electron mobility observed in Hall thrusters. In this code, the anomalous mobility models are coupled into the classical transverse magnetic field electron mobility through an enhanced electron momentum transfer frequency term, ν_m. The five different simulations presented in this section are

Table 5.1: UM/AFRL P5 3 kW Xe Performance[a]

	Experimental	Uncertainty
Discharge Voltage (V)	300	
Discharge Current (A)	10	
Thrust (mN)	180	+1.2/-8
Anode mass flow rate xenon (mg/s)	10.248[b]	
I_{sp} (s)	1744[c]	+20/-131[d]
Efficiency (%)	51	+1/-8.3
Background Pressure (torr)	$1.1 \cdot 10^{-5}$[e]	

[a]Cathode Mass Flow Rate – 0.586 mg/s xenon

[b]2-D internal and near-field data taken at 10.736 mg/s

[c]Actual $I_{sp} = 1650$ s presented in *Haas* (2001) is based on anode plus cathode mass flow rates

[d]Uncertainty based on $I_{sp} = 1650$ s

[e]2-D internal and near-field data taken at $3.2 \cdot 10^{-5}$ torr

all designed to simulate the same 3.0 kW xenon thruster configuration. To this end, various levels of success are achieved; however, the simulations presented in this section reflect reasonable model coefficients designed to best reflect the overall physical effects of the various mobility models. With any of the mobility models presented in this section, individual performance metrics, such as thrust alone or power alone, can be matched more closely by using highly skewed model coefficients. Such choices tend to force other performance parameters away from optimum and at worse can potentially lead to the breakdown of some of the underlying assumptions of the code while returning apparently reasonable results.

The anomalous mobility models selected for this section are as follows: (1) Wall-Collision mobility with $\alpha = 0.10$, (2) Bohm Diffusion Mobility with $\alpha_B = 0.005$ ("low" Bohm mobility), (3) Bohm Diffusion Mobility with $\alpha_B = 0.015$ ("high" Bohm mobility), (4) Mixed mobility: wall-collision mobility with $\alpha = 0.15$ inside the ac-

celeration channel and Bohm mobility with $\alpha_B = 0.020$ outside the channel (Mixed Outer), and (5) Mixed mobility: wall-collision mobility with $\alpha = 5.0$ inside the acceleration channel and Bohm mobility with $\alpha_B = 0.008$ outside the channel (Mixed Inner).

5.1.1.1 Performance Data

The performance data for the computational mobility models are presented in Table 5.2. The principal figure of merit for performance data is the thrust. According to this criterion, it appears that the high Bohm and both mixed mobility models perform quite successfully. The failing of the low Bohm model is not surprising since it is included in this dataset primarily to further the understanding of these particular mobility models. The wall-collision model will be discussed later in this section.

Another important listing in Table 5.2 is the electron current. Since a negative electron current means that electrons are heading away from the anode, this indicates that the effective cathode plane is somewhere inside the active simulation domain. The effective cathode plane is typically located at a local potential minimum, and because the code limits the lower potential to $\phi(\lambda_c) = 0$, then λ_c must represent the effective cathode plane. Since the discharge current in the code is evaluated simply as the sum of of the ion current and the electron current, the case of a negative electron current at λ_c implies that the ion beam current is greater than discharge current for at least some region of the thruster. (There is no actual cathode model so this electron current does not represent the actual neutralization current.) This is a serious problem, for although the discharge current provided by an idealized thruster can be equal to the beam current, in actual operation, the beam current rarely exceeds 80%

of the discharge current. The only way for the negative electron current condition to be physically realistic is if the code includes a realistic cathode model. Therefore, negative electron currents indicate that, for this particular code, the mobility model is operating out of the physically realistic parameter space. In general, increasing the coefficient of the anomalous mobility correction term is sufficient to return to a physically realistic parameter space.

The wall-collision model is optimized for thrust, and doing so required reducing α to increase the electron energy and hence promote ionization. The particular choice of $\alpha = 0.1$ seems reasonable at first since $\alpha = 0.2$ is cited as the best coefficient for the SPT-100 by *Boeuf and Garrigues* (1998). The wall-collision simulation, while demonstrated here to be physically unrealizable, is still analyzed in this chapter to demonstrate how other aspects of this mobility model provide desirable simulation characteristics. The breakdown of the wall-collision model does not occur catastrophically. Instead, one of the underlying assumptions of the code is quietly violated while performance data stay reasonable. This is because the negative electron current collected at λ_c represents only a local violation of the code physics. In fact, upstream of the effective cathode plane, the simulation results remain physically possible.

Finally, the thruster power listing in Table 5.2 has a direct dependence on the discharge current. The electron current can be a major contributor of the discharge current, and since the electron mobility is one of the principal plasma properties responsible for the magnitude of the electron current, the anomalous mobility model selection has a significant impact on the simulated thruster power. Since thrust performance is based on the ion current while the thruster power is based on the total current, simulations which produce comparable amounts of thrust can show wide variation in thruster power. In particular, while the high Bohm model provides

almost exactly the experimentally observed level of thrust, it predicts a required power over 70% greater than the power input actually necessary to run the thruster. On the other hand, the Mixed Outer model underpredicts the experimental thrust by only 6% while maintaining almost exactly the experimental power input. The thrust efficiency scales inversely with the discharge current, so similar poor thruster efficiency results when the electron mobility (and, consequently, the electron current) is too great.

5.1.1.2 Centerline Mobility

Centerline electron mobility data is presented in Fig. 5.1. Looking at the region inside the Hall thruster, the Wall-Collision model, the Mixed Outer model, and the Mixed Inner model illustrate the dependence of the mobility on the parameter α, which is 0.10, 0.15, and 5.00, respectively. All the models except the Wall-Collision model have a Bohm mobility dependence in the near-field region (downstream of the thruster exit) corresponding to values for α_B of 0.008, 0.015, 0.020, and 0.035. Details of the centerline electron mobility profiles will be explored in the following sections.

5.1.1.3 Potential

Internal and near-field plasma potential data are presented in Fig. 5.2 through Fig. 5.6. Some care must be taken in analyzing Fig. 5.2 since it is only consistent with the underlying physics up to the effective cathode plane. The potential exhibits a very steep decline about 2.4 cm from the anode face. This behavior is entirely consistent with the sharp mobility drop (by over a factor of 100) from the anode. This very large potential gradient means that the ions accelerate to most of their maximum speed in a relatively short distance. Since the discharge current must remain constant

Table 5.2: UM/AFRL P5 Computational Mobility Model Performance Data

	Wall-Collision [a]	Low Bohm[b]	High Bohm[c]	Mixed Outer[d]	Mixed Inner[e]
Thrust (mN)	135.9	154.5	182.7	169.4	173.9
I_{sp} (s)	1372	1544	1824	1686	1728
Ion Current (A)	6.75	11.07	11.58	9.90	10.92
Electron Current (A)	-1.00	0.33	7.41	0.72	2.34
Discharge Current (A)	5.75	11.41	19.00	10.63	13.26
Power (W)	1582	3137	5224	2922	3646
Thrust Efficiency (%)	58	37	31	48	40

[a] $\alpha = 0.10$, Xe^+ Only

[b] $\alpha_B = 0.015$

[c] $\alpha_B = 0.035$

[d] $\alpha = 0.15$, $\alpha_B = 0.020$

[e] $\alpha = 5.00$, $\alpha_B = 0.008$

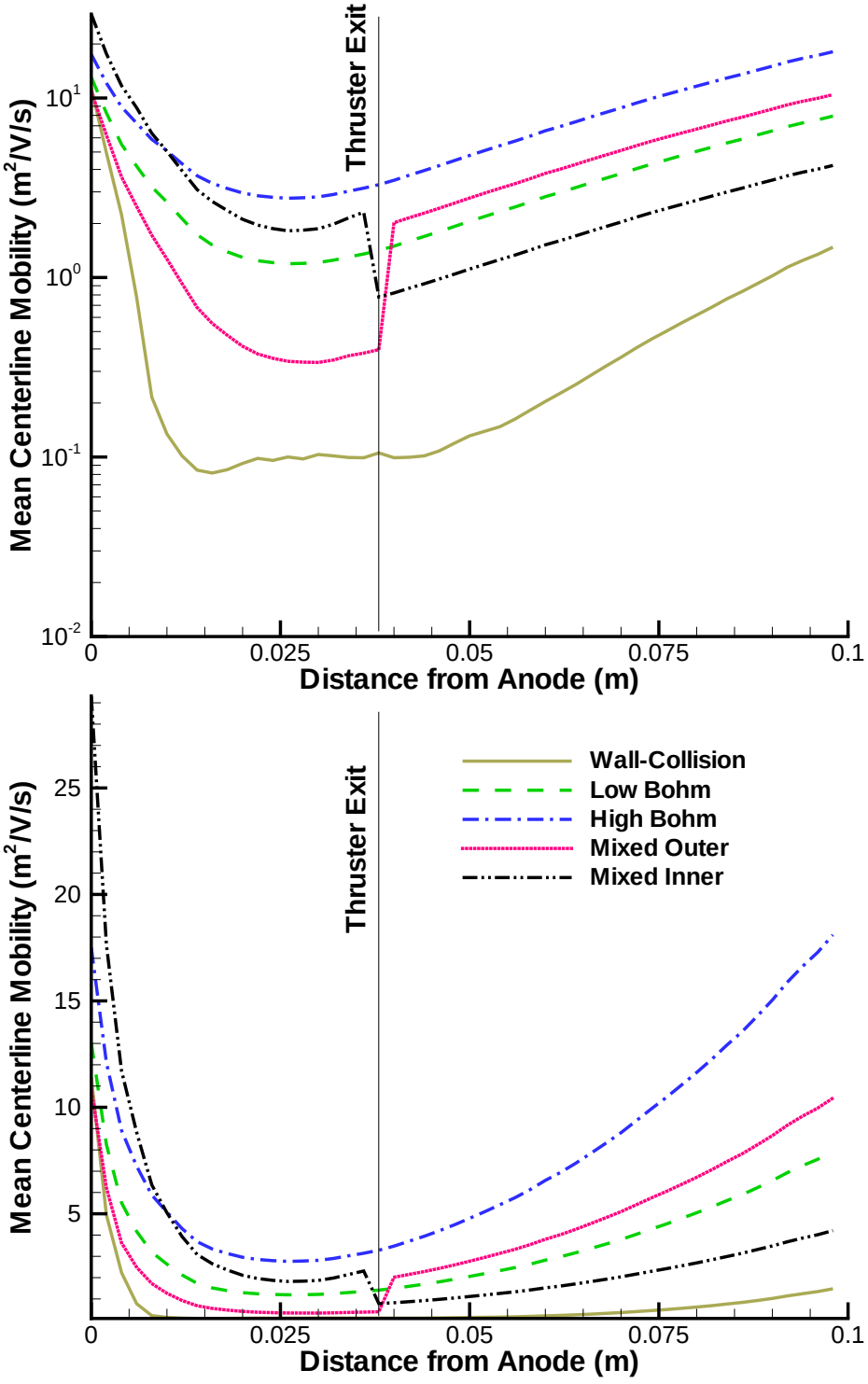


Figure 5.1: UM/AFRL P5 Mean Centerline Mobility

upstream of the effective cathode plane, this means that the electron current rapidly drops through the acceleration zone and is only fraction of the discharge current for the rest of the channel and near-field. (This drop is rapid enough that even though the mobility remains very small, the electron current dimishes to keep pace.) Near λ_c, the thermal pressure actually pushes the electrons away from the thruster more efficiently than the electric field accelerates them towards the thruster, leading to the negative electron current observed in the simulation. Note: When ν_{neut} is very low, then the effect of adding a constant ν_w term becomes quite pronounced. The very flat region of the mobility profile in Fig. 5.1 for this case from 1.5 cm from the anode to 5 cm from the anode corresponds directly to a region with severe neutral depletion such that $\nu_w \geq \nu_{neut}$.

Next, Fig. 5.3 and Fig. 5.4 demonstrate the effect of increasing α_B. Supposing that $\alpha_B \cdot \omega_{c,e} \gg \nu_{neut}$, then the correct scaling for μ in the limit of Bohm diffusion, $\mu \propto 1/B$, is reached. Since this $\alpha_B \cdot \omega_{c,e} \gg \nu_{neut}$ condition is only really satisfied in the near-field region, the low α_B and high α_B mobility profiles are both strongly modified in the acceleration channel near the magnetic field peak. Since the α_B correction for the low Bohm case is smaller than for the high Bohm case, the low Bohm mobility case shows more moderating effects from ν_{neut} near the thruster exit of the acceleration channel. This is demonstrated by the high positive curvature displayed by the high Bohm model mobility. The effect of this increased positive curvature in the mobility profile can be clearly seen in the centerline mobility profiles for the two Bohm configurations in Fig. 5.1. For the low Bohm case, the flatter mobility profile results in an almost linear potential gradient throughout the acceleration channel while for the high Bohm case, the mobility drops more steeply in the channel and rises more steeply outside of the channel, resulting in a much steeper potential

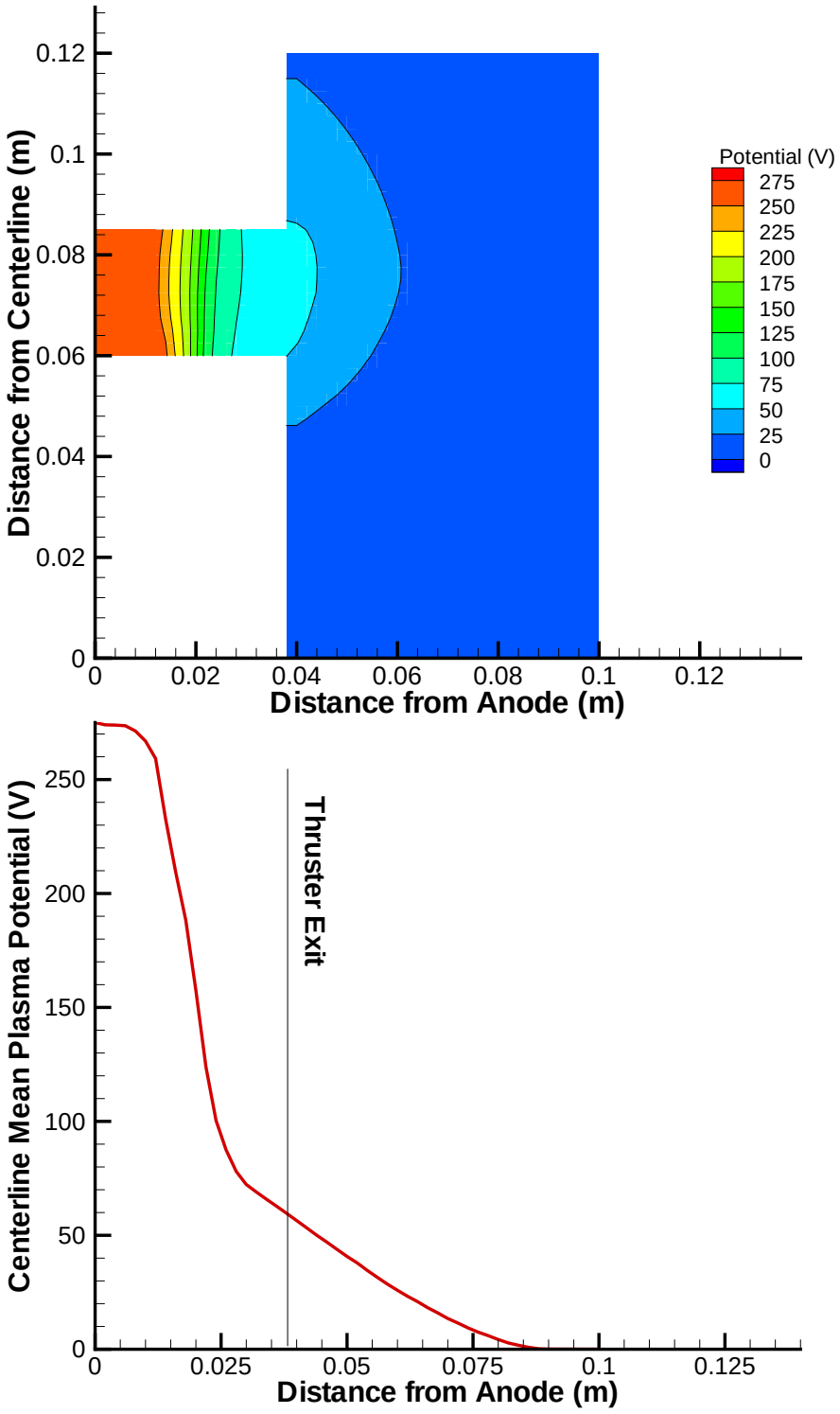


Figure 5.2: UM/AFRL P5 Mean Potential (Wall-Collision mobility)

gradient.

Although the peak potential gradient is generally close to the minimum in the mobility curve, other factors, such as the electron current, electron temperature and pressure gradient must couple with the mobility to establish a self-consistent potential distribution. As a consequence, the absolute location of the peak potential gradient cannot be established from only the electron mobility profile.

The wall-collision model is based on the theory by *Morozov and Shubin* (1984) that electron-wall collisions are the mechanism for enhancing electron transport inside the thruster. Accordingly, this theory is better suited to the acceleration channel (where there are walls) than to the near-field of the thruster. The theory behind the mechanism for Bohm mobility, presented by *Esipchuck and Tilinin* (1976), is based on transport from azimuthal drift waves in the plasma which can exist only in regions with decreasing gradients in the magnetic field. Consequently, the Bohm model for anomalous mobility should not be used inside the thruster channel where the magnetic field criteria to support these azimuthal drift waves is not met.

To incorporate these ideas, mixed mobility models for Hall thrusters have been presented by *Hagelaar et al.* (2002) with a wall-collision mobility model inside the thruster and a Bohm mobility model outside the thruster. The approach used in the present work to blend the two mobility regimes is slightly different than the approach presented by *Hagelaar et al.* (2002); however, the fundamental idea of using wall-collision mobility inside the thruster and Bohm mobility in the near-field is identical.

The use of a mixed mobility model, while better capturing the theoretical physics of the problem, introduces extra dimensions to the model parameter space. For this work, the boundary between the two models is fixed at the thruster exit, so now

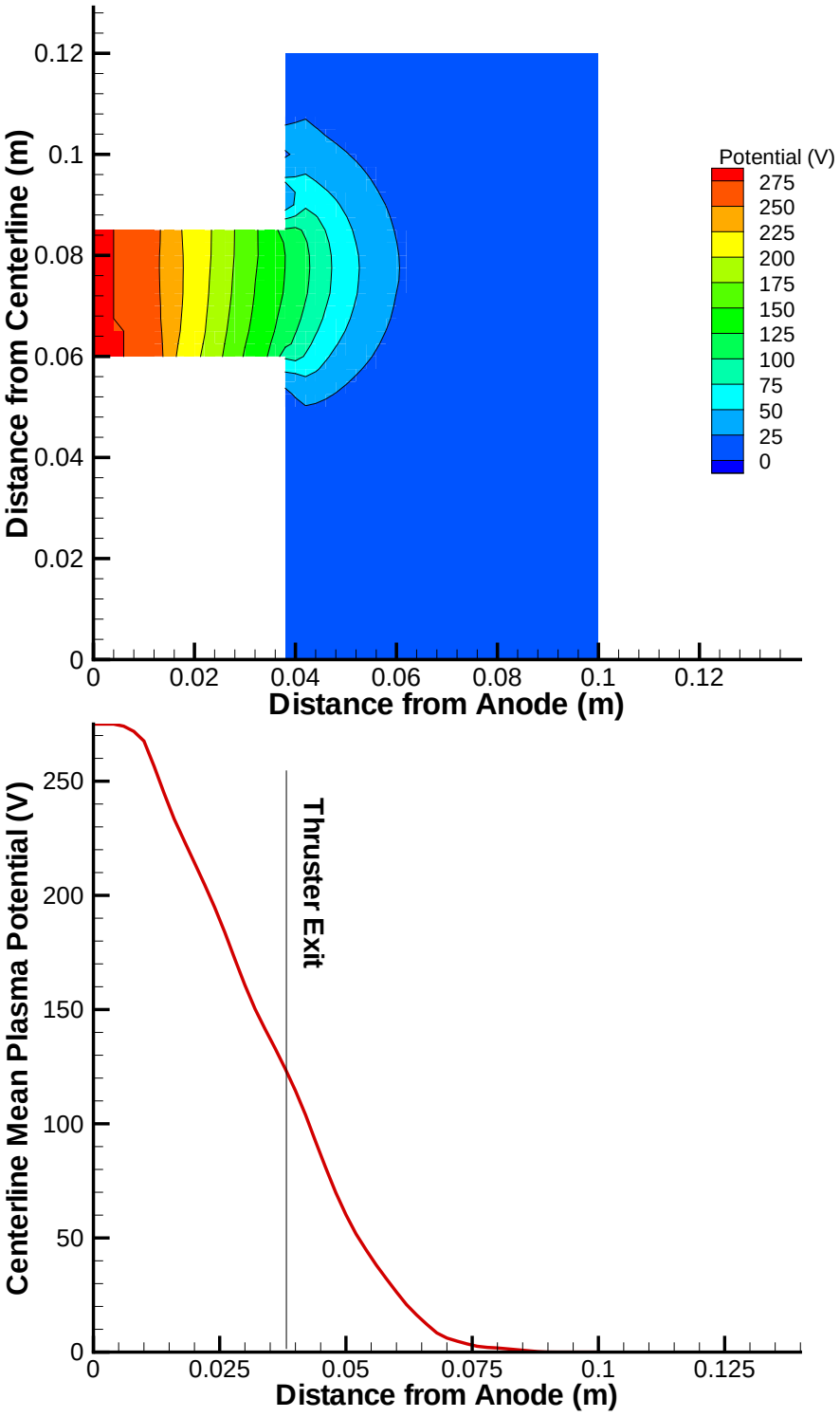


Figure 5.3: UM/AFRL P5 Mean Potential (Low Bohm mobility)

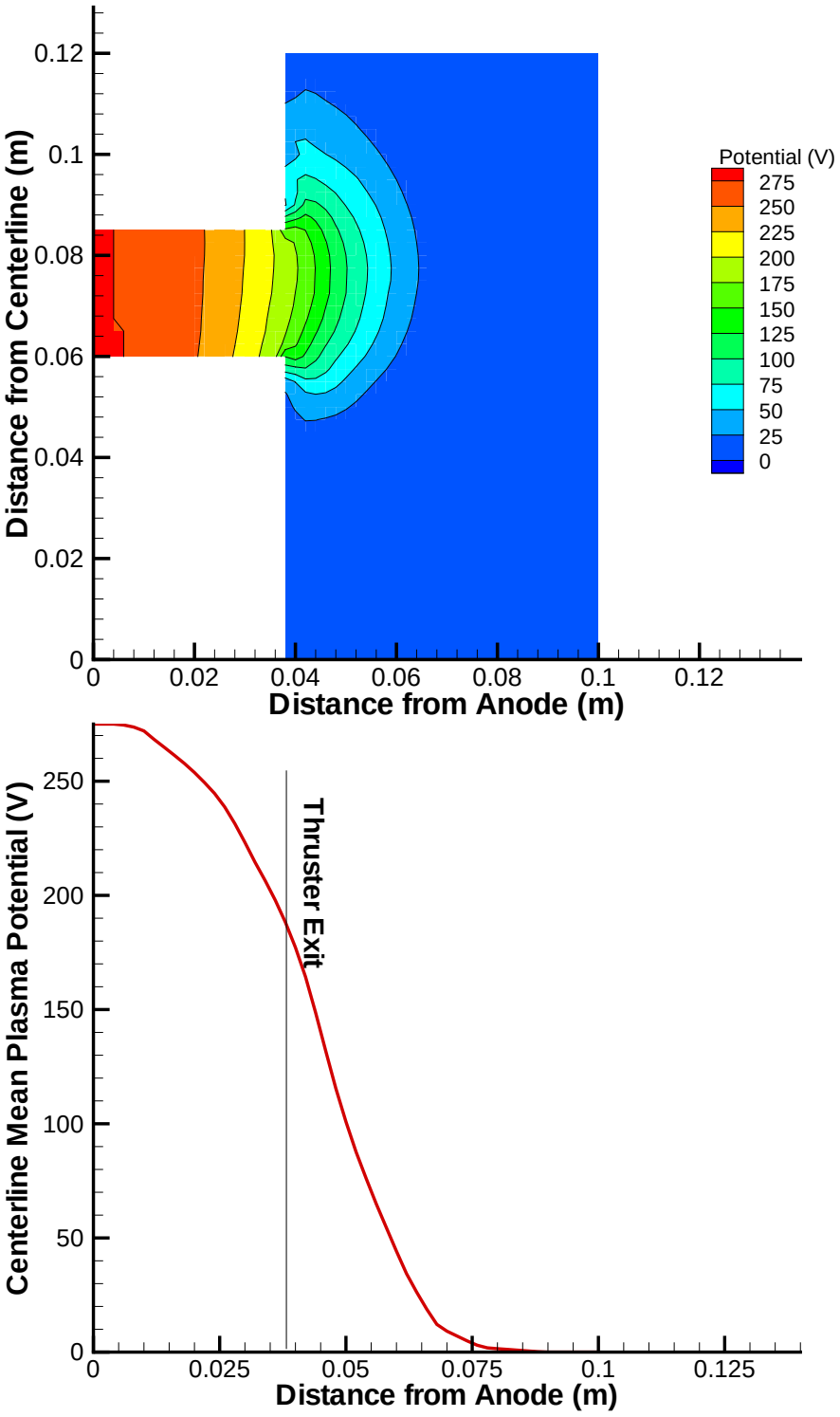


Figure 5.4: UM/AFRL P5 Mean Potential (High Bohm mobility)

two parameters, α inside the channel and α_B outside the channel, are necessary to describe the model. The two simulation results presented in this section are referred to as the Mixed Outer model ($\alpha = 0.15$, $\alpha_B = 0.020$) with higher mobility outside the channel and the Mixed Inner model ($\alpha = 5.0$, $\alpha_B = 0.008$) with higher mobility inside the channel.

The results presented in Fig. 5.5 demonstrate the tendency of a high mobility in the near-field of the thruster to force the acceleration zone into the acceleration channel. Figure 5.6 demonstrates the opposite behavior when the near-field of the thruster has a low mobility relative to the acceleration channel. By varying the strength of these coefficients, it is possible to control the magnitude of the potential drop inside the channel. It is not possible, within the framework of this implementation strategy, to change the relative shape of the mobility curve beyond the single control parameter (α or α_B) in each region of the thruster. As a result, for the Mixed Inner mobility model, a small cusp in the mobility profile just upstream of the thruster exit is sufficient to induce a discontinuity in the gradient of the centerline potential just after the thruster exit.

5.1.1.4 Mean Electron Energy

It is difficult to compare the different model simulations to each other directly since the parameters of the electron energy wall loss model are tuned in some of the simulations to achieve particular performance targets. The energy loss parameters used for each model are shown in Table 5.3. Note that the electron energy loss model parameter α has a dual function as the leading term in both the electron energy loss parameter and the mobility parameter ν_w whenever the wall-collision mobility model is used.

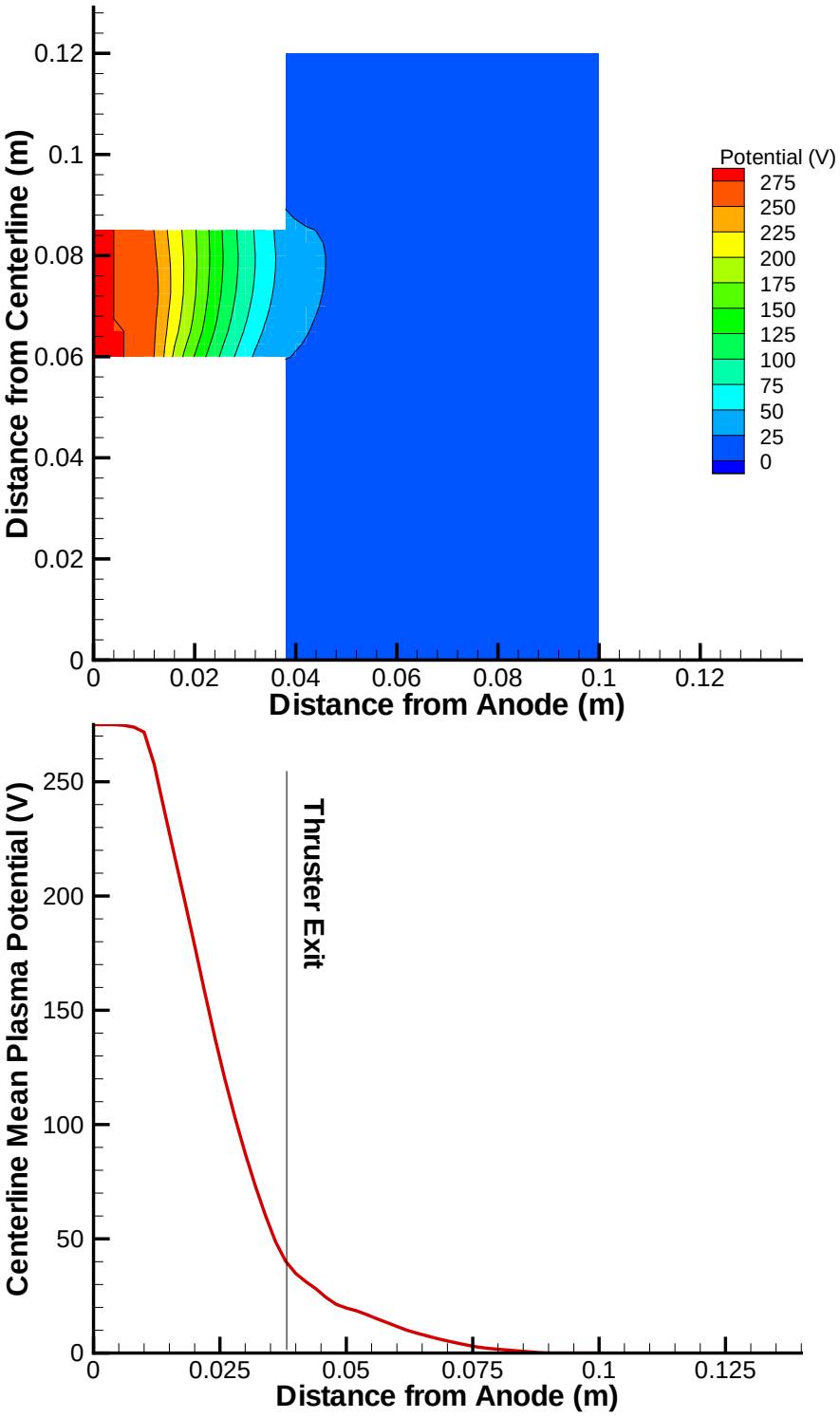


Figure 5.5: UM/AFRL P5 Mean Potential (Mixed Outer mobility)

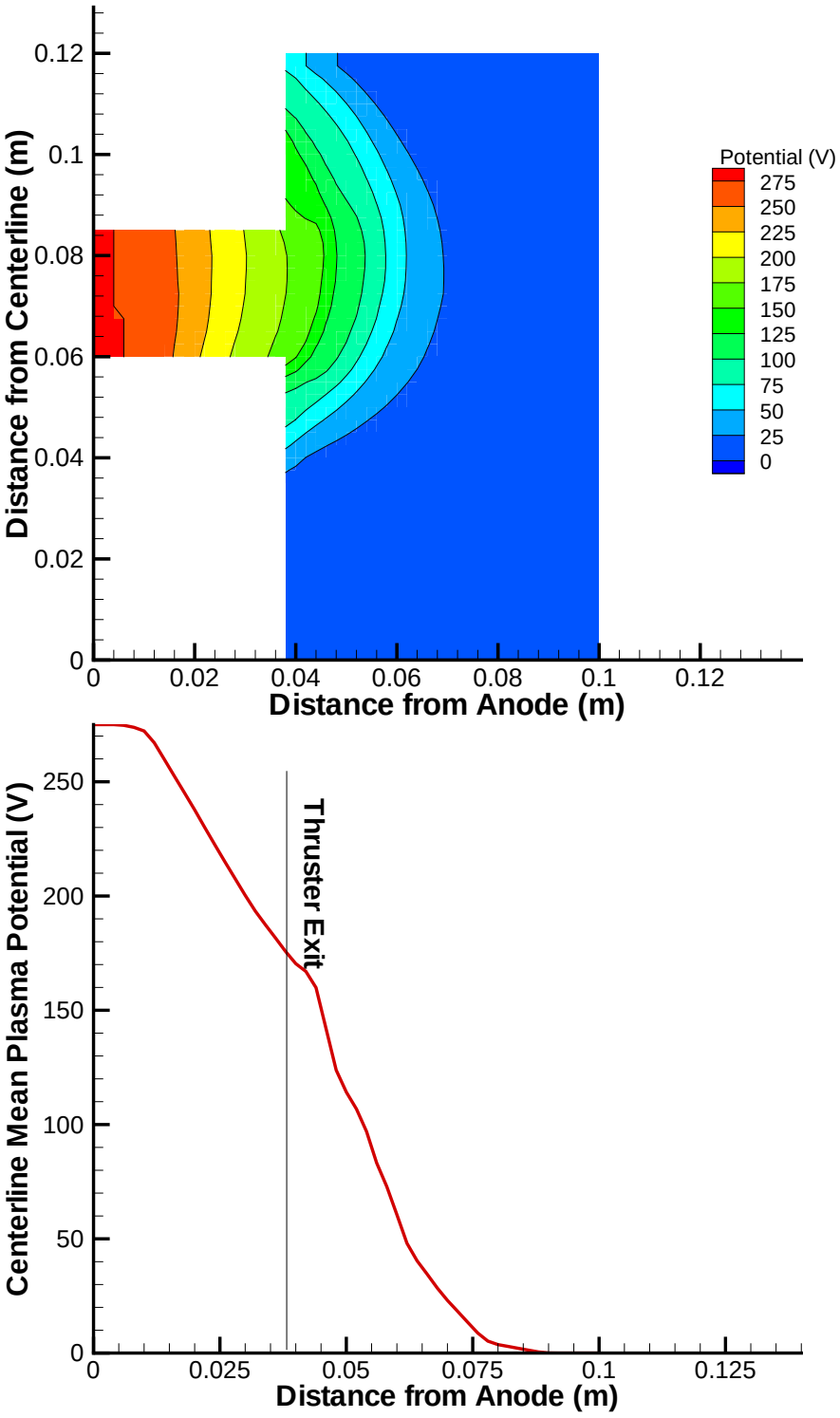


Figure 5.6: UM/AFRL P5 Mean Potential (Mixed Inner mobility)

Table 5.3: UM/AFRL P5 Computational Model Energy Loss Parameters

	α	U_{loss} (eV)
Wall-Collision	0.10	20
Low Bohm	0.20	15
High Bohm	0.20	15
Mixed Outer	0.15	15
Mixed Inner	5.00	50

Essentially, the electron energy wall loss parameter (see Sec. 2.6.3) functions as an energy limiter by preferentially quenching high-energy electron populations through an exponential term. As long as the assumptions regarding the discretization of physical space using the thermalized potential are accepted, the use of a "wall"-loss based energy parameter in the near field of the thruster is not unreasonable due to high electron mobility along magnetic field lines. Not only is this term permissible in the near field, but more efficient energy loss mechanisms in the near field region would allow for better agreement with the experimental data.

Despite the simplicity of the electron energy loss term, significant dynamics occur in the electron energy profile due to the mobility profile of the plasma. The first coupling comes from the assumption (see Sec. 2.6) that the thermal diffusivity of electrons is equal to their mass diffusivity which is related to the electron mobility through the Einstein relationship. The second coupling mechanism comes through the ohmic heating term $j_e \cdot E$, which increases linearly with the electron mobility. This coupling between the mobility and electron energy generation is demonstrated quite clearly in the centerline mean energy profiles presented in Fig. 5.7.

The three models (High Bohm, Mixed Outer and Mixed Inner) are able to adequately predict the same thrust; however, only two of the three demonstrate the same trends in the electron energy profile. In particular, the High Bohm and the Mixed

Inner profiles are both characterized by an energy peak at less than 1 cm downstream of the thruster exit. The extremely strong energy loss parameter $\alpha = 5.00$ of the Mixed Inner profile leads to a very damped mean electron energy profile. Clearly, the ohmic heating in this case peaks at 1 cm downstream of the thruster exit, as indicated by the 14 eV peak temperature here. This is also the location of the discontinuity in the potential gradient observed in Fig. 5.6.

Both the Wall-Collision and Mixed Outer models experience the greatest amount of ohmic heating very deep inside the acceleration channel. The high neutral density in this region leads to large ionization losses which keep the peak electron temperature low. All these models demonstrate zero or negative curvature in the temperature profile in the near-field region. These results do not compare well with existing experimental data, and further discussion of this behavior is presented later in this chapter.

5.1.1.5 Discussion

Existing models for anomalous electron mobility offer a useful tool to rapidly evaluate possible thruster operating conditions. With proper parameter choices, some performance metrics can be reached by optimizing a single parameter (as in the Bohm model presented in this section). Other models, such as the wall-collision model, while not designed to simulate the entire domain, are nonetheless useful in the construction of more elaborate, mixed mobility models. The parameter space over which the coefficients for these mobility models are chosen is very important because realistic thrust performance data can be produced while fundamental model assumptions are being violated. Furthermore, fixed performance metrics can be achieved with different mobility models and vastly different internal and near-field

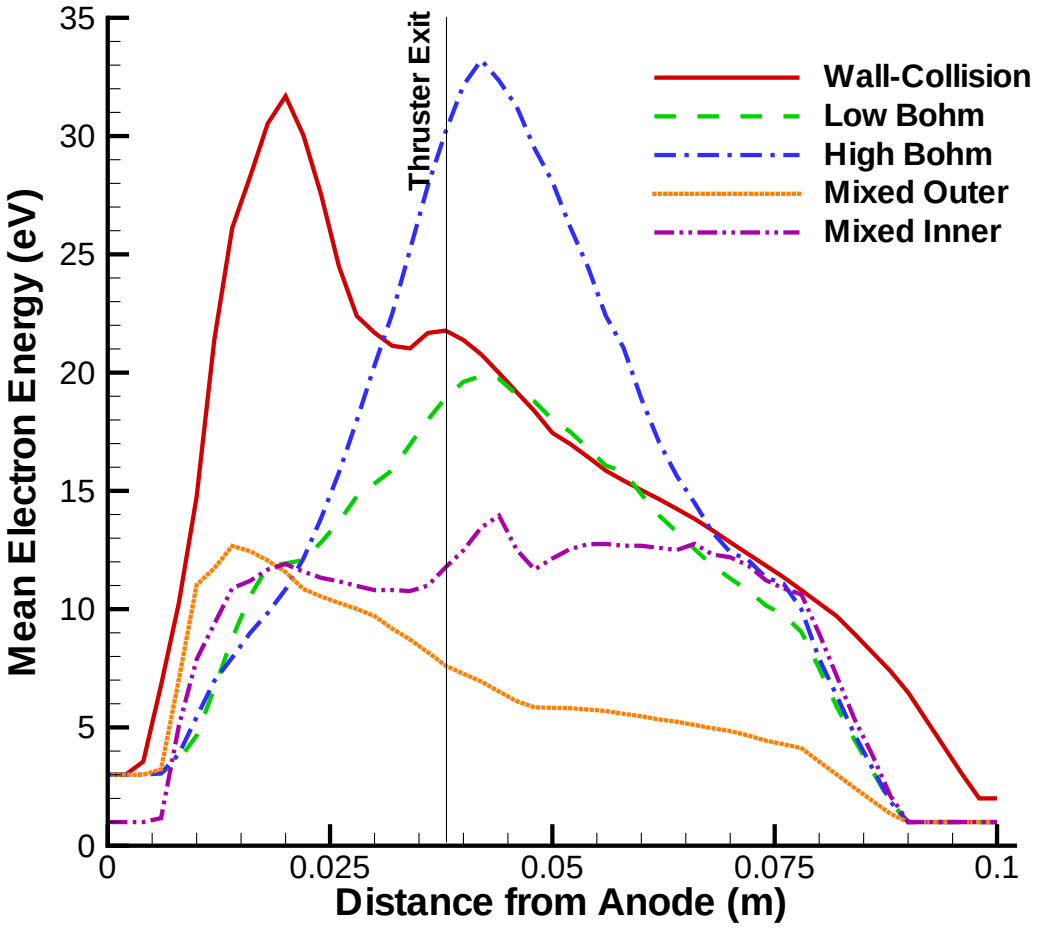


Figure 5.7: UM/AFRL P5 Mean Centerline Energy

plasma properties. Against this backdrop, more complicated, mixed mobility models have been developed which allow for more user control over the mobility profile while maintaining the theoretical underpinnings of these corrections. The goal of the next section is to establish an experimentally influenced baseline mobility for the UM/AFRL P5 Hall thruster running at 3.0 kW and to validate this mobility profile against experimental data.

5.1.2 Semi–Empirical Electron Mobility

The very substantial set of internal Hall thruster measurements taken by *Haas* (2001) allows for the evaluation of the electron mobility perpendicular to magnetic field lines (referred to simply as the "mobility" for the duration of this section); however, the electron mobility is critically dependent on the electron current density profile. Details on the assumptions needed to formulate the semi-empirical electron mobility and the results obtained are provided in this section.

5.1.2.1 Experimental Data

The condition studied is the 3.0 kW xenon operating point for the UM/AFRL P5 thruster. Available experimental data include axial traces of the plasma potential, electron temperature, and plasma density from 10 mm from the anode face to 180 mm from the anode face in 1 mm increments. Potential, plasma density and electron temperature data were gathered at 78.5 mm, and 83.5 mm from the thruster centerline. Raw data for the 78.5 mm case is presented in Fig. 5.8.

5.1.2.2 General Form

The electron mobility perpendicular to field lines can be reformulated from Eqn. 2.30 and Eqn. 2.32 to read as follows:

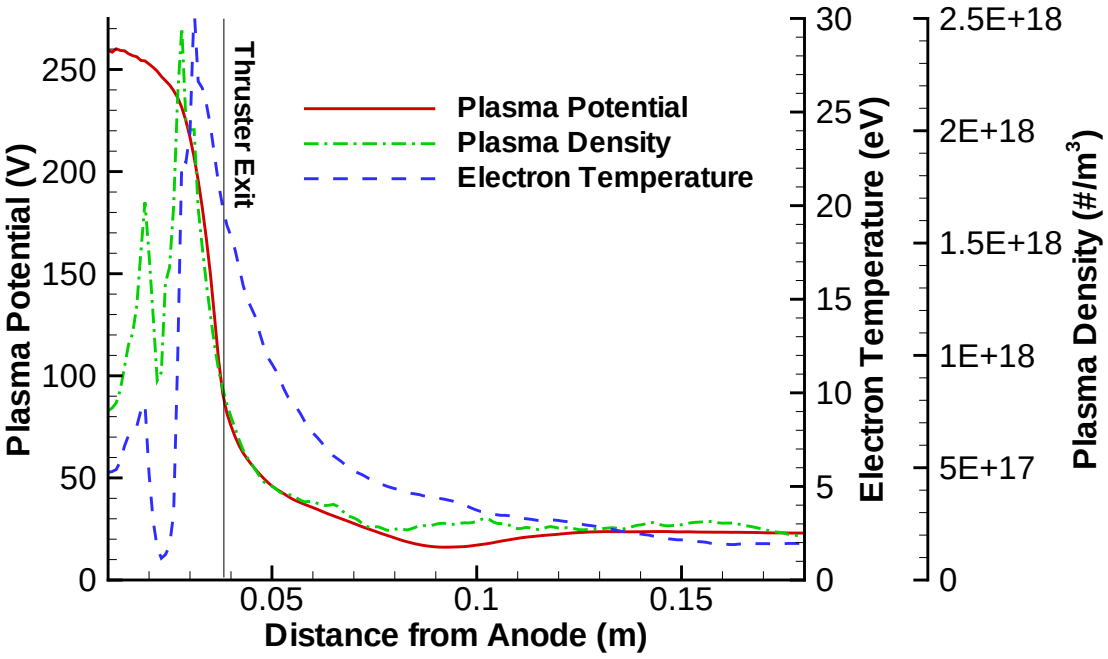


Figure 5.8: UM/AFRL P5 Plasma Properties – 78.5 mm from Centerline (Solid line – Plasma Potential, Dash-Dotted line – Electron Temperature, Dashed line - Plasma Density)

$$\mu = \frac{j_{e_\perp}}{en_e(E_\perp + \frac{1}{n_e e}\nabla_\perp p_e)} \tag{5.1}$$

From this equation, it is clear that the only value not measured which needs to be supplied to evaluate the mobility is the electron current density, $j_{e_\perp}$. This analysis is based on a 1-D model, so all directional quantities in Eqn. 5.1 are considered to be perpendicular to the magnetic field lines. Finally, only a single set of data (combined potential, temperature, and density traces) is considered at a time and these values represent plasma properties which are constant along radial slices of the acceleration channel and near-field domain.

The electron current profile in the acceleration channel is fairly well understood. Since the discharge current, which represents the sum of the ion current and electron current, must be constant through the acceleration channel due to current conservation, as long as the ion current is known, the electron current is also known. The ion current starts at or near zero (depending on the presence of an anode presheath) at the anode, so to maintain a constant discharge current, the electron current must be equal to (or larger, in the case of an anode presheath) the discharge current near the anode. Since the diameter of the acceleration channel is fixed, as the ions are created and accelerated through the thruster, the net ion current density increases and the electron current density decreases correspondingly.

A similar argument holds in the very near-field of the plume, before the effective cathode plane is reached. The behavior of the electron current density is to diminish further in exact (and opposite) concert with the ion current. Critically, the electron current density, regardless of its magnitude, must remain finite and positive in the region upstream of the effective cathode plane. Any behavior to the contrary implies that the ion current density is actually larger than the discharge current density,

which is not a physically acceptable case.

At some point in the near-field of the plume, the bulk electron motion is no longer in the direction of the anode but is now towards the plume. (Besides providing the necessary electrons to maintain the discharge, the cathode must also provide an electron source, equal in magnitude to the maximum beam current, to neutralize the plume.) At this point, since the electrons are now moving away from the thruster instead of towards the thruster, the current contribution switches from positive to negative.

To determine the ion current density, an idealized ion velocity trace is created which considers the "perfect" acceleration of an ion to the local thruster potential. The resulting velocity trace is shown in Fig. 5.9. This assumption is not unreasonable, as the maximum velocity achieved by a singly charged ion assuming perfect acceleration is around 19 km/s while the thruster exhibits an I_{sp} of around 1750 s (implying an effective propellant exit velocity of around 17.5 km/s).

Theoretically, it is possible to directly calculate the ion current density by the multiplication of the plasma density and the idealized ion velocity trace. In practice, since the plasma properties are not radially uniform, the 1-D assumption and measurement errors lead to an ion current density which is roughly five times larger than the discharge current density. (The discharge current density is a function of the area of 1-D radial slices of the thruster and near-field plume. A 45 degree divergence angle in the near-field is considered to evaluate the cross sectional area over which the discharge current density is evaluated.) To compensate, the ion current density is divided by six. This results in a peak ion current density near the effective cathode plane which is only 82% to 92% of the discharge current density. This is the equivalent of selecting an electron current equal to 8% to 18% of the discharge

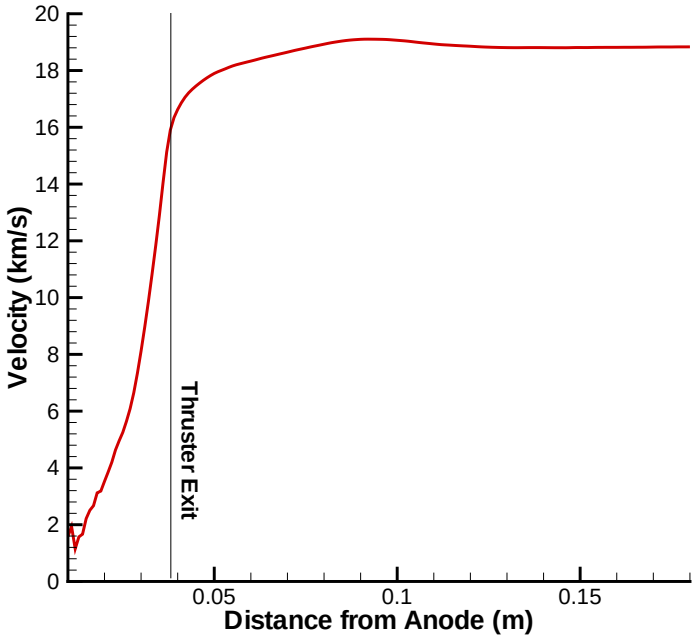


Figure 5.9: Idealized Ion Velocity Trace – 78.5 mm from Centerline

current.

The remaining task to calculate the electron current density is to locate the effective cathode plane (at which point the electron current density switches sign). Experimental measurements demonstrate that distinct regions of ion deceleration may occur as the plasma potential rises downstream of the thruster. For the UM/AFRL P5 thruster, the primary deceleration zone is located roughly 5 cm from the thruster exit. It has been theorized that the beginning of the potential rise characterizing the primary deceleration zone also serves as the effective cathode plane. Accordingly, the electron current density is negative downstream of this point which marks the downstream end of this analysis.

Based on the assumptions detailed in this section, the inferred electron current densities for two axial trace locations (78.5 mm from the thruster centerline and 83.5

mm from the thruster centerline) for the 3.0 kW case are presented in Fig. 5.10. The location of the effective cathode plane is obvious from these electron current density profiles.

5.1.2.3 Results

The resulting semi-empirical electron mobility traces are presented in Figs. 5.11–5.12. Additional information contained in each graph is the classical electron mobility and the Hall current density. The classical electron mobility is based on thruster simulations run with the semi-empirical mobility developed in this section. Since the classical electron mobility is based solely on the magnetic field and neutral density, any errors in the classical electron mobility presented in these graphs is due solely to errors in the computed neutral density. These errors are expected to be insignificant compared to the contribution of the anomalous mobility to the semi-empirical mobility. The Hall current density for this thruster, also presented by *Haas* (2001), is based on the following formula:

$$j_{hall} = en_e \frac{E_z}{B_r} \tag{5.2}$$

5.1.2.4 Simulation using Semi-Empirical Electron Mobility

The semi-empirical electron mobility at 78.5 mm from centerline case is used as a guide to create a new mobility profile as shown in Fig. 5.13. Care is taken to ensure that the low mobility region near the thruster exit is accurately captured in what will be referred to as the "best fit" curve. The drop in the mobility near the domain exit represents the location of the effective cathode plane. Since λ_c reaches a maximum at about 7.9 cm from the anode for this simulation, the active domain is within the effective cathode plane. No semi-empirical mobility data exist within

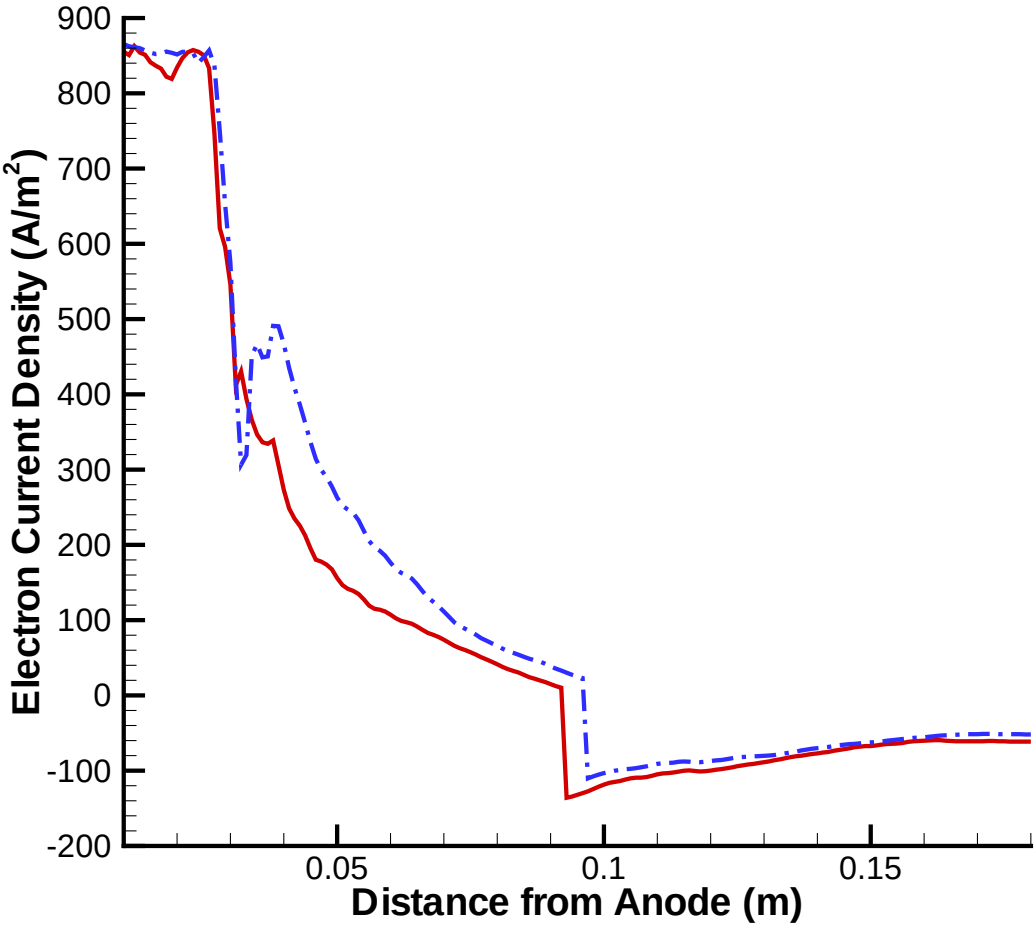


Figure 5.10: UM/AFRL P5 Electron Current Density – (Solid line – 78.5 mm from centerline, Dash-Dotted line - 83.5 mm from centerline) *Note: The location of the effective cathode plane is 5–6 cm from the thruster exit.*

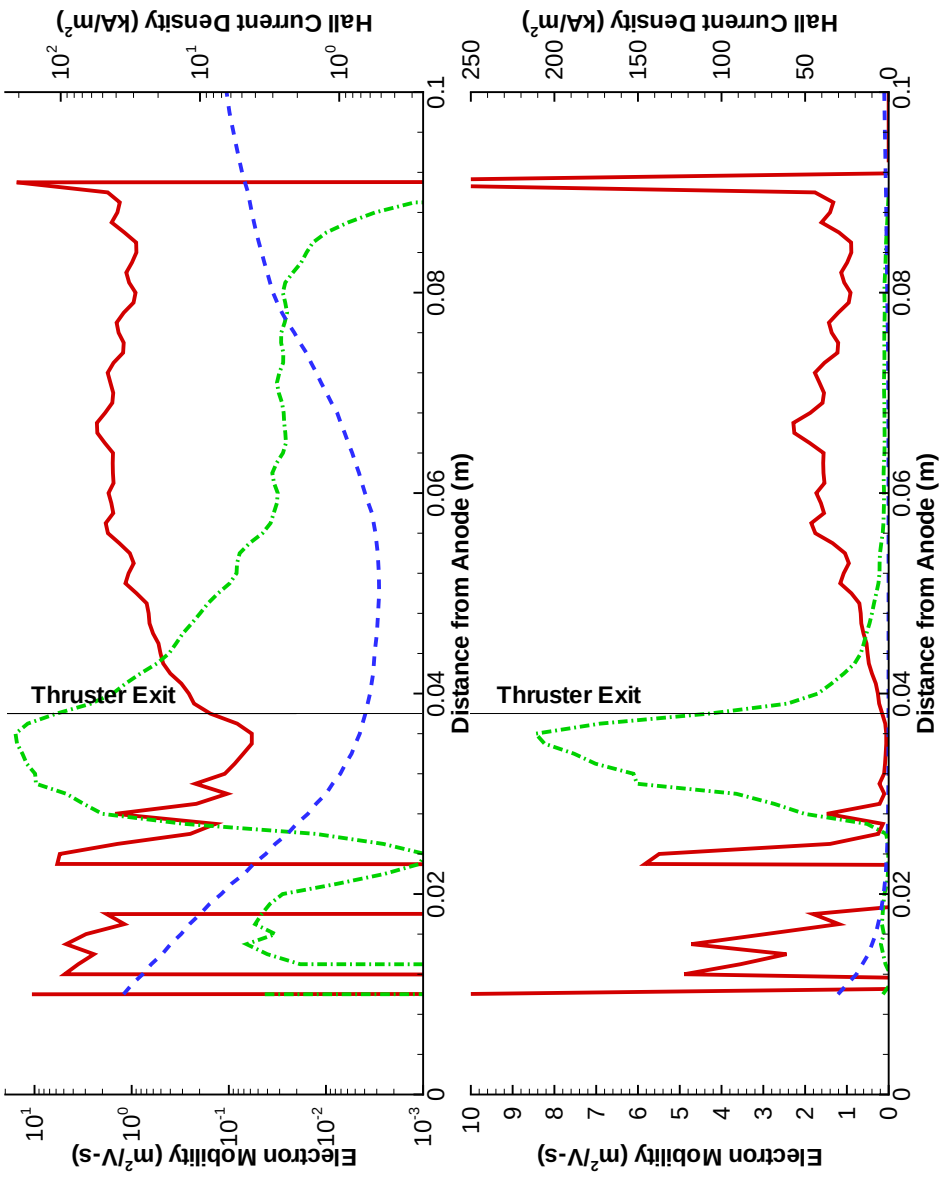


Figure 5.11: UM/AFRL P5 Plasma Properties – 78.5 mm from centerline (Solid line - Semi-Empirical Mobility, Dashed line – Classical mobility, Dash-Dotted line - Hall current density)

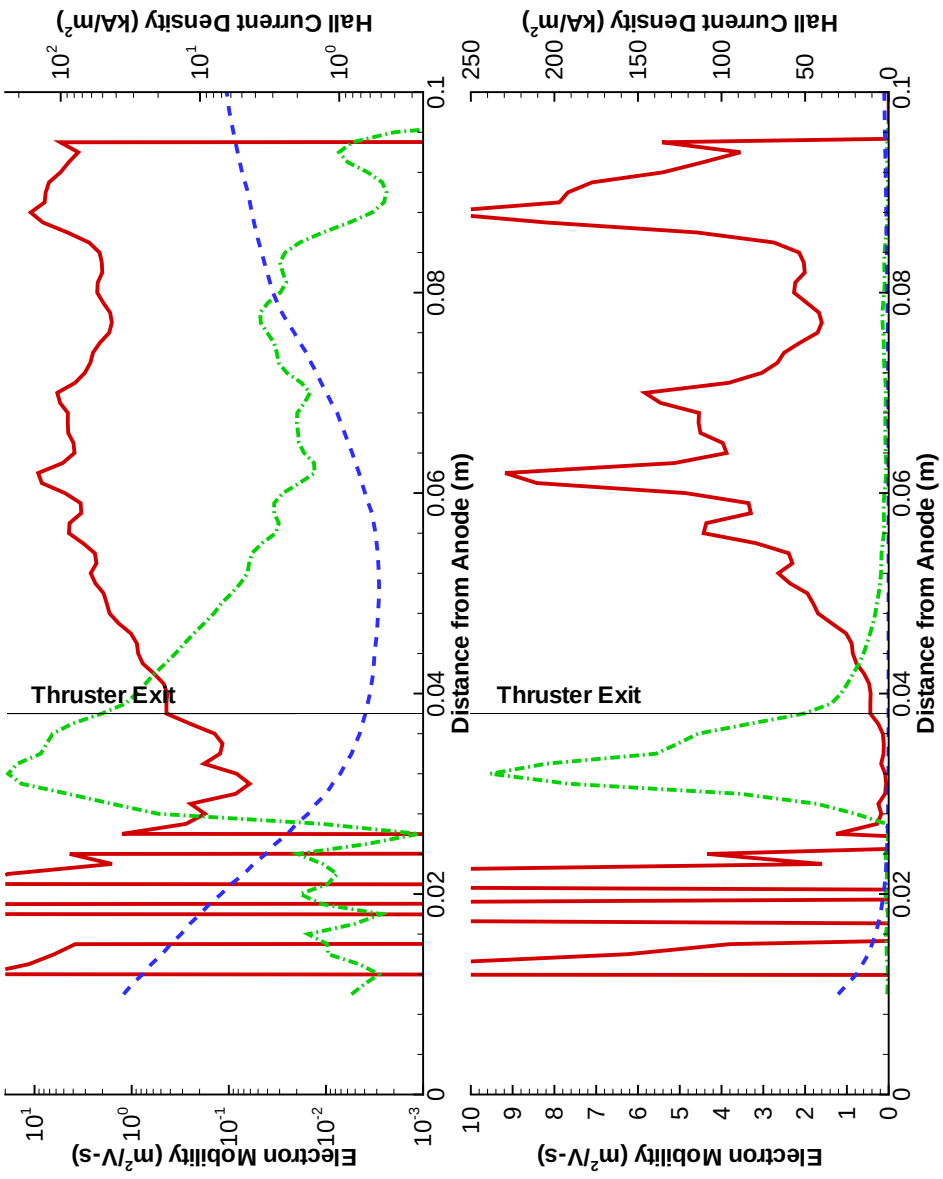


Figure 5.12: UM/AFRL P5 Plasma Properties – 83.5 mm from centerline (Solid line - Semi-Empirical Mobility, Dashed line – Classical mobility, Dash-Dotted line - Hall current density)

10 mm of the anode, so an estimated mobility is used in this region which provides good agreement with experimental potential data. The best fit curve is implemented in the code by considering the simulation to have a constant mobility in the radial direction. Electron energy loss coefficients of $\alpha = 0.20$ and $\varepsilon = 20\ eV$ are used in this simulation.

Performance data are presented in Table 5.4. All of the results, except for the discharge current are predicted to within 3% of measured values. This correlation is perhaps not surprising, since the semi-empirical mobility (upon which the best-fit mobility is based) was constructed to reproduce a similar potential profile and ion density distribution to that found experimentally near the middle of the acceleration channel.

Table 5.4: UM/AFRL P5 Xe Performance Data

	Experimental	Best Fit
Discharge Voltage (V)	300	275
Discharge Current (A)	10.0	11.3
Thrust (mN)	180.0	179.3
Anode mass flow rate xenon (mg/s)	10.2	10.2
I_{sp} (s)	1744	1792
Efficiency (%)	51.0	50.5
Power (W)	3000	3119

A comparison between the simulation and experimental centerline potential is presented in Fig. 5.14. It is clear that the entire acceleration channel potential gradient has been captured with very high fidelity. Besides the initial offset of the experimental and simulation potential at the anode, serious discrepancies do not arise until the thruster exit plane. At this point, the curvature of the experimental potential gradient changes sign as the ions begin to leave the acceleration zone.

The 2-D potential profiles from the best fit simulation and experimental data

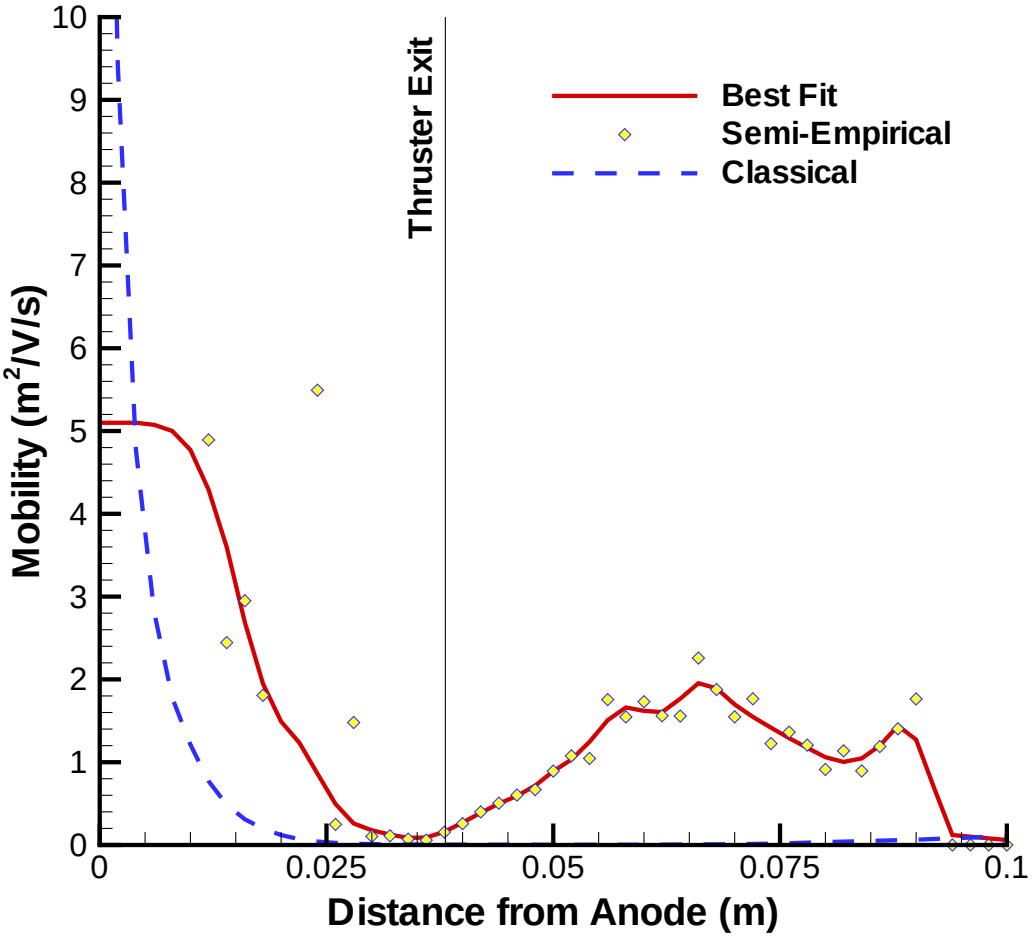


Figure 5.13: UM/AFRL P5 Semi-Empirical Electron Mobility – 78.5 mm from centerline (Solid line - Semi-Empirical Mobility, Dashed line – Classical mobility)

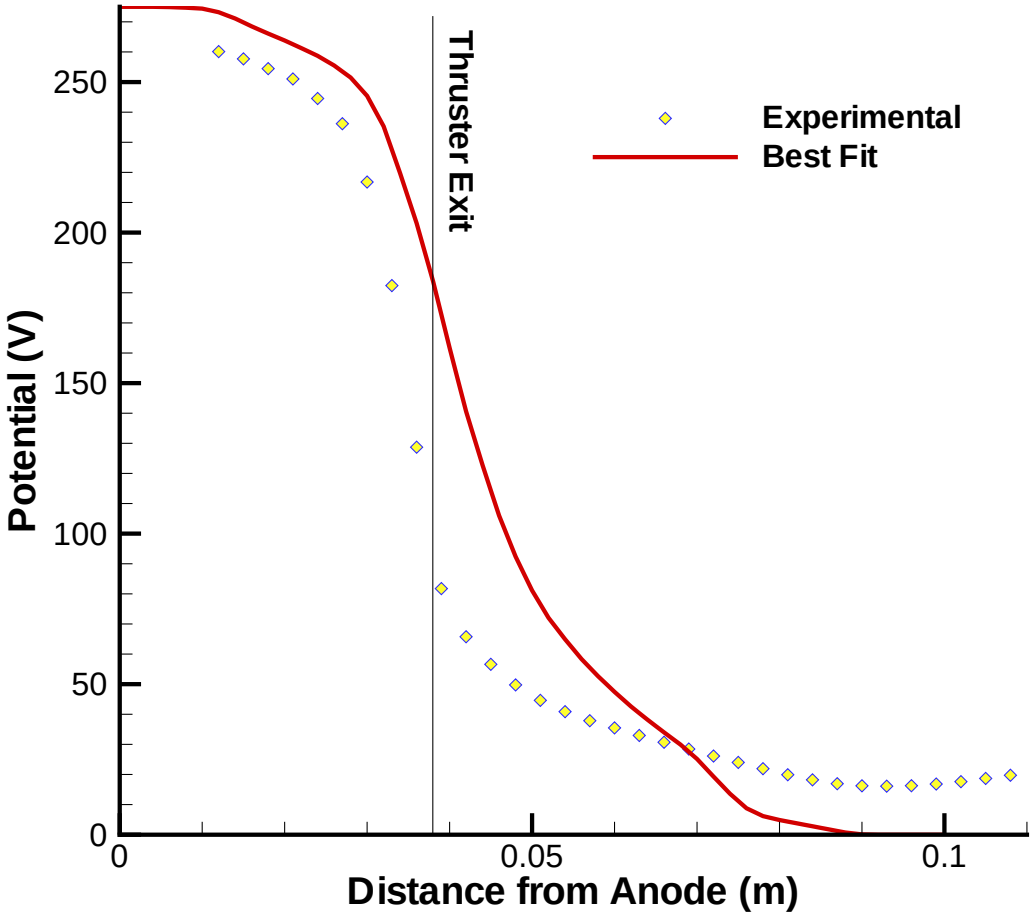


Figure 5.14: UM/AFRL P5 Centerline Plasma Potential

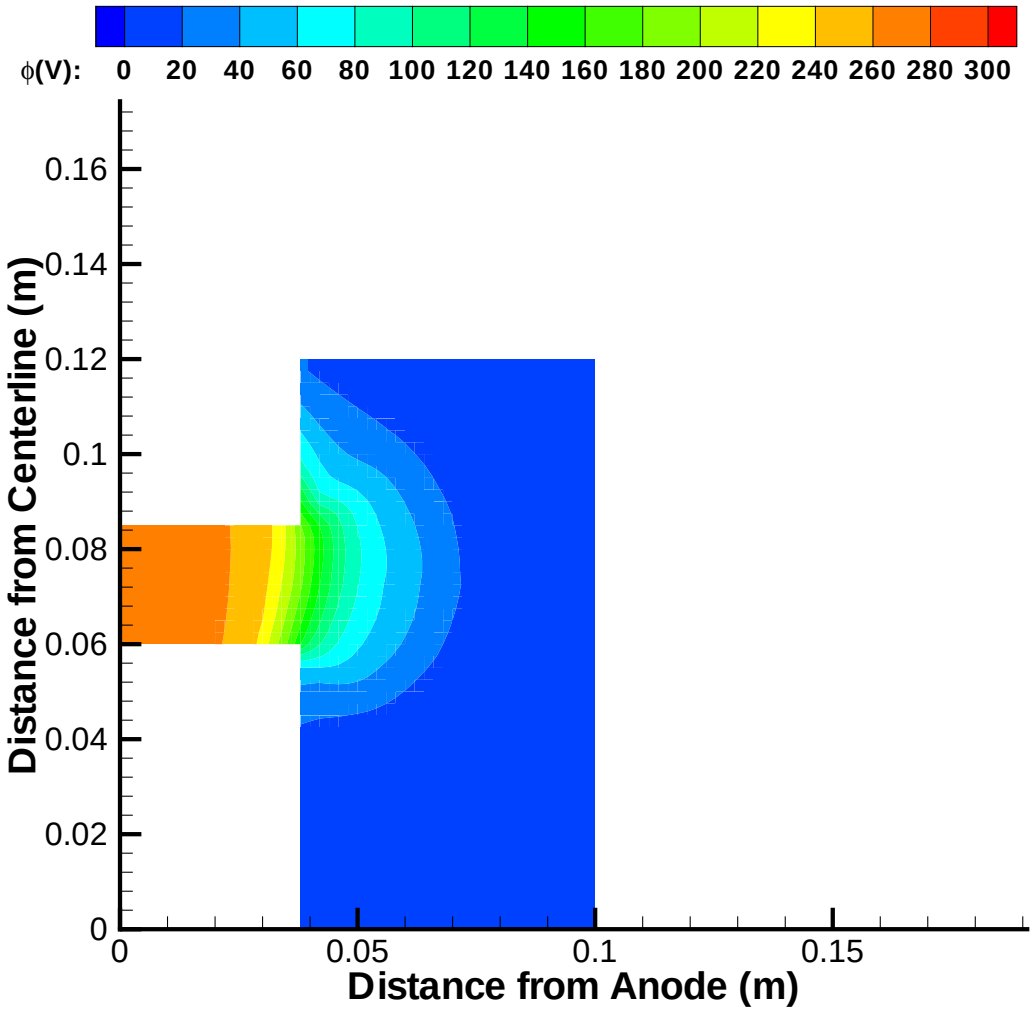


Figure 5.15: UM/AFRL P5 Computational Mean Potential

are presented in Fig. 5.15 and Fig. 5.16, respectively. The potential "jet" structure observed experimentally has been reproduced successfully with a full 2-D fluid Hall thruster model by *Keidar et al.* (2004). The inability of the simulation to reproduce this feature reflects the quasi 1-D nature of the electrostatic solver.

A comparison of the model and experimental centerline electron temperature is presented in Fig. 5.17. The model clearly does not show very strong agreement with the experimental data. In this case, not only is the magnitude of the peak

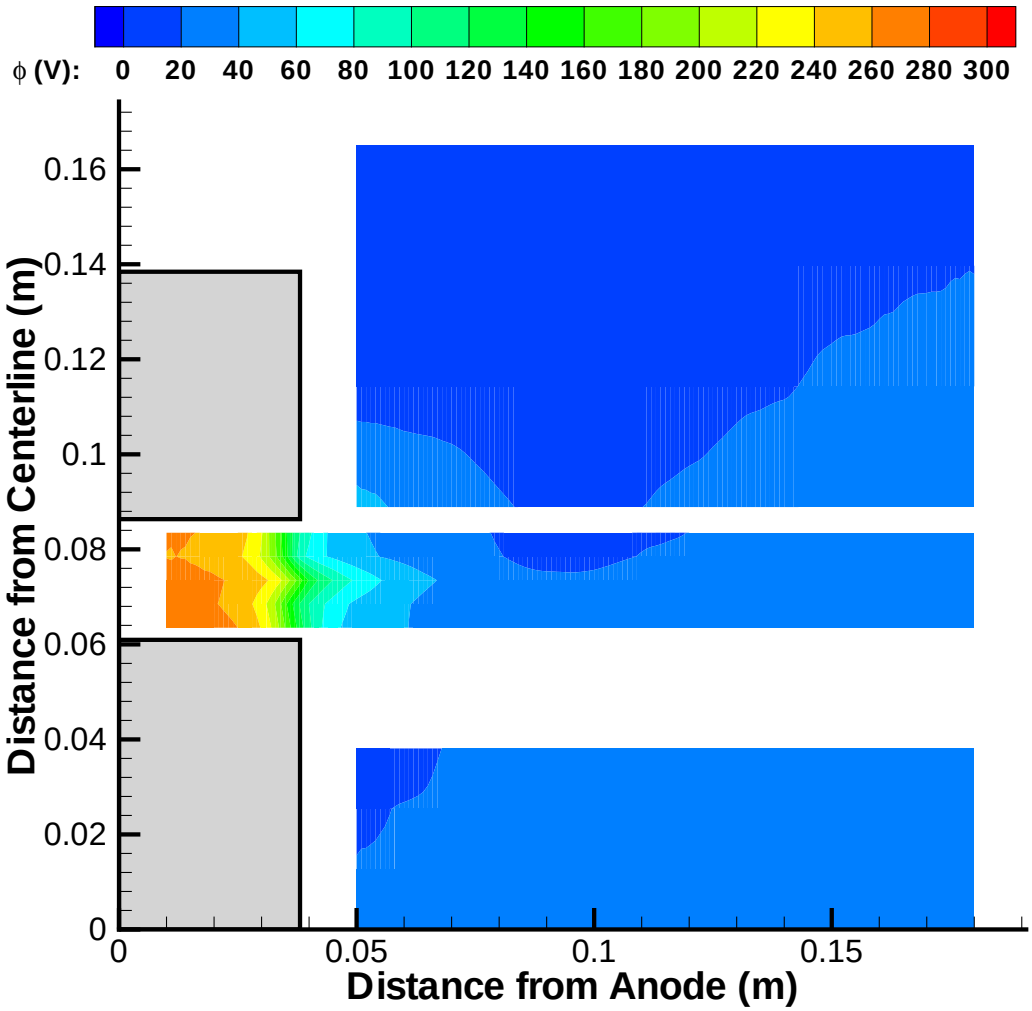


Figure 5.16: UM/AFRL P5 Experimental Potential

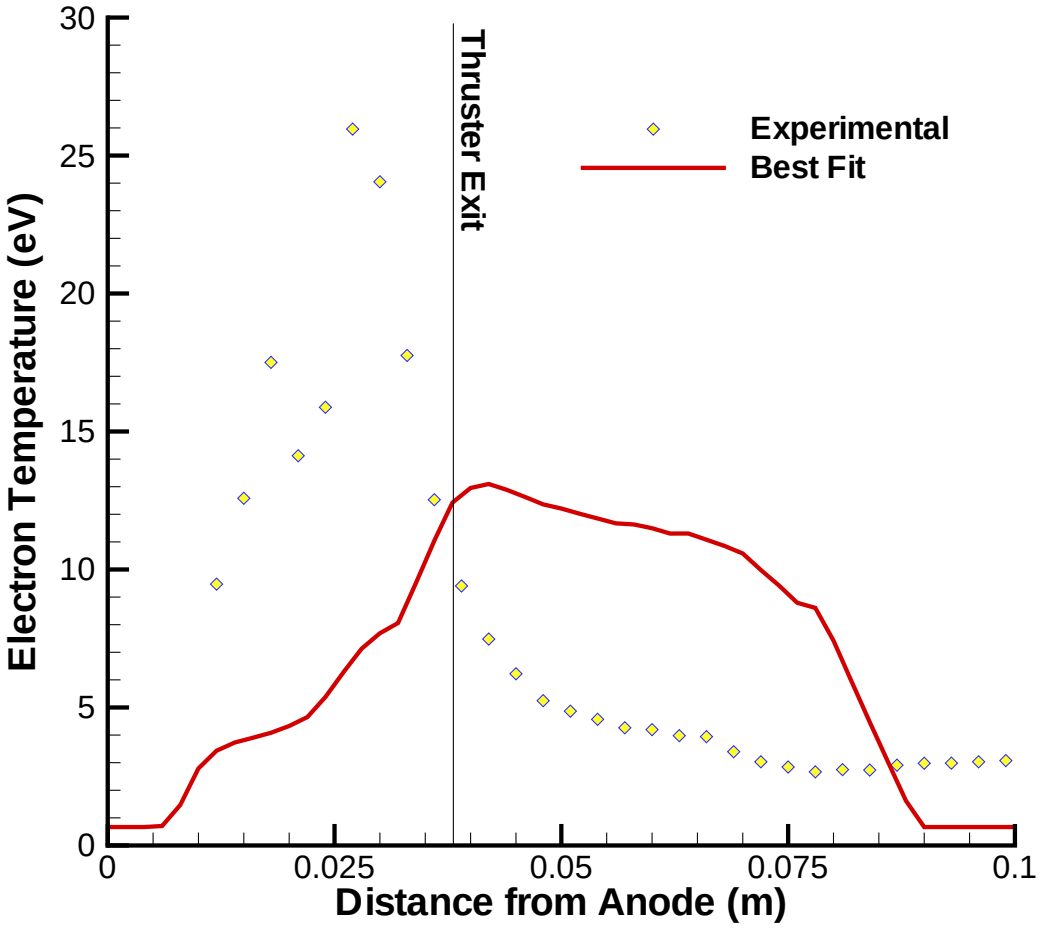


Figure 5.17: UM/AFRL P5 Centerline Electron Temperature

temperature off by a factor of two, but the temperature profile in the near-field is almost as high as the peak temperature and exhibits a definite negative curvature (indicating some energy source in the near field) instead of the positive curvature (no energy source) associated with measured electron electron temperature profiles outside the thruster.

The extreme magnitude of the "breathing-mode" oscillations (see current trace in Fig. 5.18) is the likely cause of the elevated near-field temperature profile. An

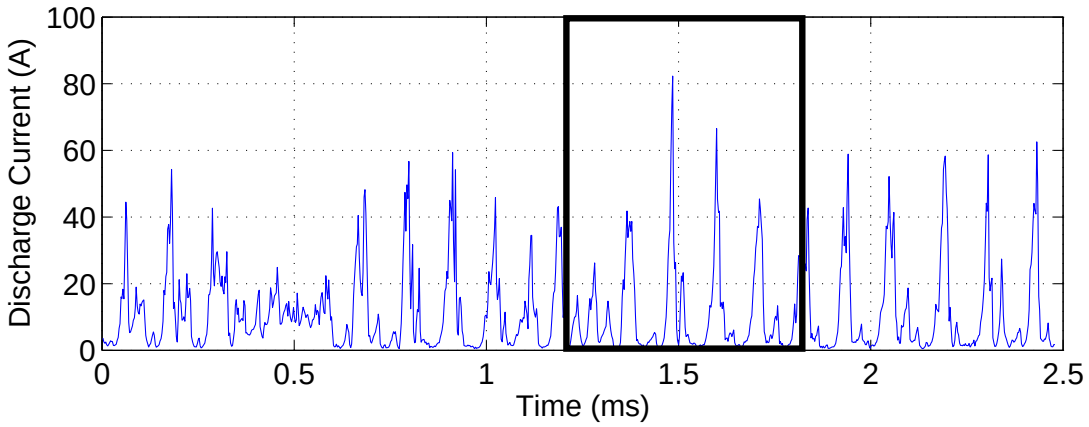


Figure 5.18: UM/AFRL P5 Computational Discharge Current – The magnitude of the discharge current oscillation at a discharge voltage of 500 V is typically less than 10% of discharge current. (Dark box represent interval over which data in Fig. 5.19 are sampled.)

illustration of this mechanism is shown in Fig. 5.19. The breathing mode oscillations (average frequency 8.5 kHz) are most visible in the plasma density trace (middle frame) as the plasma density can be seen to build in magnitude at about 2 cm from the anode then suddenly accelerate to the right (out of the thruster). The movement of the potential gradient from deep inside the channel to far outside the channel is very clear from the potential trace. Since there can exist a very steep negative potential gradient (corresponding to a strong positive electric field) in the thruster channel, then ohmic heating is a real concern in this region. As the electron temperature trace (right frame) makes clear, the result of the high ohmic heating associated with these oscillations is a high instantaneous electron temperature which moves around in the near-field of the thruster. (Unless noted as instantaneous energies or temperatures, all simulation energy and temperature results presented in this paper represent density-averaged quantities. Density-averaging better represents the actual energy fluxes than simple time-averaging.)

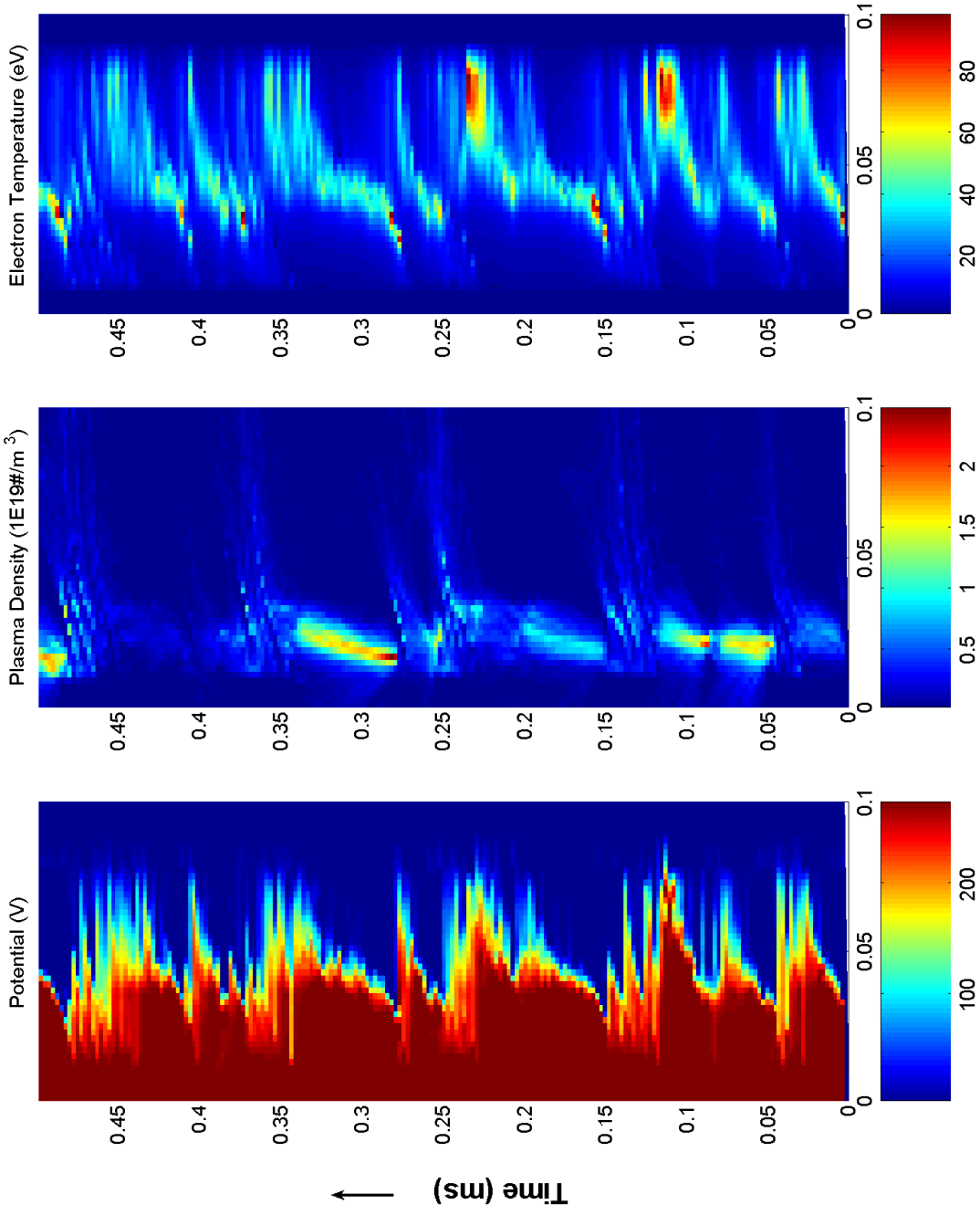


Figure 5.19: UM/AFRL P5 Computational Centerline Properties – *Horizontal axis represents distance from anode in meters*

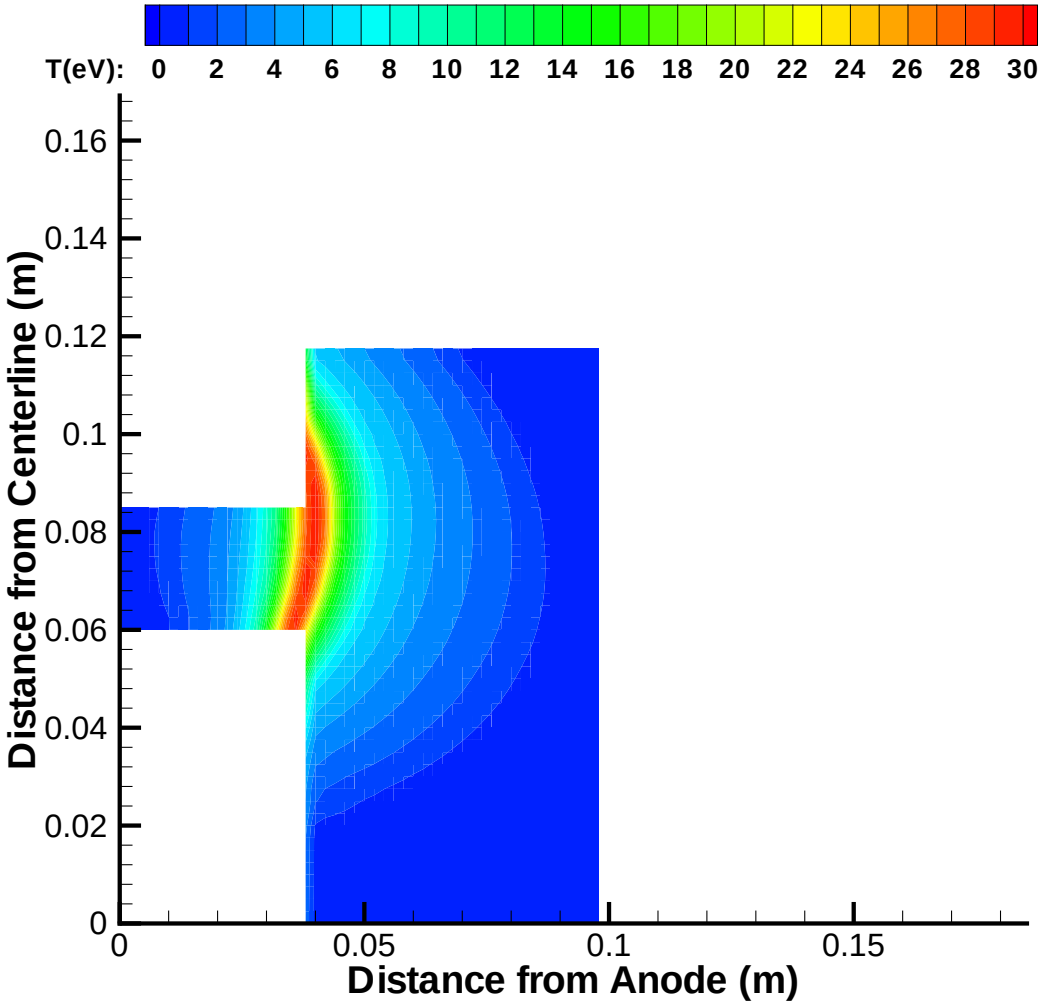


Figure 5.20: UM/AFRL P5 Instantaneous Plasma Temperature

The strong oscillatory physical behavior also explains why instantaneous simulation results do exist (Fig. 5.20) which can mimic the experimental results (Fig. 5.21) while averaged results are clearly different. These characteristics add yet another metric (correct time-dependent discharge current profile) upon which to evaluate and validate computational simulations.

Finally, 2-D computational and experimental plasma densities are presented in Fig. 5.22 and Fig. 5.23, respectively. The spatial configuration of the computational

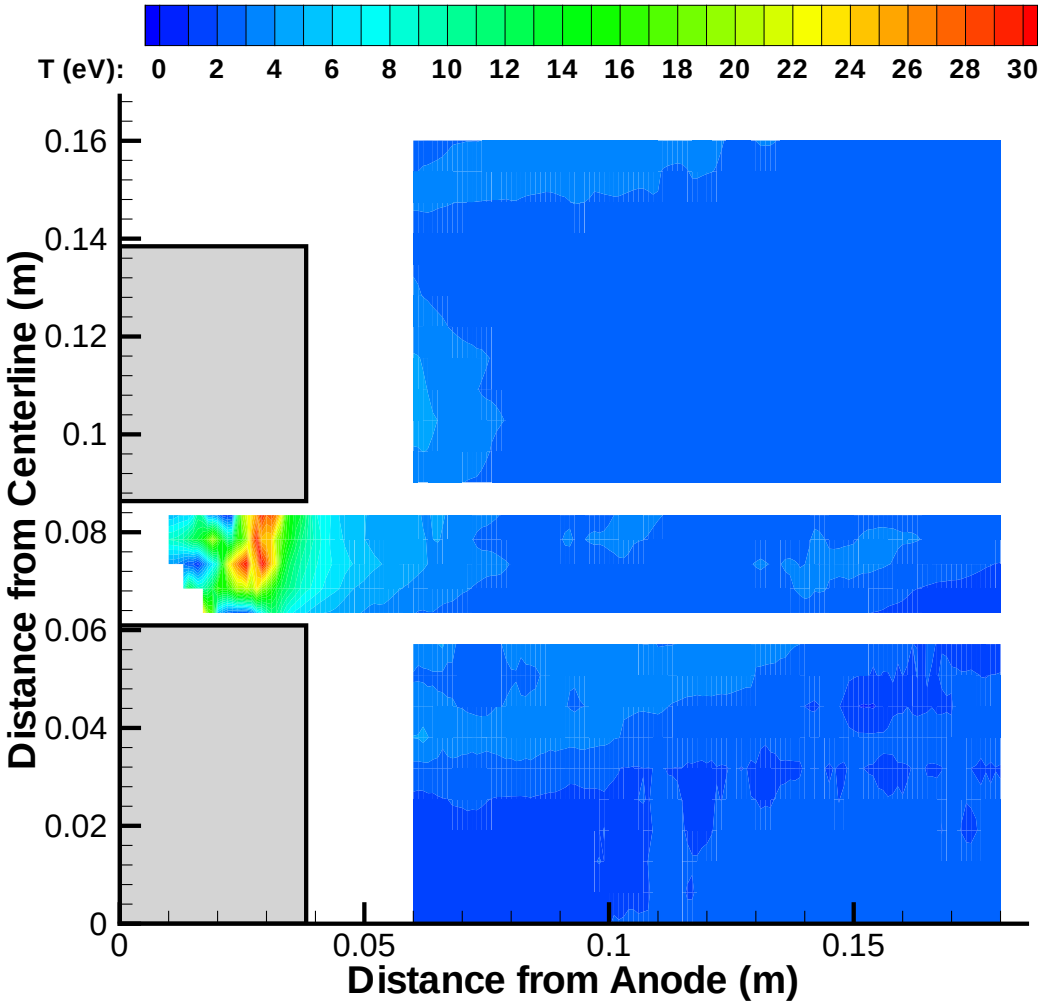


Figure 5.21: UM/AFRL P5 Experimental Plasma Temperature

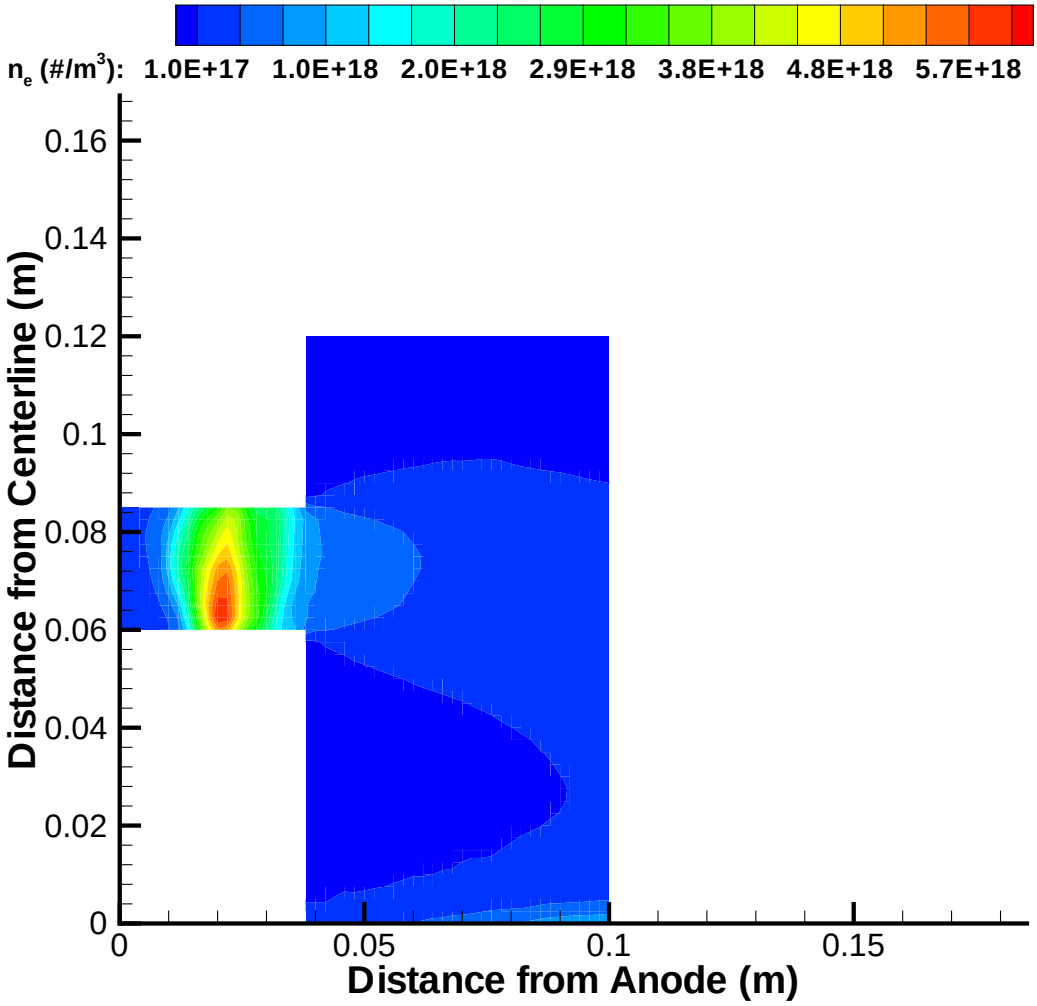


Figure 5.22: UM/AFRL P5 Computational Mean Plasma Density

plasma density depends strongly on the local electron temperature, which is constant along the magnetic field lines shown in Fig. 5.24. Again, the radial asymmetry of the experimental dataset is not well represented by the quasi-1D physical models in the simulation. The differences in the peak plasma densities are about a factor of two, just within the error of the experimental dataset.

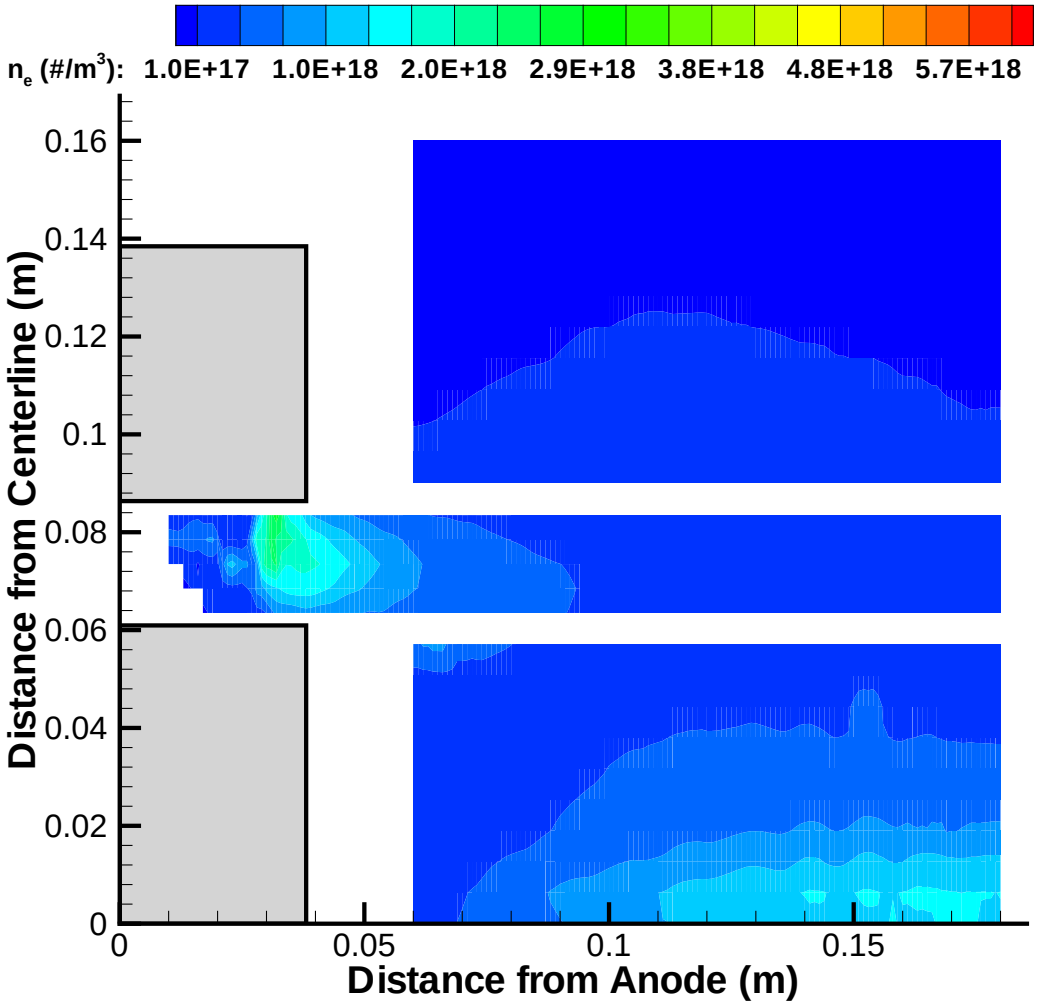


Figure 5.23: UM/AFRL P5 Experimental Plasma Density

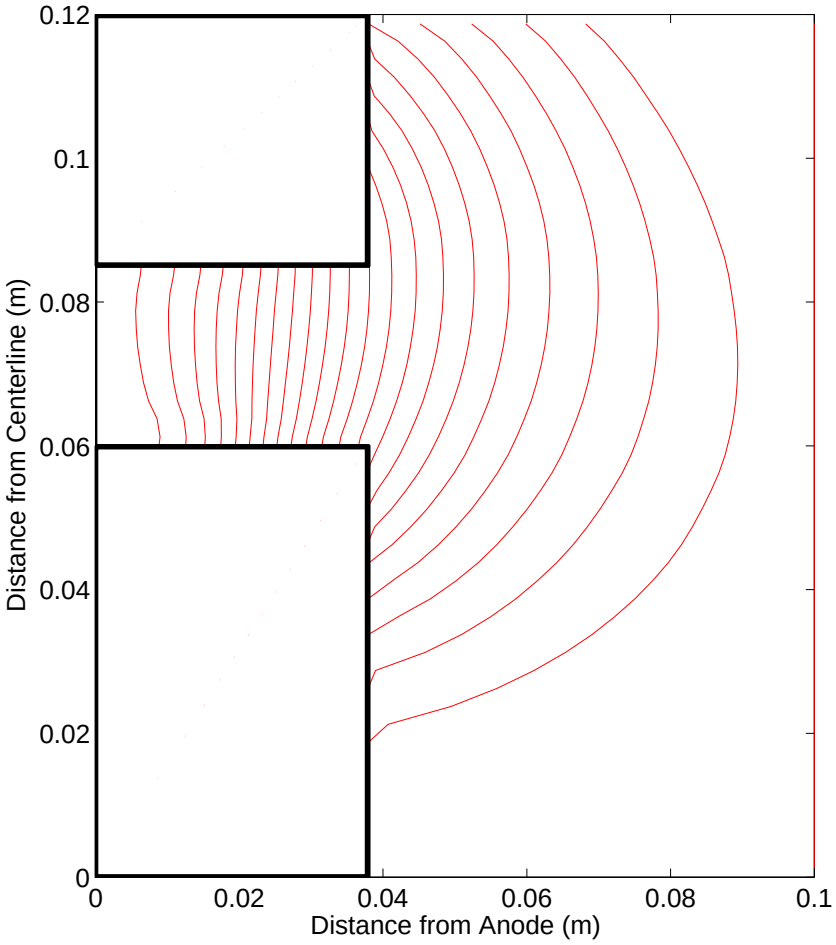


Figure 5.24: UM/AFRL P5 Magnetic Field Grid

5.1.2.5 Discussion

Existing single and mixed mobility models demonstrate that Hall thruster simulations are quite robust and can produce results for even physically unreasonable electron mobility profiles. Unfortunately, since such simulations are so robust, it is difficult to tell whether or not the correct mobility model has been selected. Of the fully computational model electron mobility models presented in this thesis, the mixed mobility models offer the most flexibility and thus are able to produce the best overall simulation performance.

Going one step further and calculating the electron mobility based on experimental datasets leads to a semi-empirical mobility profile which can be used to construct very high fidelity mobility curve fits. A simple curve fit to a semi-empirical mobility based on an assumed electron current density profile performed extremely well in replicating the experimental centerline potential profile. Although certain 2D details were lost, the simulated plasma density was also correct to within the experimental uncertainty. The greatest weakness of this 1D mobility curve fit was in the electron temperature, which was off by a factor of two in magnitude and had a completely different near-field structure; however, all the electron temperatures observed from this code have shown extremely weak correlation with experimental data.

5.1.3 Semi-Empirical Self-Field Electron Mobility

The semi-empirical mobilities proposed in Sec. 5.1.2.4 are constructed using the contributions of both experimental data (through the plasma potential, plasma density, and electron temperature) and modeling assumptions (through the electron current density). Since different electron current density profiles certainly have the potential to radically alter the resulting semi-empirical mobilities, it is prudent to

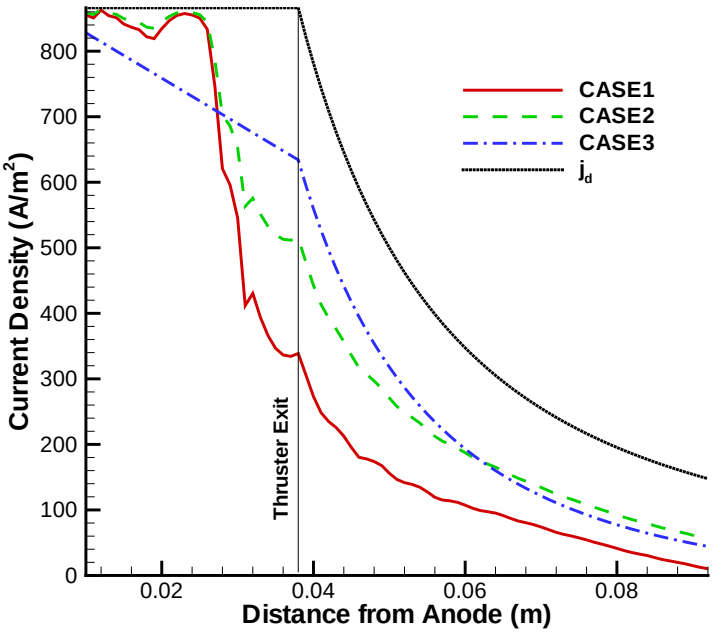


Figure 5.25: Test Electron Current Densities

establish the sensitivity of this relationship in at least an ad hoc manner before trying to fit theoretically based computational mobility models to their semi-empirical counterparts. To this end, two additional electron current density profiles, in addition to CASE1 (developed in Sec. 5.1.2.4), are constructed to demonstrate the conditions of CASE2 (high discharge current – 40% of discharge current density) and CASE3 (medium discharge current – 30% of discharge current density – with a linear electron current growth rate throughout the simulation). The actual electron current densities are presented in Fig. 5.25 and the resulting semi-empirical electron mobilities are presented in Fig. 5.26.

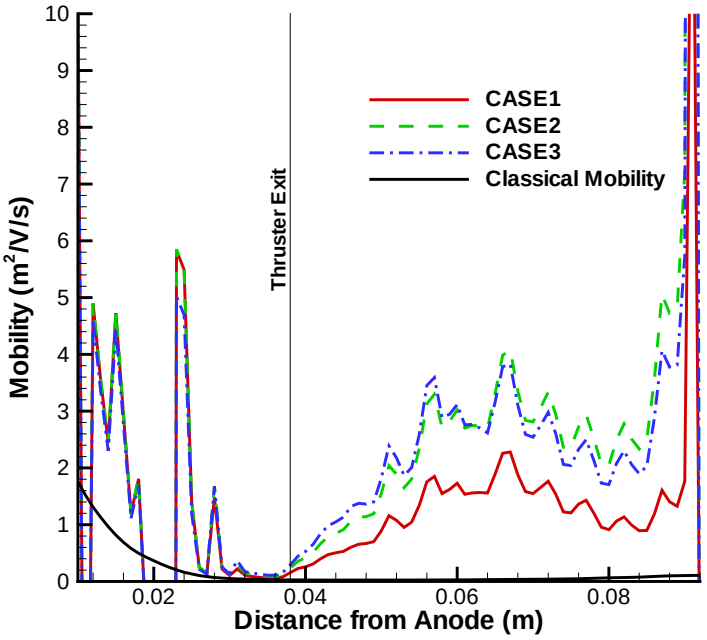


Figure 5.26: Semi-Empirical Electron Mobility

5.1.3.1 Magnetic Self-Field

The question of whether the plasma dynamics are sufficiently energetic and directed to induce a self-magnetic field is a question of quite some contention in the Hall thruster community. Direct measurement of the radial magnetic field (at 73.7 mm from thruster centerline) in the UM/AFRL P5 thruster operating at 3 kW on xenon has been performed by *Peterson et al.* (2001) and their study is used as the reference experimental plasma (self-field) configuration. The baseline vacuum field (at 78.5 mm from thruster centerline) is from *Haas* (2001). Both radial magnetic field configurations are presented in Fig. 5.27.

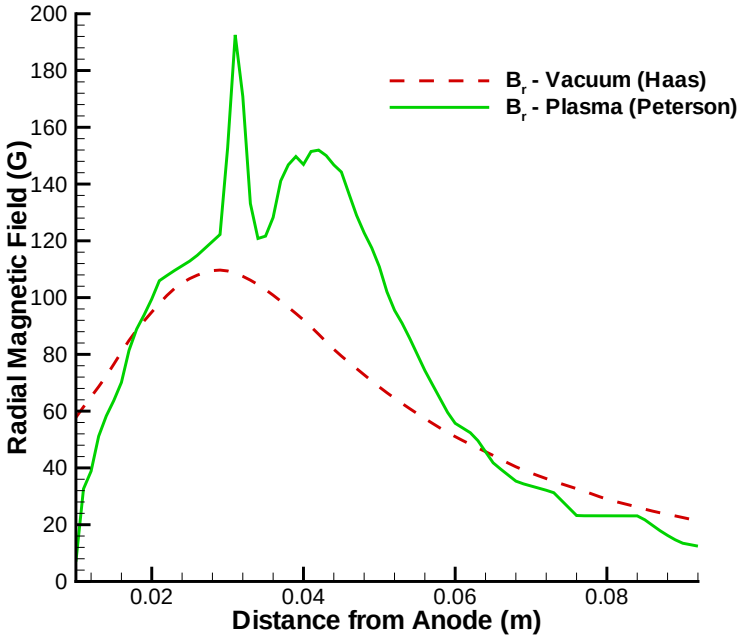


Figure 5.27: UM/AFRL P5 Radial Magnetic Field

5.1.3.2 Thermalized Potential

Experimental data from *Haas* (2001) is used to calculate the thermalized potential according to the following formula:

$$\phi^*(\lambda) = \phi - \frac{k_B T_e}{e} ln(n_e) \tag{5.3}$$

The thermalized potential for the UM/AFRL P5 operating at 3.0 kW on xenon is shown in Fig. 5.28. Note that contours of constant thermalized potential represent magnetic field lines. The vacuum magnetic field grid is the red overlay. From this data, it is possible to make out the Hall current region (dark blue) and the "X" shape characteristic (in green) which indicates that negative B_r values exist further downstream in the anode region of the thruster. It is important to note that this

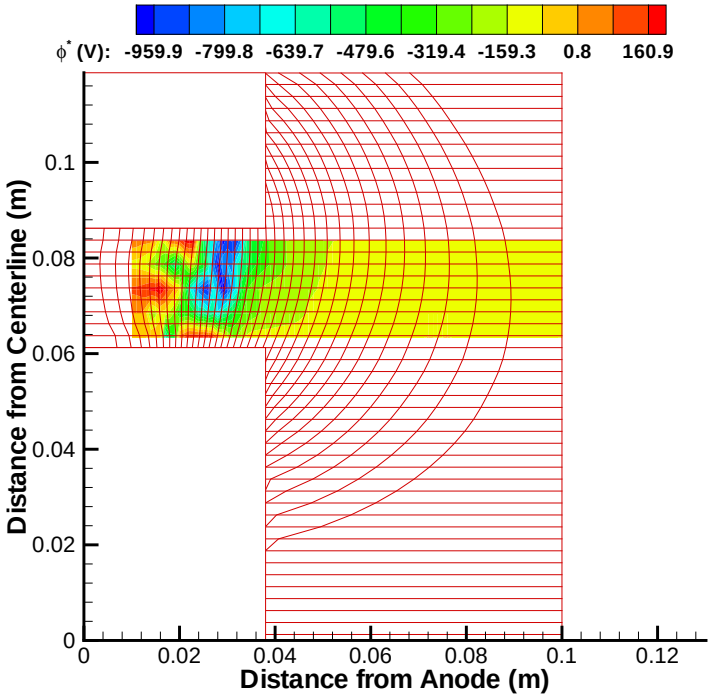


Figure 5.28: UM/AFRL P5 Thermalized Potential

inferred illustration of the magnetic field line is constructed with completely different diagnostics than the direct B-field measurement technique of *Peterson et al.* (2001).

5.1.3.3 Mobility Results

Now it is possible to construct two different mobility datasets presenting the contribution of classical and Bohm mobility (with constant coefficient of $0.005 \cdot B_r$). The profiles in Fig. 5.29 are based on the vacuum B_r and those in Fig. 5.30 are based on the plasma B_r. Magnified versions of these datasets are presented in Fig. 5.31 and Fig. 5.32

5.1.3.4 Discussion

The magnetic self-field, which has now been documented by two different experimental techniques in the UM/AFRL P5 Hall thruster, provides some clue as to

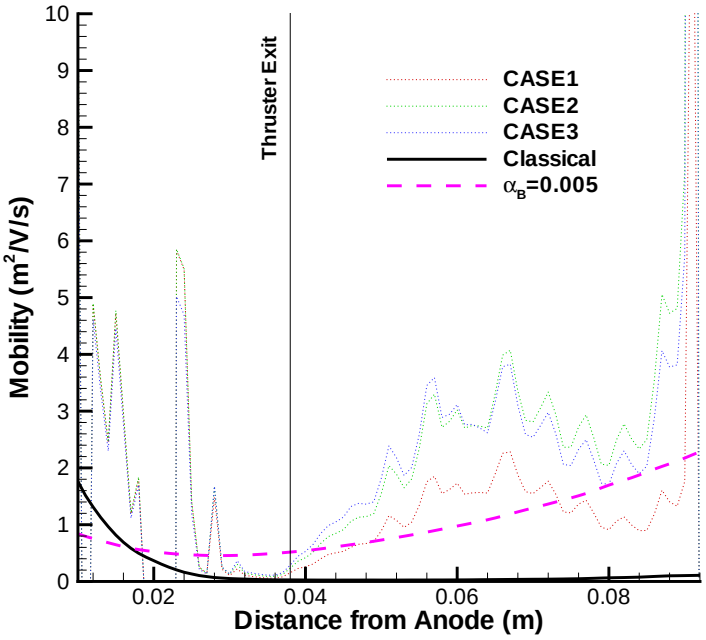


Figure 5.29: UM/AFRL P5 Semi-Empirical Mobility (Vacuum B_r)

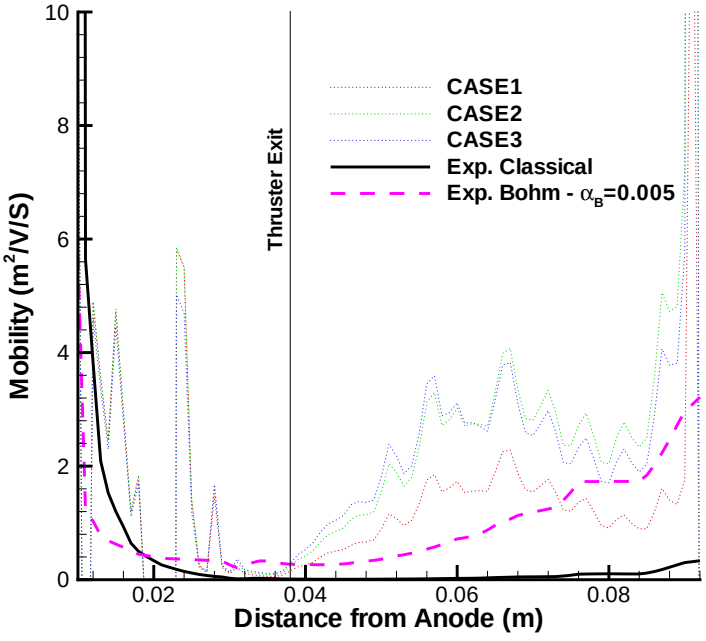


Figure 5.30: UM/AFRL P5 Semi-Empirical Mobility (Plasma B_r)

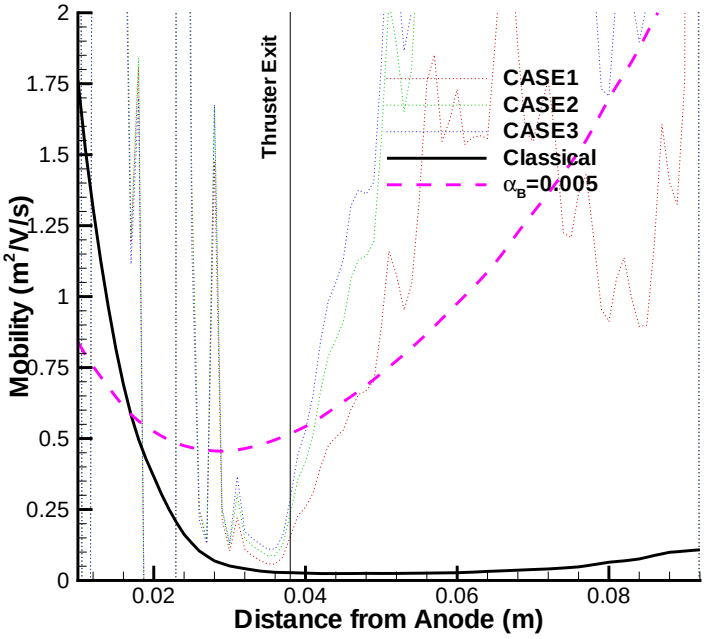


Figure 5.31: UM/AFRL P5 Semi-Empirical Mobility (Vacuum B_r)

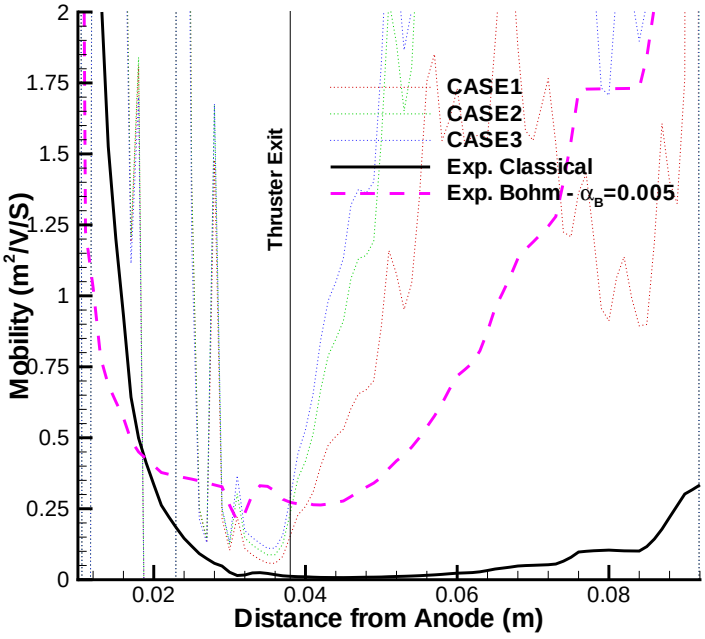


Figure 5.32: UM/AFRL P5 Semi-Empirical Mobility (Plasma B_r)

how to construct a theoretically sound model for the anomalous mobility in a Hall thruster.

Based on work with the semi-empirical mobility model in this chapter, it is clear that a sufficiently high mobility is necessary in the anode region to ensure that the potential gradient stays low in this region. On the other hand, it can be observed in virtually all of the semi-empirical profiles that the electron mobility drops to near classical values in regions with a high Hall current density. Finally, the mobility curves in the near field definitely share a 1/B Bohm type slope; however, the positive offset necessary for a reasonable curve (the minimum value of 1/B) leads to an unreasonably high mobility near the thruster exit.

Successful mixed mobility models couple a wall-collision mobility model inside the acceleration channel with a Bohm diffusion mobility model outside the channel; however, they suffer from problems when the two curves must be joined near the thruster exit. This is where the plasma magnetic field appears to play a significant role. It not only provides a much better mating condition near the thruster exit (by locating a sharp magnetic field peak at the edge of the Hall current), but it also lowers the magnetic field near the anode region of the thruster, permitting high mobility in this region without the need for additional near-wall conductivity terms.

Although the results presented here are preliminary, they offer a potential combination of useful characteristics to construct a unified Hall thruster mobility model.

5.2 NASA-173Mv1 Hall Thruster

A mixed mobility model (similar to the Mixed Outer model) with $\alpha = 0.125$ and $\alpha_B = 0.060$ and a wall-energy loss coefficients of $\alpha = 0.125$ and $\varepsilon = 15$ is used to simulate the NASA-173Mv1 Hall thruster operating on krypton. The performance

characteristics of this simulation are provided in Table 5.5. Although the thrust performance of this simulation is impressive, the elevated discharge current belies significant problems. Since the thrust is produced by the heavy particles only, then it can be postulated that at least some portion of the excess 3.52 A of discharge current in the simulation is electron current. From the work presented in this thesis, it is clear that an incorrect electron current indicates fundamental errors in the electron mobility profile. Unfortunately, internal and/or near-field data for this thruster configuration is not yet available for validation purposes. Plasma potential data is presented in Fig. 5.33 and centerline plasma properties are presented in Fig. 5.34. RPA and Faraday probe data indicate that the plume divergence of this thruster operating condition is over 60 degrees while simulation results indicate a much lower plume divergence angle. Future refinement of the mobility model should therefore seek to move a larger fraction of the potential gradient outside the thruster (by raising the internal mobility relative to the mobility in the near-field) to replicate the larger plume divergence of the experimental dataset. This krypton simulation at high operating voltage suffers from the same problems as the UM/AFRL P5 xenon simulations at lower voltage. This finding emphasizes the need for improved fundamental understanding of electron mobility in all Hall thrusters.

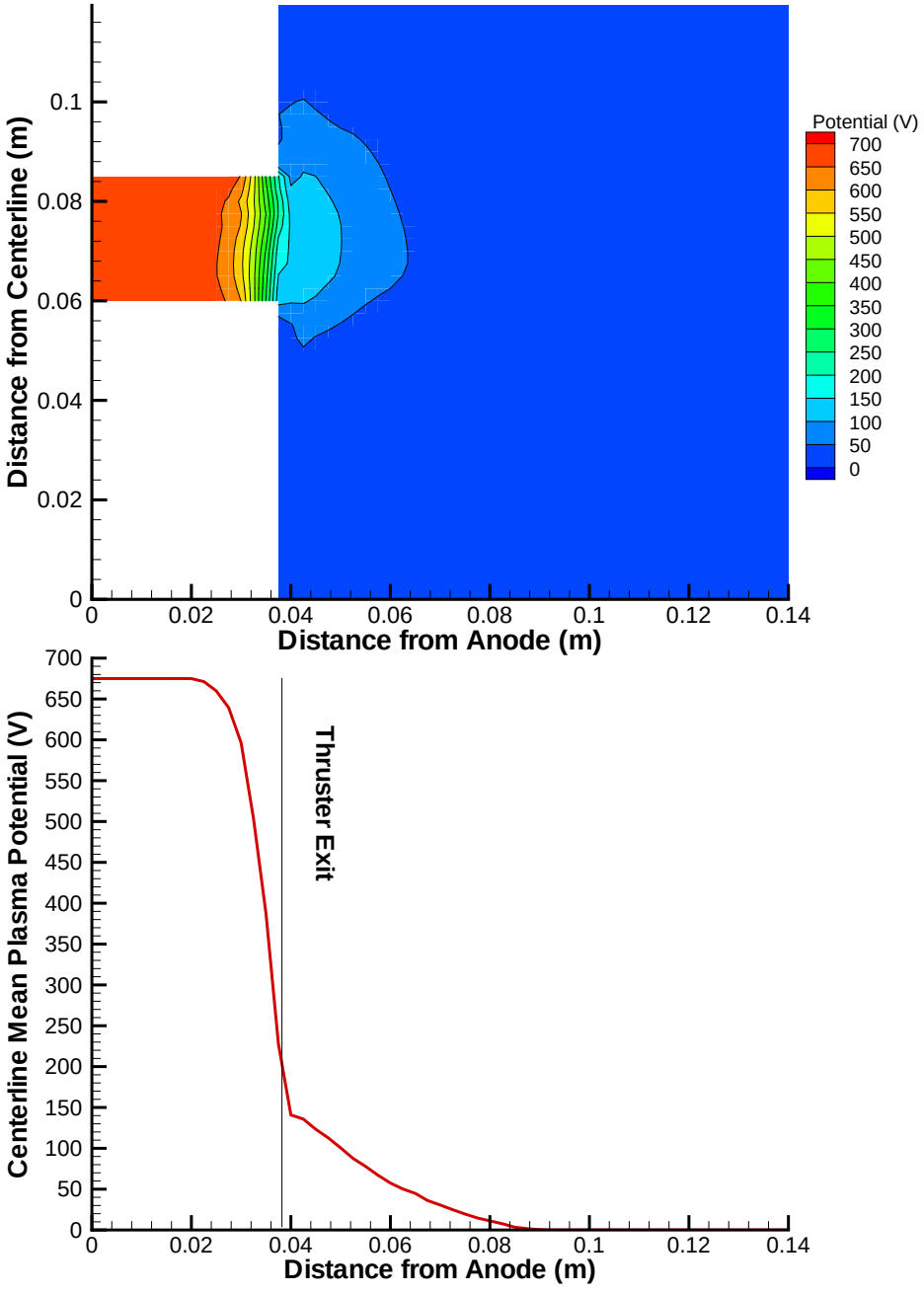


Figure 5.33: NASA-173Mv1 Kr Computational – Plasma Potential

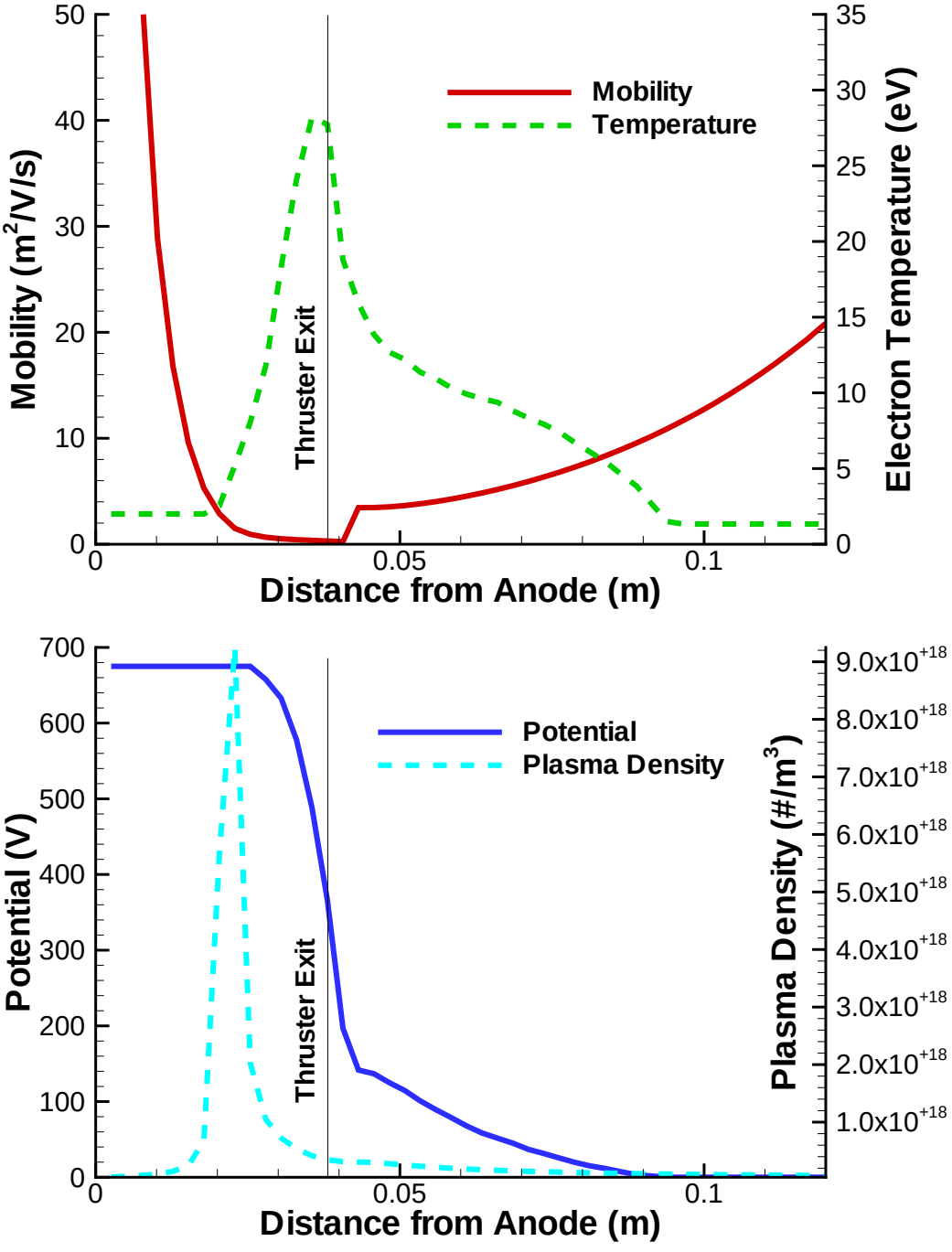


Figure 5.34: NASA-173Mv1 Kr Computational – Plasma Properties

Table 5.5: NASA-173Mv1 Kr Performance[a]

	Experimental	Computational
Discharge Voltage (V)	700	675
Discharge Current (A)	9.75	13.27
Thrust (mN)	225	232
Anode mass flow rate krypton (mg/s)	7.26	7.26
I_{sp} (s)	3160	3254
Efficiency (%)	51.1	41.3
Power (W)	6825	8957

[a]Cathode Mass Flow Rate – 0.73 mg/s krypton, Background Pressure – $4.84 \cdot 10^{-6}$ torr

CHAPTER VI

Summary and Future Work

This thesis presents a detailed study of the numerical behavior and mobility modeling in a 2-D axisymmetric hybrid PIC-MCC Hall thruster code. This chapter includes a brief summary of the most important lessons learned from this research and presents a number of possible directions for future research on this topic.

6.1 Conclusions

As a study of numerical behavior, this work catalogues the sensitivity of the code to both numerical parameters and physical parameters. Besides demonstrating that the code must satisfy typical CFL number constraints based on time step and grid size, this research also demonstrated that certain numerical choices, namely the placement of the upstream and downstream boundaries of the active simulation region (where the electrostatic potential and the electron energy are solved self-consistently), can have a significant impact on the physics of the simulation. This effect occurs because the definition of an active simulation region does not account for the possibility of a spatially diffuse ionization zone which spans almost the entire length of the acceleration channel in certain thruster simulations. In practice, judicious modeling decisions are necessary to minimize the impact of these numerical

choices.

The ionization algorithm in this code is based on a Monte Carlo Collision algorithm which performs direct ionization of neutral macroparticles into ion macroparticles. A collision multiplier technique was used to ensure that enough ion macroparticles exist to ensure satisfactory particle statistics in the simulation. Study of the time-dependent behavior of the code with different numbers of macroparticles uncovered a weakness in this approach to neutral ionization when it was observed that strong plasma oscillations in the 5–30 kHz range were being damped strongly by the ionization algorithm under certain circumstances.

The role of the total electron energy loss frequency in this simulation is to account for the loss of energy in the plasma through both wall-collision and inelastic collision losses. The components of this term were studied individually and it was demonstrated that certain coefficient choices for the wall-collision term do not dissipate enough energy and lead to excessive mean electron temperatures. The inelastic collision loss frequencies used by the code were demonstrated to be in a relatively stable regime where small perturbations in the electron energy inelastic collision rate result in only small changes in thruster performance. Finally, it was demonstrated that excessively high electron energies can overwhelm phenomena dependent on finite rate ionization dynamics like the breathing mode oscillations.

As a study of mobility modeling, this thesis evaluated the performance of existing computational models for the electron mobility and developed a semi-empirical model for the electron mobility based on experimental data. A 1D mobility profile obtained from the semi-empirical model provided a very promising validation of the code for the UM/AFRL P5 Hall thruster.

Finally, the semi-empirical model was used with a non-vacuum condition mag-

netic field to uncover corrections to the electron mobility due to self-field effects. These corrections enabled the formulation of a more accurate computational mobility model which incorporated established Bohm diffusion theory in the near-field and classical diffusion theory (across magnetic field lines) inside the acceleration channel. As part of this analysis, the traditional modeling concept of the thermalized potential was used to provide concrete evidence that there is a substantial difference between the vacuum condition and non-vacuum condition magnetic field configurations. As a result, it is possible that the fundamental underpinnings of conventional electrostatic Hall thruster simulations need to be re-evaluated.

6.2 Future Work

While significant progress has been made in this study for the numerical simulation of Hall thrusters, the research has also indicated several areas where further work is required.

6.2.1 2-D Electromagnetic Solver

If indeed the plasma magnetic field configuration is not identical to the vacuum magnetic field configuration (as the thermalized potential indicates), then existing electrostatic potential solvers, including the one employed in this thesis, are fundamentally incapable of capturing all the essential physics of Hall thruster operation. An adaptive electrostatic solver, or, ideally, a 2-D electromagnetic solver capable of handling quasineutral plasmas, will be even more essential to the simulation of the next generation of high power, high current Hall thrusters.

6.2.2 Mobility Modeling

Although the self-field correction alone offers great promise in unifying the approach to mobility modeling, there are undoubtedly mechanisms and coefficients which will be necessary for higher fidelity Hall thruster simulation. The successful development of a realistic mobility model will be critical to the future success of any 2D electromagnetic solver.

6.2.3 Ionization Algorithm

Future work will necessarily include some numerical approach to better simulate the ionization process and the corresponding oscillatory behavior of the plasma. This can be approached through the development of a "fuzzy" collision multiplier controller which can maintain acceptable particle statistics while tolerating deviations from the target macroparticle count without drastically changing the collision multiplier. Alternatively, the use of a decoupled neutral ionization / ion creation algorithm as used by *Fife* (1998) can be implemented. This approach has its own statistical drawback in a large simulation but offers more direct user control over the ion macroparticle count in the simulation.

6.2.4 Cathode Modeling

In the existing code, the virtual cathode line, λ_c, should be fixed as close as possible to the effective cathode plane and an electron current density influx boundary condition of about 30% of the discharge current density should be imposed. Reducing the size of the active domain to extend only as far as the cathode plane should also reduce the computational cost of these simulations.

6.2.5 Sheath Modeling and Wall Effects

It is well established that dielectric sheaths are present in the low electron energy regions of the acceleration channel. The necessary stability criteria for such sheaths requires either finite electric fields or bulk ion motion at the sheath interface. Such boundary conditions must be accounted for by the potential solver (whether electrostatic or electromagnetic). Coupling the sheath and the active domain through a quasineutral presheath transition region seems a likely candidate for further study.

6.2.6 Neutral Collisions

In the regions of high neutral pressure near the anode face, significant neutral pressures (in excess of $6 \cdot 10^{-3}$ torr) are predicted by the code; however, at present no neutral-neutral collision model is contained in the code. The effect of collisions in cold-flow DSMC calculation of the acceleration channel indicate that the neutral-neutral collision processes leads to around twice the bulk neutral velocity at the channel exit when compared to simple ballistic neutral motion. Inclusion of neutral collisions will undoubtedly have a major effect on the ionization dynamics in the thruster since the bulk neutral velocity in the channel couples directly into the theoretical breathing mode oscillation frequency.

6.2.7 Charge-Exchange Collisions and Neutral Backpressure

As this code has matured and included significant portions of the very near field into the active simulation domain, the effect of neutral backpressure and charge exchange collisions is expected to be more and more significant, requiring the addition of further physical models to the code.

APPENDICES

APPENDIX A

Nomenclature

This section details the variables used throughout the thesis. When possible, the relevant mks units are provided. In addition, this section also contains the physical constants used throughout the thesis.

Variables

$\vec{B}$	$\cdots$	Magnetic Field $[T]$
B_r	$\cdots$	Radial Magnetic Field $[T]$
B_z	$\cdots$	Axial Magnetic Field $[T]$
n_e	$\cdots$	Electron Plasma Density $\left[\frac{\#}{m^3}\right]$
n_e^*	$\cdots$	Reference Electron Plasma Density $\left[\frac{\#}{m^3}\right]$
n_a	$\cdots$	Neutral Density $\left[\frac{\#}{m^3}\right]$
n_{Xe^+}	$\cdots$	Xe^+ Density $\left[\frac{\#}{m^3}\right]$
$n_{Xe^{++}}$	$\cdots$	Xe^{++} Density $\left[\frac{\#}{m^3}\right]$
r	$\cdots$	Distance from Centerline $[m]$
$\hat{r}$	$\cdots$	Radial Unit Vector
z	$\cdots$	Distance from Anode $[m]$
$\hat{z}$	$\cdots$	Axial Unit Vector
λ	$\cdots$	Magnetic Field Streamfunction $[T \cdot m^2]$
$\hat{t}$	$\cdots$	Tangential (to B) Unit Vector
$\hat{n}$	$\cdots$	Normal (to B) Unit Vector
$\perp$	$\cdots$	Perpendicular to Magnetic Field Grid
T_e	$\cdots$	Electron Temperature $[K]$
ϕ	$\cdots$	Electrostatic Potential $[V]$
ϕ^*	$\cdots$	Thermalized Potential $[V]$
P_c	$\cdots$	Collision Probability
ε	$\cdots$	Electron Energy $[eV]$
k^i	$\cdots$	Ionization Rate $\left[\frac{m^3}{s}\right]$
Δt	$\cdots$	Timestep $[s]$
γ	$\cdots$	Collision Multiplier

j_e $\cdots$ Electron Current Density $\left[\frac{C}{m^2 \cdot s}\right]$

j_i $\cdots$ Ion Current Density $\left[\frac{C}{m^2 \cdot s}\right]$

$\vec{E}$ $\cdots$ Electric Field $\left[\frac{V}{m}\right]$

σ $\cdots$ Electron Conductivity $\left[\frac{1}{\Omega \cdot m}\right]$

μ $\cdots$ Electron Mobility $\left[\frac{m^2}{V \cdot s}\right]$

p_e $\cdots$ Plasma Pressure $[Pa]$

$\vec{u_i}$ $\cdots$ Ion Velocity $\left[\frac{m}{s}\right]$

$\vec{u_e}$ $\cdots$ Electron Velocity $\left[\frac{m}{s}\right]$

$\omega_{B,e}$ $\cdots$ Electron Cyclotron Frequency $\left[\frac{1}{s}\right]$

ν_m $\cdots$ Electron Momentum Transfer Frequency $\left[\frac{1}{s}\right]$

ν_{neut} $\cdots$ Electron-Neutral Collision Frequency $\left[\frac{1}{s}\right]$

λ_a $\cdots$ Virtual Anode Line

λ_c $\cdots$ Virtual Cathode Line

$\vec{q_e}$ $\cdots$ Thermal Conduction $\left[\frac{W}{m^2}\right]$

$\vec{K_e}$ $\cdots$ Thermal Conductivity $\left[\frac{W}{m \cdot K}\right]$

ν_e $\cdots$ Electron Energy Loss Frequency $\left[\frac{1}{s}\right]$

k_{e-Xe} $\cdots$ Ground State Ionization Rate $\left[\frac{m^3}{s}\right]$

k_{e-Xe^+} $\cdots$ Stepwise Ionization Rate $\left[\frac{m^3}{s}\right]$

ν_{e-Xe} $\cdots$ Ground State Ionization Loss Frequency $\left[\frac{1}{s}\right]$

ν_{e-Xe^+} $\cdots$ Stepwise Ionization Loss Frequency $\left[\frac{1}{s}\right]$

ν_{walls} $\cdots$ Wall Loss Frequency $\left[\frac{1}{s}\right]$

m $\cdots$ Spacecraft Mass $[kg]$

V $\cdots$ Spacecraft Velocity $\left[\frac{m}{s}\right]$

$\dot{m}$ $\cdots$ Propellant Mass Flow Rate $\left[\frac{kg}{s}\right]$

U_e $\cdots$ Propellant Exit Velocity $\left[\frac{m}{s}\right]$

ΔV $\cdots$ Mission Velocity Requirement $\left[\frac{m}{s}\right]$

j_{sc} $\cdots$ Space-charge limited Current Density $\left[\frac{A}{m^2}\right]$

D_m $\cdots$ Mass Diffusivity $\left[\frac{m^2}{s}\right]$

D_h $\cdots$ Thermal Diffusivity $\left[\frac{m^2}{s}\right]$

ρ $\cdots$ Density $\left[\frac{kg}{m^3}\right]$

c_p $\cdots$ Specific Heat Capacity at Constant Pressure $\left[\frac{J}{kg \cdot K}\right]$

m_i $\cdots$ Ion Mass $[kg]$

α $\cdots$ Wall-Collision Frequency Coefficient

α_B $\cdots$ Bohm Mobility Coefficient

d $\cdots$ Channel Diameter $[m]$

Constants

$g = 9.8 \left[\frac{m}{s^2}\right]$ $\cdots$ Gravitational Acceleration at Earth's Surface

$k_B = 1.38 \cdot 10^{23} \left[\frac{J}{K}\right]$ $\cdots$ Boltzmann Constant

$e = 1.602 \cdot 10^{-19} [C]$ $\cdots$ Electron Charge

$m_{Xe} = 2.18 \cdot 10^{-25} [kg]$ $\cdots$ Xenon Mass

$m_{Kr} = 1.39 \cdot 10^{-25} [kg]$ $\cdots$ Krypton Mass

$m_e = 9.11 \cdot 10^{-31} [kg]$ $\cdots$ Electron Mass

APPENDIX B

Effusion Sampling Routine

This routine generates the correct velocity distribution for a gas entering the simulation with a "resevoir" Maxwellian temperature T and mass "M". c_1 and c_2 are perpendicular to the direction of effusion and c_3 is in the direction of effusion.

$$\beta_1 = \sqrt{\frac{2k_BT}{M}}$$

`ra=ran1(idum)`

$$\beta_2 = \sqrt{-\log(\texttt{ra})}$$

`ra=ran1(idum)`

$$\theta = 2\pi \cdot \texttt{ra}$$

$$c_1 = \beta_2 * \sin\theta * \beta_1$$

$$c_2 = \beta_2 * \cos\theta * \beta_1$$

`ra=ran1(idum)`

$$\beta_3 = \sqrt{-\log(\texttt{ra})}$$

$$c_3 = \beta_3 * \beta_1$$

APPENDIX C

Ionization and Energy Loss Rates

Ionization and energy loss rates are based on those provided by *Garrigues et al.* (2001). These rates are based on the integration of energy dependent cross sections assuming a Maxwellian electron distribution function. The single direct ionization cross sections for xenon are from *Puech and Mizzi* (1991). The single direct ionization cross sections for krypton are from *Date et al.* (1989). Double direct ionization cross sections for xenon and krypton are from *Wetzel et al.* (1987). Stepwise xenon cross sections are from *Achenbach et al.* (1984). Stepwise krypton cross sections are from *Defrance et al.* (1995).

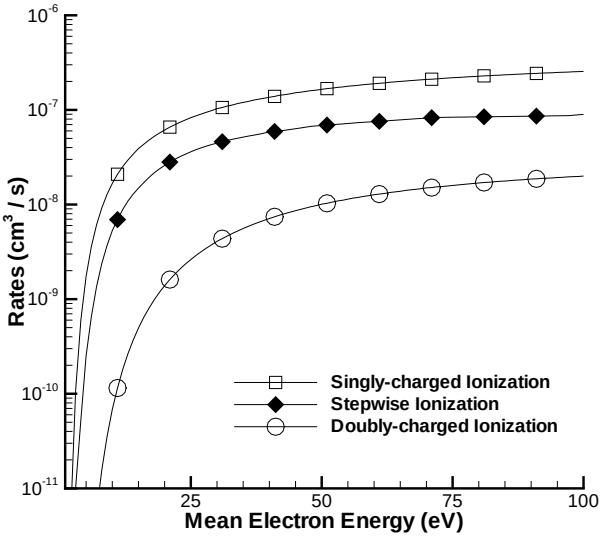


Figure C.1: Xenon Ionization Rates

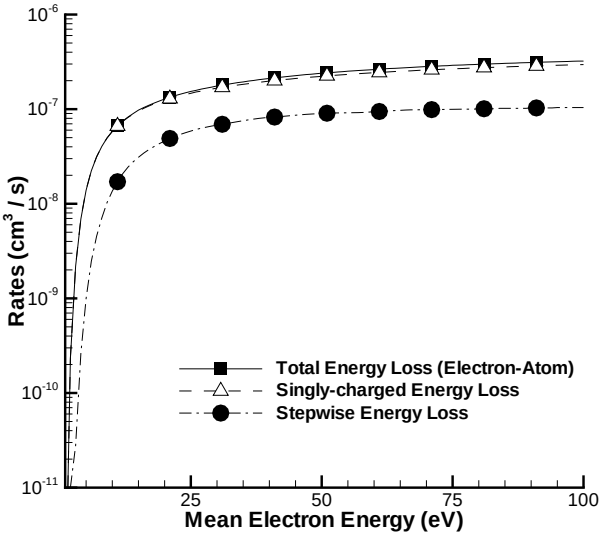


Figure C.2: Xenon Energy Loss Rates

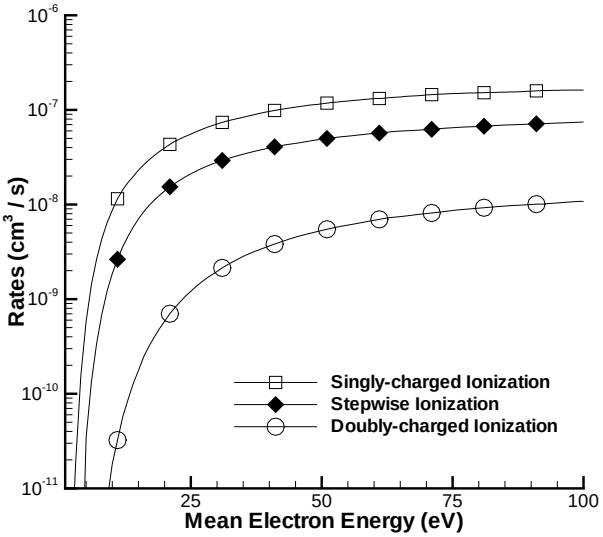


Figure C.3: Krypton Ionization Rates

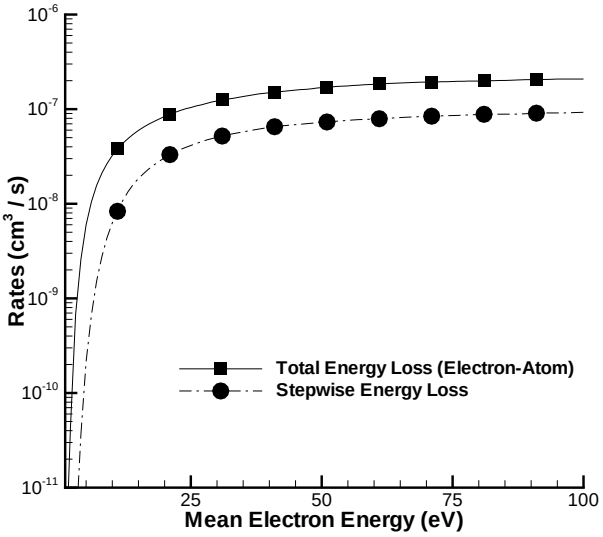


Figure C.4: Krypton Energy Loss Rates

BIBLIOGRAPHY

BIBLIOGRAPHY

C. Achenbach, A. Muller, E. Salzborn, and R. Becker. Single Ionization of Multiply Charged Xenon Ions by Electron Impact. *Journal of Physics B: Atomic and Molecular Physics*, 17(7):1405–1425, 1984.

E. Ahedo, P. Martinez-Cerezo, and M. Martinez-Sanchez. One-Dimensional Model of the Plasma Flow in a Hall Thruster. *Physics of Plasmas*, 8:3058–3068, 2001.

J. Bareilles, G. J. M. Hagelaar, L. Garrigues, C. Boniface, J.-P. Boeuf, and N. Gascon. Critical assessment of a two-dimensional hybrid Hall thruster model: Comparisons with experiments. *Physics of Plasmas*, 11(6):3035–3046, June 2004.

C. L. Birdsall and A. B. Langdon. *Plasma Physics via Computer Simulation*. Institute of Physics Publishing, 1991.

A. M. Bishaev and V. Kim. Local plasma properties in a Hall-current accelerator with an extended acceleration zone. *Soviet Physics - Technical Physics*, 23(9):1055–1057, September 1978.

J. A. Bittencourt. *Fundamentals of Plasma Physics*. Pergamon Press, 1986.

V. Blateau, M. Martinez-Sanchez, O. Batishchev, and J. Szabo. PIC Simulation of High Specific Impulse Hall Effect Thruster. IEPC-01-037, Pasadena, CA, October 2001. 27th International Electric Propulsion Conference.

J.-P. Boeuf and L. Garrigues. Low Frequency Oscillations In a Stationary Plasma Thruster. *Journal of Applied Physics*, 84:3541–3544, 1998.

I. D. Boyd. Hybrid Electron-Particle Model of a Hall Thruster. Internal Technical Document, 2003.

F. F. Chen. *Introduction to Plasma Physics and Controlled Fusion*. Plenum Press, 1984.

H. Date, Y. Sakai, and H. Tagashira. Boltzmann Equatio Analysis of Electron Collision Cross Sections and Swarm Parameters for Krypton. *Journal of Physics D: Applied Physics*, 22(10):1478–1481, 1989.

P. Defrance, M. Duponchelle, and D. L. Moores. Ionization of Atomic Ions by Electron Impact. In R. K. Janev, editor, *Atomic and Molecular Processes in Fusion Edge Plasmas*, pages 153–193, New York, 1995. Plenum.

Y. V. Esipchuck and G. N. Tilinin. Drift Instability in a Hall-Current Plasma Accelerator. *Sov. Phys. - Tech. Phys.*, 21:419, 1976.

J. M. Fife. *Hybrid-PIC Modeling and Electrostatic Probe Survey of Hall Thrusters*. PhD thesis, Massachusetts Institute of Technology, Department of Aeronautics and Astronautics, Cambridge, MA, 1998.

J. M. Fife. Private Communication, June 2004.

J. E. Foster, T. Haag, M. Patterson, G. J. Williams, Jr., J. S. Sovey, C. Carpenter, H. Kamhawi, S. Malone, and F. Elliot. The High Power Electric Propulsion (HiPEP) Ion Thruster. AIAA-2004-3812, Fort Lauderdale, FL, July 2004. 40th AIAA Joint Propulsion Conference.

L. Garrigues G. J. M. Hagelaar, J. Bareilles and J.-P. Boeuf. Two-dimensional model of a stationary plasma thruster. *Journal of Applied Physics*, 91:5592–5598, 2002.

L. Garrigues, I. D. Boyd, and J. P. Boeuf. Computation of Hall Thruster Performance. *Journal of Propulsion and Power*, 17(4), July-August 2001.

J. M. Haas. *Low-Perturbation Interrogation of the Internal and Near-Field Plasma Structure of a Hall Thruster Using a High-Speed Probe Positioning System*. PhD thesis, University of Michigan, 2001.

G. J. M. Hagelaar, J. Bareilles, L. Garrigues, and J.-P. Boeuf. Two-dimensional model of a stationary plasma thruster. *Journal of Applied Physics*, 91(9):5592–5598, May 2002.

G. J. M. Hagelaar, J. Bareilles, L. Garrigues, and J.-P. Boeuf. Role of anomalous electron transport in a stationary plasma thruster simulation. *Journal of Applied Physics*, 93(1):67–75, January 2003.

R. G. Jahn and E. Y. Choueiri. *Encyclopedia of Physical Science and Technology*, volume 5. Academic Press, 3rd edition, 2002.

M. Keidar, I. D. Boyd, and I. I. Beilis. Plasma Flow and Plasma-Wall Transition in Hall Thruster Channel. *Physics of Plasmas*, 9:5315–5322, 2002.

M. Keidar, A. D. Gallimore, Y. Raitses, and I. D. Boyd. On the potential distribution in Hall thrusters. *Applied Physics Letters*, 85(13):2481–2483, 2004.

J. W. Koo and I. D. Boyd. Computational Model of a Hall Thruster. *Computer Physics Communications*, 164(1-3):442–447, December 2004.

W. J. Larson and J. R. Wertz. *Space Mission Analysis and Design*. Space Technology Series. Microcosm, Inc. and Kluwer Academic Press, 2nd edition, 1992.

V. Latocha, L. Garrigues, P. Degond, and J.-P. Boeuf. Numerical simulation of electron transport in the channel region of a stationary plasma thruster. *Plasma Sources Science and Technology*, 11:1–11, 2002.

D. Massey, A. Kieckhafer, J. Sommerville, and L. B. King. Development of a Vaporizing Liquid Bismuth Anode for Hall Thrusters. AIAA-2004-3768, Fort Lauderdale, FL, July 2004. 40th AIAA Joint Propulsion Conference.

A. I. Morozov and A. P. Shubin. Electron kindetics in the wall-conductivity regime I and II. *Sov. J. Plasma Phys.*, 10(6):728–735, 1984.

A. I. Morozov, Yu. V. Esipchuk, G. N. Tilinin, A. V. Trofimov, Yu. A. Sharov, and G. Ya. Shchepkin. Plasma Accelerator With Closed Electron Drift and Extended Acceleration Zone. *Soviet Journal of Plasma Physics*, 17:38, 1972.

P. Y. Peterson, A. D. Gallimore, and J. M. Haas. Experimental Investigation of a Hall Thruster Internal Magnetic Field Topography. IEPC-01-030, Pasadena, CA, October 2001. 27th International Electric Propulsion Conference.

P. Y. Peterson, A. D. Gallimore, and J. M. Haas. An experimental investigation of the internal magnetic field topography of an operating Hall thruster. *Physics of Plasmas*, 9(10):4354–4362, October 2002.

V. Puech and S. Mizzi. Collision Cross Sections and Transport Parameters in Neon and Xenon. *Journal of Physics D: Applied Physics*, 24(11):1974–1985, 1991.

S. Roy and B. P. Pandey. Development of a finite element based Hall thruster model for Sputter Yield Prediction. IEPC-2001-049, Pasadena, CA, October 2001. 27th International Electric Propulsion Conference.

W. M. Ruyten. Density-Conserving Shape Factors for Particle Simulations in Cylindrical and Spherical Coordinates. *Journal of Computational Physics*, 105:228, 1993.

K. Sullivan, J. Fox, M. Martinez-Sanchez, and O. Batishchev. Kinetic Study of Wall Effects in SPT Hall Thrusters. IEPC-2004-3777, Fort Lauderdale, FL, July 2004. 40th AIAA Joint Propulsion Conference.

J. J. Szabo, Jr. *Fully Kinetic Modeling of a Hall Thruster*. PhD thesis, Massachusetts Institute of Technology, Department of Aeronautics and Astronautics, Cambridge, MA, 2001.

R. C. Wetzel, F. A. Baiocchi, T. R. Hayes, and R. S. Freund. Absolute Cross Sections for Electron-Impact Ionization of the Rare-Gas Atoms by Fast-Neutral-Beam Method. *Physical Review A*, 35(2):559–577, 1987.

V. V. Zhurin, H. R. Kaufman, and R. S. Robinson. Physics of closed drift thrusters. *Plasma Sources Science and Technology*, 8:R1–R20, 1999.

ABSTRACT

Hybrid PIC-MCC Computational Modeling of Hall Thrusters

by

Justin William Koo

Chair: Iain D. Boyd

This dissertation describes the development of a 2-D axisymmetric hybrid Particle-In-Cell Monte Carlo Collision (PIC-MCC) Hall thruster code and an investigation into the effects of the numerical parameters and physical models for this code. From the outset, it is clear that some of the necessary model boundary conditions have significant effects on both the spatial and temporal dynamics of the simulation. Therefore, judicious modeling choices must be taken to minimize interference in critical thruster physical processes.

A study of the electron mobility term assesses the performance of various existing computational models of electron mobility. In the process, it is demonstrated that nearly identical thrust performance can be achieved by simulations with different plasma characteristics. As a result, robust validation against more than integrated performance data is necessary to truly validate simulation results. In this regard, none of the computational mobility models shows great success in capturing the details of the mean centerline potential profile.

A semi-empirical electron mobility is developed which results in the successful validation of this code using data measured for the UM/AFRL P5 Hall thruster.

The semi-empirical electron mobility is then used as a reference configuration against which to refine the computational models for electron mobility. An analysis of a dataset of UM/AFRL P5 internal plasma properties uncovered evidence of a strong magnetic self-field during thruster operation. (The existence of a magnetic self-field in this thruster has been identified only once before.) This self-field provides physically motivated corrections which drive the output of the computational model for electron mobility towards the reference configuration.

The original goal of this work was to better understand and extend the physical principles contained in existing computational simulation of Hall thrusters. In the process of validating the existing code with a mobility profile derived from experimental sources, it is discovered that electrostatic codes (such as this one) can produce results in good agreement with experimental data if tuned correctly with some knowledge of experimental conditions; however, fully self-consistent computational modeling of these thrusters will require an electromagnetic solver to properly resolve the correct magnetic configuration during thruster operation.